

学位論文

**Geologic processes controlling physical properties
in forearc wedge**

(沈み込み帯前弧ウェッジの岩石物性を支配する地質過程)

平成27年12月博士（理学）申請

東京大学大学院理学系研究科

地球惑星科学専攻

濱橋 真理

Abstract

One of the key controls on subduction processes and upper plate deformation in convergent margins is the topography on the subducting plate. Understanding the nature of seamount subduction is important to reveal its influence on the forearc wedge deformation, subduction erosion, and seismogenic behaviors along the plate interface. Uplift, subsidence, and faulting in the upper plate associated with seamount subduction have been indicated in previous studies by anomalies in the morphology and structures of the margin such as reentrants, bulges, scarps, and faults found from seafloor bathymetry and seismic surveys. However, the direct geological observation and sampling of the inferred offshore deformation structures during seamount subduction have been limited, and the quantitative features of the upper plate deformation and subduction erosion have been poorly defined.

The Middle America Trench offshore Osa Peninsula, Costa Rica, is known to be an erosive margin with active seismicity where the aseismic Cocos Ridge and associated subsequent seamounts on the Cocos Plate subduct beneath the Caribbean plate, creating an opportunity and necessity to investigate the geologic processes associated with seamount subduction. Previous offshore seismic reflection and multi-beam bathymetry studies have mapped clear high-amplitude widespread seismic reflectors beneath the slope considered to be a major unconformity developed between the slope cover and the more consolidated, intensely deformed upper plate material that exhibit a domed-structure along the plate boundary indicative of a subducted seamount. Abundant normal faults are identified to cut into the slope, and the high-amplitude reflections along faults, pockmarks and mud mounds as signs of abundant fluid seeps were previously reported suggesting an inter-relationship between deformation and fluid flow. The nature of the

seismic reflectors in the forearc wedge and the high consolidation state of the upper plate material beneath the widespread unconformity in the wedge slope has been one of the major unknowns in this margin, but direct geologic observations of these structures and lithology have been limited, though they are important to understand the tectonic-depositional history, sediment-fluid interaction, and the processes related with seamount subduction.

To investigate the geological processes occurring at the Costa Rica margin, the Integrated Ocean Drilling Program (IODP) Expeditions 334 and 344: Costa Rica Seismogenesis Project, Program A Stages 1 and 2 (CRISP-A1, A2) have drilled into this margin offshore Osa Peninsula. In 2012, I have participated in IODP Expedition 344 as a physical property scientist and conducted physical property measurements (porosity, density, P-wave velocity, resistivity, natural gamma ray, magnetic susceptibility, thermal conductivity, shear/compressive strength) during the cruise. IODP Expeditions 334 and 344 have penetrated the major unconformity beneath the middle and upper slopes. Beach deposits and fault zones were observed to distribute across the unconformity beneath the slope, indicating the events of uplift to nearshore environment, erosion, and faulting.

In the present study, to investigate the nature of the seismic reflectors in the forearc wedge, the high consolidation state of the upper plate material, and the roles of fluids at the Costa Rica margin and to quantify the deformation events during seamount subduction, I focused on the consolidation process and physical property transitions of the sediment samples that correlate with the seismic reflectors across the major unconformity and examined the burial condition and the maximum burial depth range of the sediments below the unconformity. On the basis of sediment microstructural observations, physical property measurements, and geochemical composition analyses

using the sediment cores from the middle-slope Site 1380 recovered during IODP Expedition 344, I investigated the effects of burial diagenesis and fluid-sediment interaction on the porosity-depth transition to extract the initial burial compaction curve. I assessed the maximum burial conditions below the unconformity from the porosity-depth curve and quantified the tectonic events of uplift, subsidence, surface erosion, and fault displacement that have occurred across the unconformity as described below.

The upper plate material below the unconformity at the middle slope consisting of lithified terrigenous sediments of clayey siltstone (Units 2, 3) and the slope sediments above consisting of silty clay (Unit 1) were revealed to be characterized by consolidation due primarily to burial compaction and mineral precipitation of zeolites. A Na-type zeolite analcime which formed during burial diagenesis was observed to be present only below the unconformity, whereas a Na/Ca type zeolite heulandite and a Ca-type zeolite laumontite were precipitated due to interaction with high-temperature fluid ($\sim 100^{\circ}\text{C}$) that has likely localized in the vicinity of the unconformity. The experienced maximum temperature of the sediments below the unconformity based on the formation of analcime during burial diagenesis is estimated to range from $86^{\circ}\pm 5^{\circ}\text{C}$ to $122^{\circ}\pm 2^{\circ}\text{C}$, which is higher than the current geothermal gradient. The change in zeolite assemblage indicates that the events of uplift from a greater depth, the transition of pressure-temperature (P-T) conditions, and sediment removal have occurred across the unconformity.

By quantifying the weight percentages of zeolites, I estimated the effect of laumontite and heulandite precipitation on porosity and recalculated the porosity-depth curve eliminating the effect of the fluid-sediment interaction. Based on microstructural observations, the lithology difference across the unconformity was minimal and the burial compaction trend was consistent among Units 1, 2 and 3, enabling to assume a composite

initial porosity-depth curve of the sediments. The depth along the approximate curve of the porosity-depth transition of Unit 1 that matches the porosity of the sediments at the top of Unit 2 corresponds to the maximum burial depth range of the sediments below the unconformity: 1000 ± 400 meters below the seafloor (mbsf).

The distribution of the beach deposits consisting of shell fragments and the damage zones of normal fault regime across the unconformity were observed from the drilled cores, indicating that the sediments that have experienced the maximum burial depth range of 1000 ± 400 mbsf have likely uplifted to the ocean surface and reached the current depth through surface erosion and/or fault displacement.

In this study, the examination of the maximum sediment removal (surface erosion) (Model 1) and maximum fault displacement (Model 2) during uplift and subsidence events were made from the porosity gap across the unconformity and the burial compaction curve derived from the porosity-depth relationship of the sediments. The results suggest that after the initial burial, the sediments uplifted ~ 500 m (Model 2) to 1500 ± 400 m (Model 1) to near sea level, followed by ~ 1050 m subsidence, associated with a mass movement of 1000 ± 400 m maximum (Model 1) and/or normal fault displacement of 450 ± 400 m maximum (Model 2) to reach the current depth range. Under an approx. 10° – 30° dip angle of the slope and fault plane, this thickness of maximum mass movement and normal faulting would correspond to the distances of 4600 ± 3400 m (Model 1) and 2500 ± 2400 m (Model 2) parallel to the slope and fault, respectively.

These events occurred during the time range between 2.20 ± 0.25 Ma and 1.71 ± 0.24 Ma inferred from nannofossil age, which is likely to be consistent with the timing of the onset of the subduction of the Cocos Ridge and the subsequent seamount chains reported by previous studies. The observations in this study suggest that the major unconformity

in the wedge slope at the Costa Rica margin were developed through the geologic processes during Cocos Ridge/seamount subduction, in which significant uplift occurred mirroring the topography of the undergoing seamount, causing over-steepening of the wedge, followed by subsidence and erosion due to normal faulting, mass movement, and basal erosion.

The erosional unconformity, slope sediment cover, mass transport deposit, faulting and folding are indicated by 2D seismic reflection data near the middle-slope Site 1380, and they are consistent with the geologic events quantified from the sediment cores in this study. The events of uplift and subaerial erosion across the unconformity are supported by the seismically imaged erosional unconformity that cuts the landward-dipping reflectors in the margin wedge below. The uplift events have likely induced multiple events of landslide and mass movement, associated with normal fault and reverse fault displacement. The slope sediments and mass transport materials deposited on top of the unconformity, possibly creating additional unconformity due to erosion in the shallower region. The major unconformity and the sedimentary layers were later folded, cut by and accompanied with abundant faults. The fluid paths that enable the significant sediment-fluid-thermal interaction in high temperature which caused zeolite precipitation promoting sediment consolidation revealed from this study may be related to the transitions in hydrologic properties during seamount subduction that initiated abundant fluid flow along the landward- and seaward-dipping high-amplitude reflectors that penetrate from greater depths and occasionally cut the unconformity.

The geologic events across the widespread unconformity observed in both the upper and middle slopes are likely to be regional. However, when comparing the major unconformity developed in the Costa Rica margin between the middle and upper slopes,

the unconformity is shallower in the middle slope and the porosity gap and the indicated amount of sediment removal is larger in the upper slope. Although the unconformity is continuous along the slope due to sequential seamount arrival, the depth and age of the unconformity may be heterogeneous due to structural variations corresponding to multiple events of subsequent seamounts.

My investigation of the balance among tectonic events of uplift, sediment removal, normal faulting and subsidence during seamount subduction revealed that these processes resulted in a significant exhumation of deeper rocks to a shallower region through surface erosion (gravity collapse, mass movement) and/or extension (normal faulting), contributing to the high consolidation of the forearc wedge. The exhumation of the lithified, deeply buried sediments preserving the higher paleo-isotherm in the upper plate may thus have lifted the up-dip limit of the seismogenic zone to a shallower depth range.

Table of Contents

1. Introduction and Research Objectives.....	1
1.1 Seamount subduction and its effects on the forearc wedge in convergent margins.....	1
1.2 Middle America Trench offshore Osa Peninsula, Costa Rica.....	2
2. Geologic setting of the study area.....	6
2.1 Tectonic setting of the Middle America Trench offshore Osa Peninsula, Costa Rica.....	6
2.1.1 The on-land upper plate response to the Cocos Ridge/ seamount subduction.....	7
2.1.2 The forearc wedge of the Costa Rica margin offshore Osa Peninsula: insights from 2D and 3D seismic reflection and multi-beam bathymetry surveys.....	8
2.1.3 Seismicity along the Costa Rica margin offshore Osa Peninsula.....	11
2.2 Integrated Ocean Drilling Program (IODP) Expeditions 334 and 344: Costa Rica Seismogenesis Project (CRISP).....	12
2.2.1 CRISP drilling sites along the 2D seismic line BGR99-7.....	12
2.2.2 The major unconformity penetrated during IODP Expeditions 334 and 344.....	13
2.2.3 The author’s participation and contribution to IODP Expedition 344 as a physical property scientist and scope of this study (post-cruise research).....	14
2.3 Study area.....	16

2.3.1	Geologic structure and an interpretation based on the 2D seismic reflection profile BGR99-7 at CRISP Middle-slope Site 1380.....	16
2.3.2	Lithology and structure of CRISP Middle-slope Site 1380.....	17
2.3.3	Physical property contrast across the unconformity and the seismic reflectors observed at Site 1380.....	20
2.3.4	Lithology, structure, and physical properties observed at CRISP Upper-slope Site 1379 and Site 1413.....	21
3.	Methodology.....	24
3.1	Shipboard physical property measurements during IODP Expedition 344 (conducted with the physical property group during the cruise).....	25
3.2	Laboratory methods (post-cruise research conducted by the author).....	26
4.	Results and Discussion.....	33
4.1	Consolidation trend based on microstructural observations and physical properties.....	33
4.1.1	Zeolite precipitation as pore-filling minerals.....	34
4.1.2	Cross correlation of physical properties.....	35
4.2	Element and mineral compositions of the sediments.....	36
4.2.1	Experienced temperature range of sediments and precipitation conditions of zeolite assemblages.....	38
4.2.2	The effect of zeolite precipitation and sediment-fluid interaction on the porosity decrease.....	42
4.3	The initial compaction curve derived from the porosity-depth transition and the maximum burial depth range below the unconformity.....	44
4.4	The uplift, material removal, subsidence, and deposition inferred	

from the porosity-depth transition.....	47
4.4.1 Model 1: Rapid, maximum uplift and material removal.....	48
4.4.2 Model 2: Normal faulting, uplift, and minimum material removal.....	50
4.5 Comparison with the upper slope Site 1379 and Site 1413.....	52
4.6 Major events at the wedge slope offshore Costa Rica inferred from this study and the relationship with the Cocos Ridge/seamount subduction.....	57
4.7 Comparison of the structures from the 2D seismic profile BGR99-7 at Site 1380 and the 3D seismic reflection surveys.....	61
4.8 Characteristics of erosive wedge development affected by seamount subduction: –A high consolidation state and the effects during subduction erosion.....	63
4.9 The exhumation of consolidated sediments through surface erosion and faulting during seamount subduction and insights into seismogenic behaviors and fluid/heat flow.....	64
5. Conclusion.....	68
6. Acknowledgements.....	73
7. References.....	78

1. Introduction and Research Objectives

1.1 Seamount subduction and its effects on the forearc wedge in convergent margins

Forearc wedge in subduction zones (Figure 1) are characterized by variations in geometry, geomorphology, and kinematics, related to the deformation styles in the upper plate. One of the key controls on subduction processes and upper plate deformation is the topography of the subducting plate. The subduction of topographic highs at some margins such as seamounts are likely to have large impacts on forearc wedge structures, seismogenesis, and volcanism, as they collide with the overriding plates [e.g., *Vogt, 1973; McCann and Habermann, 1989; Geist et al., 1993; Dominguez et al., 1998; Rosenbaum and Mo, 2011; Bassett and Watts, 2015*].

The evidence for seamount subduction has generally been from seafloor bathymetry and seismic reflection and refraction data, identified based on one or more anomalies in the morphology of the margin such as reentrants, distinctive furrows, scarps and/or uplifted bulges, which have likely formed and tracked the path of seamounts as they subduct [e.g., *Dominguez et al., 1998; von Huene et al., 2000*]. Deformation structures such as backthrusts propagating from the base of the seamount, out-of-sequence thrusts located on the landward side of the seamount, and normal faults that formed around the seamount's track have also been observed, and were also reproduced by sand-box experiments [e.g., *Dominguez et al., 1998*].

These prior studies indicated that during seamount subduction, substantial uplift and subsidence may occur in the forearc wedge associated with pervasive faulting. Seamount subduction may also initiate significant abrasion along the plate boundary, leading to forearc subsidence and subduction erosion, *i.e.* the frontal and basal removal of the overriding plate [e.g., *von Huene and Lallemand, 1990; Ranero and von Huene,*

2000].

However, the direct geological observation and sampling of these offshore deformation structures during seamount subduction inferred from bathymetry and seismic data were limited in the previous studies, and the quantitative features of the wedge deformation have not been well characterized. For the determination of the events of uplift, subsidence, faulting, and erosion caused by seamount subduction, ocean drillings into margins where seamounts are subducting could provide opportunities to directly observe and sample the lithology and structures affected by these processes and the chance to compare these findings with larger-scale seismic and bathymetry data.

1.2 Middle America Trench offshore Osa Peninsula, Costa Rica

The Middle America Trench offshore Osa Peninsula, Costa Rica, is known to be an erosive margin with active seismicity where the aseismic Cocos Ridge and a number of seamounts on the Cocos Plate subduct beneath the Caribbean Plate, creating one of the best study areas to investigate the geologic processes associated with seamount subduction and subduction erosion. From on-land surveys, the Cocos Ridge subduction is inferred to have caused uplift and exhumation of the Osa Peninsula and Quepos region, and the creation of fold-and-thrust belts [*Corrigan et al.*, 1990; *Morell et al.*, 2012; *Gardner et al.*, 1992; 2013; *Sak et al.*, 2004; *Kolarsky and Mann*, 1995; *Fisher et al.*, 2004; *Sitchler et al.*, 2007].

Despite the extensive on-land studies, however, little is known about the offshore outer forearc wedge where active seismicity occurs. Offshore surveys of 2D- and 3D-seismic reflections and multi-beam bathymetry studies have mapped clear high-amplitude widespread seismic reflectors (acoustic basement reflectors) that are considered to be a

major unconformity that cuts and separates the more intensely deformed consolidated materials below from younger slope sediments above [von Huene *et al.*, 2000; Kluesner *et al.*, 2013; Bangs *et al.*, 2015]. Along the plate boundary, a domed structure was observed as evidence of seamount subduction [Bangs *et al.*, 2015]. Abundant normal faults were observed to cut into the slope, and landward- and seaward-dipping seismic reflectors as thrusts faults associated with folding are distributed beneath the unconformity [e.g., Kluesner *et al.*, 2013; Bangs *et al.*, 2015].

In addition to these high-amplitude reflections along faults, pockmarks and mudmounds indicative of abundant fluid flow and seeps were also reported based on seafloor bathymetry [e.g., Kluesner *et al.*, 2013; Bangs *et al.*, 2015]. The nature of these seismic reflectors in the forearc wedge and the lithology of the upper plate material beneath the unconformity have been one of the major unknowns in this margin, but direct geologic observations of these structures and quantification of the geologic processes have been limited, though they are important to understand the tectonic-depositional history and sediment-fluid interaction of this region and the processes related to seamount subduction.

To investigate the geological processes occurring at the Costa Rica margin, the Integrated Ocean Drilling Program (IODP) Expeditions 334 and 344: Costa Rica Seismogenesis Project, Program A Stages 1 and 2 (CRISP-A1, A2) drilled into this margin offshore Osa Peninsula. In 2012, I participated in Expedition 344 as a physical property scientist and conducted physical property measurements (porosity, density, P-wave velocity, resistivity, natural gamma rays, magnetic susceptibility, thermal conductivity, shear/compressive strength) during the cruise. Expeditions 334 and 344 penetrated the major unconformity characterized by high-amplitude seismic reflectors

beneath the middle-slope Site 1380 and the upper-slope Site 1379 [Vannucchi *et al.*, 2012; Harris *et al.*, 2013]. Beach deposits and fault zones were observed to be distributed above the consolidated sediments across the unconformity beneath the slope, indicating the events of uplift to the nearshore environment, erosion, and faulting.

At the upper-slope Site 1379 recovered during Expedition 334, the benthic foraminifera distribution of abyssal species below the unconformity and beach species above inferred an uplift and subsidence that occurred in the age range roughly consistent with the initiation of the Cocos Ridge subduction [Vannucchi *et al.* 2013] reported from plate reconstruction models [e.g., Barckhausen *et al.*, 2001; MacMillan *et al.*, 2004; Lonsdale, 2005; Morell, 2015]. The amount of uplift and subsidence were estimated from the seafloor paleo-depth transition inferred from the benthic foraminifera assemblage [Vannucchi *et al.* 2013].

However, the burial condition and the maximum burial depth range of the sediments below the unconformity have been unknown, although they are crucial in the determination of the amount of surface erosion and/or fault displacement associated with uplift and subsidence across the unconformity. Sharp contrasts in physical properties (porosity, density, P-wave velocity) were identified across the unconformity that correlate with the acoustic basement reflectors [Vannucchi *et al.*, 2012; Harris *et al.*, 344]. The physical property contrast is the key to studies of the consolidation state and burial conditions of the upper plate framework material and to efforts to assess the amounts of uplift, subsidence, and material removal across the unconformity.

The geologic processes across the acoustic basement reflector recovered at middle-slope Site 1380 during Expedition 344 have not yet been examined. The relationship with the events indicated from the upper-slope Site 1379 has been less constrained, though it

is important to determine whether the geologic events across the unconformity are widespread throughout the wedge or occur locally.

The objectives of the present study were to clarify and quantify the tectonic processes (uplift, subsidence, erosion, faulting) during seamount subduction by investigating the physical properties and consolidation process of sediments across the major unconformity at the Costa Rica subduction zone focusing on the middle-slope Site 1380. By examining the effects of compaction, burial diagenesis, and fluid-sediment interaction on the porosity-depth curve based on physical property measurements, microstructural observations, and geochemical (mineral/element) analyses (the methodology is described in Section 3), I evaluated the compaction curve and mineral assemblage of the sediments to obtain the maximum burial conditions (temperature and depth range) below the unconformity and assessed the amounts of tectonic uplift, erosion, subsidence, and fault displacement in this margin. To determine whether the geologic events across the unconformity are widespread or local, I compared the results between the upper slope and the middle slope.

Through this process, I obtained geologic information about the structures indicated by 2D and 3D seismic reflection surveys in the Costa Rica margin, and I investigated the upper plate material beneath the unconformity, the roles of fluids in the slope, and the structural development of the forearc wedge during seamount subduction. The findings obtained in this study will ultimately provide insights into the effects of seamount subduction on the processes of subduction erosion and seismogenic behaviors.

2. Geologic Setting of the Study Area

2.1 Tectonic setting of the Middle America Trench offshore Osa Peninsula, Costa Rica

The Middle America Trench off the coast of Costa Rica (Figures 2, 3) is considered to be an erosive margin characterized by active seismicity and subduction of the rough seafloor. This margin has also been a target of the National Science Foundation (NSF) MARGINS Program (NSF 07-546) (<http://nsf.gov/pubs/2007/nsf07546/nsf07546.htm#toc>) and the GeoPRISMS Program (NSF 12-537) (http://www.nsf.gov/publications/pub_summ.jsp?ods_key=nsf12537). Offshore the western margin of Costa Rica, the oceanic Cocos Plate subducts under the Caribbean plate at the convergence rate of ~90 mm/y [DeMets, 2001]. The bathymetry and morphology of the Cocos-Nazca spreading center (CNS)-generated Cocos Plate is relatively rougher offshore Osa Peninsula compared to the East-Pacific Rise (EPR)-generated crust offshore Nicoya Peninsula. The seafloor offshore Osa Peninsula stands at a maximum ~2.5 km higher than the surrounding seafloor [Barckhausen *et al.*, 2001; Walther, 2003], due to the subduction of the aseismic Cocos Ridge, a 200 km wide and 1000 km long trail of the Galapagos hot spot [Johnson and Lowrie, 1972; Werner *et al.*, 2003] on the eastern edge of the Cocos Plate that is associated with multiple seamounts as subsequent chains.

Northwest of the Cocos Ridge, other seamounts and topographic highs of 1–2 km in height and 10–20 km in diameter cover ~40% of the seafloor [von Huene *et al.*, 1995; 2000]. The crustal thickness of the Cocos Plate increases southeastward, correlating approximately with the decrease in the dip of the Cocos slab (indicating flat slab subduction), where the Wadati-Benioff zone eventually shallows from $> 60^\circ$ in the northwestern region of the Cocos Plate [Guendel *et al.*, 1989; Protti *et al.*, 1995; Ranero

and von Huene, 2000; Syracuse *et al.*, 2008] to near-horizontal along the axis of the Cocos Ridge [Protti *et al.*, 1994; 1995; Husen *et al.*, 2003; Linkimer *et al.*, 2010]. Receiver function and tomographic analyses indicated that the slab is relatively shallow for ~75 km from the trench northwest of the Cocos Ridge, but steepens to 80° at the depth of > ~50 km [Dinc *et al.*, 2010; Dzierma *et al.*, 2010; 2011], although the geometry at greater depths remains poorly understood [e.g., Morell, 2015].

2.1.1 The on-land upper plate response to the Cocos Ridge/seamount subduction

Previous on-land chronological studies reported that the Cocos Ridge subduction probably initiated the emergence and deformation of Burica Peninsula [Corrigan *et al.*, 1990; Morell *et al.*, 2012] and Osa Peninsula with an uplift rate ranging from 1.7 m/ky to 8.5 m/ky in the latter and subsidence up to ~6 m/ky along the northwest coast [Gardner *et al.*, 1992; 2013; Sak *et al.*, 2004], the development and shortening (10–40 mm/y) of the Fila Costena thrust belt [Kolarsky *et al.*, 1995; Fisher *et al.*, 2004; Sitchler *et al.*, 2007] and escape faulting away from the ridge [Kobayashi *et al.*, 2014] in the inner forearc, the ~2 km of rock uplift and exhumation of the Cordillera de Talamanca volcanic arc within the past 1–3 Ma [Grafe *et al.*, 2002; Morell *et al.*, 2012] and late Miocene termination of calc-alkaline volcanism [de Boer *et al.*, 1995; Abratis and Worner, 2001], and the development of the Limon back arc thrust belt [Goes *et al.*, 1993; Collins *et al.*, 1995].

The estimates for the timing of the arrival of seamounts, rough crust, and Cocos Ridge subduction along the Middle America Trench offshore Osa Peninsula inferred from the initiation of the upper plate deformation mentioned above have been controversial. Estimates of the onset of Cocos Ridge subduction have ranged from 1 Ma [Lonsdale and Klitgord, 1978; Gardner *et al.*, 1992] to 2–3 Ma [Morell, 2015] from modern plate

reconstructions; 1 Ma [Corrigan *et al.*, 1990], 3.6 Ma [Collins *et al.*, 1995], and ~2.5 Ma [Vannucchi *et al.*, 2013] based on paleobathymetric studies from benthic foraminifera distribution; <3 Ma [Morell *et al.*, 2012] to 5–7 Ma [Grafe *et al.*, 2002] based on unroofing of the Cordilera de Talamanca; to 2–3 Ma [MacMillan *et al.*, 2004], 5 Ma [de Boer *et al.*, 1995], and 8 Ma [Abratis and Worner, 2001] based on the age of volcanic/igneous rocks in the magmatic arc inboard of the Cocos Ridge.

Further investigation is necessary to determine the timing of the Cocos ridge/seamount subduction in this margin. However, the reported distribution of the youngest radiometric ages from plutons of the Costa Rica-Panama volcanic arc [de Boer *et al.*, 1995; Wegner *et al.*, 2011] is thought to indicate that the late Miocene cessation of calc-alkaline volcanism in Costa Rica may be unrelated to the Cocos Ridge subduction [Morell *et al.*, 2012], and may be instead linked to the initiation of the oblique Nazca plate subduction [Morell, 2015].

Recent modern plate reconstructions also suggest that the initiation of seamount and rough crust subduction northwest of the Cocos Ridge started at ~3–4 Ma [e.g., Morell, 2015].

2.1.2 The forearc wedge of the Costa Rica margin offshore Osa Peninsula: insights from 2D and 3D seismic reflection and multi-beam bathymetry surveys

Despite the extensive on-land surveys mentioned above, however, little had been known about the offshore outer forearc wedge and the lithology of the upper plate framework material.

The 2D and 3D seismic reflection studies along the margin indicated that the offshore forearc is composed of an approx. 2-km-thick slope sediment cover overlying

the upper plate framework material cut by a widespread major unconformity characterized by clear high-amplitude seismic reflectors (acoustic basement reflectors) observed from offshore Osa to Nicoya Peninsula [von Huene *et al.*, 2000].

One hypothesis for the lithology of the upper plate framework rock that has been proposed [e.g., Harris *et al.*, 2013] is that the basement is composed of accreted oceanic lithologies composed of igneous rocks (oceanic islands and aseismic ridge terranes) that could be derived from the subducted materials generated by the Galapagos hotspot, similar to the rocks observed offshore in the exposed Caribbean Large Igneous Province [Hauff *et al.*, 1997; 2000; Sinton *et al.*, 1997; Hoernle *et al.*, 2002], the Quepos and Osa terranes [Hauff *et al.*, 1997; Vannucchi *et al.*, 2006], and the Osa mélange [Vannucchi *et al.*, 2006].

Another hypothesis that has been proposed [e.g., Harris *et al.*, 2013] is that the upper plate basement is composed of old accreted sediments (paleo-accretionary prism material), which is consistent with the observed seismic velocity (~3.5 km/s) below the large-scale unconformity based on seismic surveys [Harris *et al.*, 2013; Stavenhagen *et al.*, 1998].

2D and 3D seismic reflection images indicate that the upper plate is a densely fractured, folded slope margin beneath the major unconformity (Figure 4) [Kluesner *et al.*, 2013; Bangs *et al.*, 2015]. A small accretionary wedge was shown to have formed at the trench [Bangs *et al.*, 2015] (Figure 4). High-amplitude reversed polarity reflection characterize the normal faults that are abundant in the slope cover cutting through the acoustic basement reflector. Landward-dipping thrust faults were also shown to be concentrated below the unconformity, also cutting into the slope cover which extends down to the plate interface [e.g., Kluesner *et al.*, 2013; Bangs *et al.*, 2015] (Figure 4).

Along the plate boundary, 3D seismic reflection images have mapped horst and graben structures that characterize a rough interface and a domed structure at ~6 km depth that provides evidence of a subducted seamount [Bangs *et al.*, 2015] (Figure 4). Seaward-dipping thrusts faults are observed to form along the seaward side of the domed structure, and they are coincident with the location where the fault orientation changes between the landward- and seaward- dipping faults/fabrics [Bangs *et al.*, 2015] (Figures 4, 5), which may indicate a deformation structure associated with seamount subduction. The relative reflection amplitude along the plate boundary fault shows high values until ~6 km depth, which may characterize the velocity contrast and fluid distribution that may be coincident with the up-dip limit of the seismogenic zone [Bangs *et al.*, 2015] (Figure 6).

Multi-beam bathymetry and side-scan sonar studies have identified structures of reentrants, embayments, bulges, scarps, furrows, faults, and slides on the seafloor as evidence for seamount subduction along the trench offshore Osa Peninsula to Nicoya Peninsula, Costa Rica [e.g., Ranero *et al.*, 2008] (Figure 3). 3D seismic reflection and multi-beam bathymetry studies detected pockmarks, mud mounds, and active gas plumes, and they identified substantial amounts of potential fluid seepage on the shelf and slope regions that are associated with faults and folds [Ranero *et al.*, 2008; Sahling *et al.*, 2008; Kluesner *et al.*, 2013]. Large amounts of fluids and gases are likely to permeate through the margin slope through fault systems, and these shallow- to- deep fluid seep indicators are found especially across the mid-slope region [Ranero *et al.*, 2008; Sahling *et al.*, 2008; Kluesner *et al.*, 2013; Bangs *et al.*, 2015]. The root mean square (RMS) reflection amplitude calculated from the 3D seismic reflection along the major unconformity [Bangs *et al.*, 2015] indicates zones of abundant fluid/gas migration that coincide with the location of the evidence of fluid seepage such as pockmarks and gas plumes detected by

Kluesner et al. [2013] (Figure 6).

These geophysical indications of fluid seeps suggest an inter-relationship among the fluid abundance along faults, the effective stress, and the fault zone architecture. The fluid interactions may also affect the aseismic to seismogenic transition in the upper plate along the plate interface [e.g., *Ranero et al.*, 2008]. These fluids may also contribute to effective hydrothermal cooling of the upper plate crust.

The nature of the seismic reflectors and the major unconformity developed in the forearc wedge and the lithology of the consolidated upper plate material beneath the unconformity have been one of the major unknowns in the Costa Rica margin, but direct geologic observations of these structures and quantification of the geologic processes have been limited, though they are important to understand the tectonic-depositional history and sediment fluid interaction of this region and the processes related with seamount subduction. Further investigations especially from direct geologic samples are necessary to test these geophysical observations and hypotheses derived from seismic surveys of the upper plate.

2.1.3 Seismicity along the Costa Rica margin offshore Osa Peninsula

The Costa Rica subduction zone exhibits active seismicity along the margin. Offshore of the Osa Peninsula, the 1999 Mw 6.9 Quepos interplate thrust earthquake initiated at the down-dip extension of the incoming Quepos Plateau, and aftershock clustering was located in regions of lower plate relief at 10–30 km depths [*Bilek et al.*, 2003; *Husen et al.*, 2002; *Protti et al.*, 1995] (Figure 7). Another event during the 2002 Mw 6.4 Osa earthquake and its aftershocks exhibited a shallow (~6 km depth) underthrusting event that occurred along the plate boundary [*Arroyo et al.*, 2014] (Figure

7).

2.2 Integrated Ocean Drilling Program (IODP) Expeditions 334 and 344: Costa Rica Seismogenesis Project (CRISP)

The Integrated Ocean Drilling Program (IODP) Expeditions 334 and 344: Costa Rica Seismogenesis Project, Program A Stages 1 and 2 (CRISP-A1, A2) were designed to identify the factors that control the generation and seismic rupture of large earthquakes at erosive subduction zones, and to study the geological processes characteristic of this margin [Vannucchi *et al.*, 2012; Harris *et al.*, 2013].

2.2.1 CRISP drilling sites along the 2D seismic line BGR99-7

The CRISP study area (Figures 2, 3, 8) is located offshore of the Osa Peninsula along the 2D seismic line BGR99-7 acquired during Cruise BGR99 [Ranero *et al.*, 2008] (Figures 8, 9). IODP Expeditions 334 and 344 drilled into the incoming Cocos Plate and trench and slope sites on the overriding Caribbean Plate in 2011 and 2012 [Vannucchi *et al.*, 2012; Harris *et al.*, 2013].

The 2D seismic data from Cruise BGR99 were processed in depth, and the survey lines were flanked by two lines at 1- km spacing and 2-, 5-, and 10- km spacing [Harris *et al.*, 2013]. The distribution of the plate boundary fault and the major unconformity beneath the slope were identified using high-amplitude reflections as shown in the large-scale overview of the wedge in Figure 9. Beneath the unconformity, high-amplitude landward-dipping reflectors are present, extending down to near the plate boundary (Figure 9). A small frontal accretionary prism has developed near the trench, indicated by regional landward-dipping faults (Figure 9).

2.2.2 The major unconformity penetrated during IODP Expeditions 334 and 344

CRISP Program A penetrated the major acoustic boundary beneath the slope sediments at the upper-slope Site 1379 during IODP Expedition 334 and at the middle-slope Site 1380 during IODP Expedition 344 (Figure 9).

Across the unconformity developed between the slope sediments above and the consolidated sediments below, beach deposits and fault zones were observed indicating the events of uplift to nearshore environment, erosion, and faulting.

In the upper-slope Site 1379 recovered during Expedition 334, *Vannucchi et al.* [2013] reported the paleo-water-depth records of the sediments from the benthic foraminifera distribution of abyssal species below the unconformity and beach species above, suggesting a rapid uplift of ~800 m (middle bathyal depths) to nearshore conditions at 2.3-2 Ma (early Pleistocene) that occurred across the unconformity. From the benthic foraminifera distribution in the shallower region, *Vannucchi et al.* [2013] also inferred a rapid subsidence of ~1200 m later at 2.3-2 Ma (early Pleistocene) and an uplift of ~1000 m from 1.9 Ma to now (middle-late Pleistocene to Holocene).

The investigation on the geologic events across the unconformity is important to understand the tectonic/depositional history of this margin. The geologic events across the unconformity in the middle-slope Site 1380 recovered during Expedition 344, however, had not been examined yet, and the relationship with the events indicated from the upper-slope Site 1379 was less constrained. The examination in the middle slope and the comparison with the upper slope are crucial to investigate the geologic events in the wedge slope and to study whether the events across the unconformity is widespread throughout the wedge or occurring locally.

The major unconformity drilled at the upper-slope Site 1379 was characterized by a clear contrast in the shipboard physical properties [Vannucchi *et al.*, 2012]. The nature of the seismic reflectors and the major unconformity had been unknown, and the physical property transitions across the major unconformity inferred from the seismic reflectors would provide information on the geologic events occurring at this horizon. The high consolidation state of the sediments beneath the unconformity had been less understood, requiring a study of what controls the physical properties of the upper plate material through core-log-seismic integration.

2.2.3 The author's participation and contribution to IODP Expedition 344 as a physical property scientist and scope of this study (post-cruise research)

From October 21 to December 20, 2012, I participated in IODP Expedition 344 CRISP drilling as a physical property scientist, and conducted physical property measurements (porosity, density, P-wave velocity, resistivity, natural gamma rays, magnetic susceptibility, thermal conductivity, shear/compressive strength) with the physical property laboratory group onboard. I also obtained sediment/rock samples that were cored during the cruise for the post-cruise research presented in this study.

A clear physical property contrast was observed from discrete sample measurements across the major unconformity at the middle-slope Site 1380 drilled during the Expedition, characterized by a decrease in the porosity and increase in P-wave velocity and density of the consolidated sediments below the unconformity [Harris *et al.*, 2013]. These physical property contrast correlate well with the major seismic reflectors observed from seismic surveys, and these properties are likely to reflect the structures that characterize the wedge slope at this horizon.

The physical property contrasts provide information on the consolidation state of the sediments, and are the keys to study the geologic events of uplift, subsidence, and material removal across the unconformity, though they had not been examined in previous studies. The burial condition and the maximum burial depth range of the sediments below the unconformity had been unknown, but are crucial to study the amount of missing materials (sediment removal and fault displacement) and to evaluate the deformation events across the unconformity.

In the present study, to investigate the nature of the seismic reflectors in the forearc wedge, the high consolidation state of the upper plate material, and sediment-fluid interaction across the unconformity, I focused on the consolidation process and physical property transitions of the sediment samples that correlate with the seismic reflectors, and examined the burial condition and the maximum burial depth range of the sediments below the unconformity.

On the basis of sediment microstructural observations, physical property measurements, and geochemical composition analyses using the sediment cores from the middle-slope Site 1380 recovered during IODP Expedition 344, I investigated the effects of burial diagenesis and fluid-sediment interaction on the porosity-depth transition to extract the initial burial compaction curve (Section 3. Methodology). I assessed the maximum burial conditions below the unconformity from the porosity-depth curve and quantified the tectonic events of uplift, subsidence, surface erosion, and fault displacement that have occurred across the unconformity.

To investigate whether the geologic events across the unconformity is regional or local, I compared the physical properties between the upper and middle slopes. I compared the geologic events inferred from the drilled cores with the structural

interpretation from the 2D seismic line (BGR99-7).

2.3 Study area

2.3.1 Geologic structure and an interpretation based on the 2D seismic reflection profile BGR99-7 at CRISP Middle-slope Site 1380

CRISP Site 1380 (Figures 8, 10) is located on the middle slope of the Costa Rica margin, 38 km offshore Osa Peninsula and 24 km from Cano Island along seismic Line BGR99-7 at a water depth of 502.7 m. Figures 10 and 11 show the enlarged prestack time-migrated seismic Line BGR99-7 near the middle-slope Site 1380 [Harris *et al.*, 2013]. The major unconformity below the slope is characterized by high amplitude reflection, cutting the landward-dipping reflectors below the slope cover, indicating that erosion has occurred across this boundary (Figure 11). Above the unconformity, characteristic zones of relatively less-defined reflection layers (Figure 11, colored in blue) are present, which may represent incoherent fabric such as mass transport deposits, indicating that slope failure and mass movement probably occurred along the unconformity (Figure 11). Abundant faults that are mostly normal faults are distributed below the unconformity and within the slope cover, occasionally cutting the unconformity (Figure 11). The unconformity and sedimentary layers are folded, associated with and cut by faulting. Similar pockets of less-defined layers are found in the shallow portion of the slope cover, indicating multiple landslide events.

Based on these observations, I constructed a hypothesis regarding the structural development of the wedge slope and the observed unconformity in three stages, in the order of occurrence (Figure 12). The unconformity that cut the landward-dipping reflectors below indicates that uplift and erosion have occurred across this boundary

(Figure 12, Stage 1). These events probably induced landslide(s) and mass movement associated with normal-fault and reverse-fault displacement (Figure 12, Stage 2). Slope sediment and mass transport were deposited on top of the unconformity, possibly creating additional unconformity (Figure 12). Similar zones of landslide deposits are found in the shallow portion of the slope cover, suggesting that multiple landslides have occurred, accompanied by faulting along near horizontal planes. The unconformity and sedimentary layers were later folded, cut by and associated with abundant faults (Figure 12, Stage 3).

Further investigation is necessary to examine the uplift, erosion, and faulting events across the unconformity. In the present study, I focused on the slope sites where the major seismic reflectors are present beneath the slope sediments in order to clarify the structural development of the wedge slope and the major unconformity of this region. Site 1380 (Figure 10) was targeted in an effort to penetrate the unconformity and was the first hole to be successfully drilled into the higher-velocity materials with best recovery in the middle slope. This drilling recovered cores across several boundaries that correlate with clear seismic reflectors, enabling the evaluation of the lithology, structure, and physical properties of the sediments. I focus here on the middle-slope Site 1380 and present new results to compare with the upper-slope Site 1379 and Site 1413.

2.3.2 Lithology and structure of CRISP Middle-slope Site 1380

Expedition 334 cored from 0- to 513.56 mbsf at Site 1378A and 397–474.75 mbsf at Site 1380A, and was succeeded by Expedition 344, which cored from 438–800 mbsf at Site 1380C [e.g., *Ranero et al.*, 2008; *Harris et al.*, 2013] (Figure 10). Intraplate earthquakes and geodetic measurements indicated that this site is located seaward of the up-dip extent of plate interface seismicity and is not fully locked [e.g., *Arroyo et al.*, 2014;

Harris et al., 2013]. The major seismic reflector was penetrated, and clear contrasts in physical properties were identified at ~551.48 mbsf between silty clay and consolidated clayey siltstone.

At Site 1380, the upper plate material beneath the unconformity at 551.48 mbsf is lithified, low-porosity sediment consisting of clayey siltstone with medium to coarse sandstone of Unit 2 (late Pliocene to early Pleistocene) and silty claystone with fine sandstone of Unit 3 (late Pliocene) (Figure 10). Above the unconformity is the high porosity slope sediment of Unit 1 (late? Pliocene to late Pleistocene) consisting of silty clay with fine sandstone. Between Unit 1 and 2, unconsolidated sandstone layers ~12 m thick containing abundant shell fragments are distributed above the consolidated materials (at the upper and middle slopes) (Figure 13). These unconsolidated beach deposits indicate a change of the depositional environment to a nearshore setting.

The structural observations indicated that the bedding dips vary from subhorizontal to moderately steep, but generally dip between 10° and 30° northeast and southwest, respectively [*Harris et al.*, 2013] (Figure 14). The foliation intensity is characterized by a preferred alignment of platy minerals that increase progressively downhole toward the unconformity at 551.48 m [*Harris et al.*, 2013]. A strongly foliated interval with abundant deformation bands and veins were found between 496.37 mbsf and 548.98 mbsf, and a ~53-m-thick damage zone were identified in the recovered cores ~2.5 m above the unconformity (~550.22 mbsf), with characteristic slickenlines that support fault activities occurring at this horizon (Figure 13) [*Harris et al.*, 2013]. Shipboard fault kinematics analyses inferred a normal fault stress regime with σ_1 oriented vertically and σ_3 oriented in a northeast-southwest direction, similar to the plate convergence direction [*Harris et al.*, 2013] (Figure 14).

The slope sediments of Unit 1 above the unconformity exist between the nannofossil zones of NN 19 zone (1.47–1.95Ma) and the NN 18 zone (1.95–2.44 Ma), which is marked by the first occurrence of a nannofossil, *Discoaster brouweri* (~1.95 Ma) in the lower Unit 1 [Harris *et al.*, 2013]. The lithified sediments of Unit 2 (~218.9-m-thick) below the unconformity exist within the NN 18 zone (1.95–2.44 Ma), and Unit 3 is assigned as NN 15 – NN 17 zone. From the age range of the NN 18 zone and NN 19 zone, the age gap across the unconformity is estimated to be less than 0.49 m.y. (2.44–1.95 Ma) ~0.97 m.y. (2.44–1.47 Ma) in the middle slope. Based on the sediment thickness (depth range) and the age range of the NN 18 zone, the rapid sedimentation rate > ~600 m/m.y. is inferred for Unit 2 below the unconformity [Harris *et al.*, 2013].

Magnetic polarity sequences of normal polarity (Unit 3) and reverse polarity (Units 1 and 2) were defined from shipboard paleomagnetic measurements, and the Matsuyama/Gauss Chron boundary (~2.581 Ma), the Reunion Subchron (2.128–2.148 Ma), and the Olduvai Subchron (1.778–1.945 Ma) have tentatively been placed based on normal polarity intervals at the depth range of ~770 mbsf (Unit 2/3 boundary), ~730–764 mbsf, and 633.91–666.61 mbsf, respectively [Harris *et al.*, 2013]. Above 633.91 mbsf and throughout Unit 1, geomagnetic polarity timescales were not defined because of limited data points, and shore-based paleomagnetic studies are ongoing to improve the tentative magnetostratigraphy at Site 1380. In the present study, I refer mainly to the age range defined by nannofossil records, which has a relatively more continuous dataset.

The downhole profiles of the pore water geochemistry in Unit 1 show decreases in Cl, salinity, K, and Mg and increases in Ca and Li, especially along the fault zone adjacent to the unconformity [Harris *et al.*, 2013] (Figure 15). These trends indicate the interaction and dilution of the pore fluid at present with a fresher fluid (36%–39% fresher than

modern seawater) that has migrated from a deeper region with temperatures high enough to support smectite dehydration ($> 60^{\circ}\text{C}$) [e.g., *Perry, 1970; Bekins et al., 1994*].

2.3.3 Physical property contrast across the unconformity and the seismic reflectors observed at Site 1380

Sharp discrete boundaries in shipboard measurements of porosity, P-wave velocity, natural gamma rays, and magnetic susceptibility exist across the major unconformity at ~552 mbsf between Units 1 and 2, the boundary at ~707 mbsf within Unit 2, and the boundary at ~772 mbsf between Units 2 and 3 [*Harris et al., 2013*] (Figure 16). Units 2 and 3 have lower values of porosity (~22%–37%) compared to Unit 1 (~41%–71%) on average, and the porosity is slightly increased (~28%–33%) at 700 mbsf (Figure 16). Corresponding to the porosity, the sample bulk density is lower (~1460–2040 kg/m³) for Unit 1 than Unit 2 and 3 (~2070–2280 kg/m³), whereas the grain density is relatively consistent throughout the depth.

Above the unconformity, the P-wave velocities measured from discrete samples of Unit 1 (~1540–1920 m/s) are higher than those of Units 2 and 3 (~2060–2560 m/s), and the velocity increases slightly at Unit 3 (~2210–2460 m/s). Natural gamma ray values obtained by a multi-sensor core logger (MSCL) are higher and increase with depth for Unit 1 (~9–30 cps) compared to the stable values of Units 2 and 3 (~11–20 cps). The high spikes (~46 cps) especially in Unit 1 may correspond to white siliceous ash layers measured in the recovered cores. The magnetic susceptibility measured by the MSCL is relatively consistent throughout the depth (~12–68 IU), occasionally exhibiting high spikes (~340–450 IU) especially in Units 2 and 3 which may correspond to black mafic ash layers.

Shipboard measurements indicated that the thermal conductivity ($\sim 0.81\text{--}1.64$ W/(m·K)) varies inversely with porosity and steps to higher values at the boundary between Units 1 and 2 [Harris *et al.*, 2013] (Figure 16, 17). Temperatures were measured between 0 and 120 mbsf at Site 1378B and a heat flow of 0.0442 was estimated [Vannucchi *et al.*, 2012]. The downhole temperature-depth relation was extrapolated using the Bullard [1939] method and two models for the variation of thermal conductivity with depth (Figure 17). The first model assumes a linear increase of thermal conductivity with depth provided by a least-squares fit, and the second model is based on the thermal resistance obtained from each measured thermal conductivity value [Harris *et al.*, 2013]. It is notable that the downhole temperatures used for estimating the temperature gradient were from a shallow depth (<120 mbsf), and might not reflect the thermal perturbation at greater depths.

Although geophysical logging data were not available at Site 1380 and it is difficult to construct synthetic modeling to compare with seismic reflection data, the physical property contrast observed from sample measurements suggested distinctive correlations with seismic reflectors at this horizon (Figure 16) [Harris *et al.*, 344]. The most characteristic physical property transition between Units 1 and 2 corresponds to the major seismic reflector above the acoustic basement at ~ 550 mbsf, whereas the contrast observed at ~ 700 mbsf within Unit 2 corresponds to the strong landward-dipping reflector at this depth range (Figure 16). The physical property contrast observed across the Unit 2/3 boundary is likely to correspond to the moderately strong landward-dipping reflector at ~ 770 mbsf (Figure 16).

2.3.4 Lithology, structure, and physical properties observed at CRISP Upper-slope

Site 1379 and Site 1413

Site 1379 was drilled into the upper slope of the Costa Rica margin, 34 km offshore Osa Peninsula and 16 km from Cano Island along seismic BGR99 Line 7 at the water depth of ~127 m [Ranero *et al.*, 2008; Vannucchi *et al.*, 2012] (Figure 8). Site 1379 is located above the region of the seismogenic zone observed during the aftershock sequence of the 2002 M6.4 Osa earthquake along the plate boundary that is 4.5 km below the seafloor [Arroyo *et al.*, 2014; Vannucchi *et al.*, 2012]. Geodetic measurements indicated that this drilling area is situated above the locked portion of the plate boundary [LaFemina *et al.*, 2009; Vannucchi *et al.*, 2012]. Five lithologic units were identified in the cores recovered from 0–949 mbsf [Vannucchi *et al.*, 2012]: Unit 1 of coarse sand (Pleistocene–recent), Unit 2 of clay(stone), silt(stone), and sand(stone) (early Pleistocene), Unit 3 of fine to medium sandstone (early Pleistocene), Unit 4 of carbonate-cemented shell-bearing sand (late? Pliocene), and Unit 5 of poorly sorted matrix-supported breccia (late Pliocene).

The major seismic reflector corresponds to the boundary penetrated between Units 3 and 5 across the ~1.85-m-thick unconsolidated sand layer of Unit 4 that is indicated to be beach deposits, and a clear physical property transition was observed across the unconformity at 881.75 mbsf. Shipboard physical property measurements revealed a porosity decrease of 16% between Unit 3 (~33%) and Unit 5 (~17%) and a sharp P-wave velocity increase from ~1800 m/s to ~2300 m/s, respectively. Logging-while-drilling operations were also conducted at Site 1379, and a clear physical property contrast is identified similarly from the density, neutron porosity, and ultrasonic caliper measurements recorded by the Schlumberger logging-while-drilling (LWD) tool string [Vannucchi *et al.*, 2012]. The lithified sediments and slope sediments exist above the late

NN 17 zone (2.46–2.56 Ma) at the upper slope, but the low nannofossil abundance across the unconformity made it impossible to detect the NN 18 zone below the NN 19 zone (~1.59 Ma). Based on the age range of each NN zone, the age gaps across the unconformity are estimated to be less than ~0.97 m.y. (2.56–1.59 Ma) for the upper slope. Based on the nannofossil records, the estimated average sedimentation rates are > 1035 m/m.y. for the uppermost ~566 mbsf and > ~160 m/m.y. between ~566 and ~722 mbsf [Vannucchi *et al.*, 2012].

Site 1413 is located on the upper slope of the Costa Rica margin 30 km from the trench within the 3-D seismic data set along Line 2466 and crossing Line 4882 at the water depth of ~540 m [Kluesner *et al.*, 2013; Bangs *et al.*, 2015, Harris *et al.*, 2013] (Figure 8). Interplate earthquake relocations and geodetic measurements have shown that this site is located above the region of the seismogenic zone observed in recent earthquakes [Bilek *et al.*, 2003; LaFemina *et al.*, 2009; Harris *et al.*, 2013]. Three lithologic units were defined from the recovered cores from 0 to 582.2 mbsf [Harris *et al.*, 2013]: Unit 1 of silty clay with sand (late Pleistocene to Holocene), Unit 2 of calcareous clayey silt/stone and minor sand/stone (mid- to late Pleistocene), and Unit 3 of fine to medium sandstone (early to mid-Pleistocene). The major seismic reflector was not penetrated at this site, and no significant physical property transitions were observed.

3. Methodology

In the present study, to investigate the nature of the seismic reflectors in the forearc wedge, the high consolidation state of the upper plate material, and the roles of fluids at the Costa Rica margin and to quantify the deformation events during seamount subduction, I focused on the consolidation process and physical property transitions of the sediment samples that correlate with the seismic reflectors across the major unconformity and examined the burial condition and the maximum burial depth range of the sediments below the unconformity, focusing on the middle-slope Site 1380 drilled during IODP Expedition 344. I evaluated and quantified the geologic events of uplift, material removal and subsidence during the Cocos Ridge subduction by studying the porosity-depth transition and consolidation curve across the major unconformity beneath the slope of the Costa Rica margin.

I conducted microstructural observations and a particle size analysis of middle-slope Site 1380 to study the compaction texture of the sediments across the unconformity and physical property transitions. I analyzed shipboard physical property measurement data (porosity, velocity, density, natural gamma rays, thermal conductivity, magnetic susceptibility, and the thermal gradient), conducted resistivity measurements, and developed physical property relationships to evaluate the consolidation trend of the sediments. To examine the possible conditions for burial diagenesis and sediment-fluid interaction, I studied the major element/mineral components of the sediments focusing on the primary diagenetic minerals (zeolite and clay mineralogy) by conducting X-ray fluorescence/diffraction analysis.

I examined the effects of the burial diagenesis and sediment-fluid interaction findings on the porosity, and evaluated the consolidation curve during burial. For the

quantification of the conditions for uplift, material removal and subsidence, I obtained the maximum burial depth range of the sediments from the consolidation curve derived from the porosity-depth transition and zeolite mineral assemblage.

3.1 Shipboard physical property measurements during IODP Expedition 344 (conducted with the physical property group during the cruise)

Porosity measurement

Discrete sample porosity, bulk density, and grain density were measured via mass and volume determinations using the dual-balance system and a pycnometer with six cells equipped on the ship (the JOIDES Resolution) during the Expedition. Sediment mass and dry volume in cylinders were determined by measuring the mass and volume of the cylinders. The traditional Ocean Drilling Program (ODP) method (Method C) from *Blum* [1997] was used for the calculation of the sediment bulk density, dry density, grain density, porosity, and void ratio. The determination of the water content was based on the methods of the American Society for Testing and Materials (ASTM) designation D2216 [*ASTM International*, 1990].

P-wave velocity measurement

P-wave velocity was measured using an *x*-axis caliper-type contact probe with one plastic transducer contact on the sample split core and the other contact against the core liner. Panametrics-NDT Microscan delay line transducers were used in the system, transmitting at 500 kHz.

Thermal conductivity measurement

Thermal conductivity was measured using the half-space line source [Vacquier, 1985] for the consolidated sediments, which approximates the heating element of an infinite line source [Blum, 1997]. Measurement was made on the sample split core in half-space mode [Vacquier, 1985].

Additional shipboard methodology for the other physical properties (magnetic susceptibility, natural gamma rays, vane shear, shear strength, luminescence) are described by Harris *et al.* [2013] (Expedition 344 Proceedings, Methods Chapter).

3.2 Laboratory methods (post-cruise research conducted by the author)

Resistivity measurement

Electric resistivity was measured using an Agilent 4294A component analyzer equipped at the Kochi Institute for Core Sample Research (KCC) based on the bridge method with a two-terminal circuit for cubic samples. Twenty-five discrete sediment samples from Site 1380 were cut in specimen cubes parallel to the depth (z) direction of the borehole, and the horizontal plane was polished for measurement. Parafilm was wrapped around the oriented samples to avoid breaking during polish. Samples were impregnated with seawater for 10 hours, and a resistivity measurement was taken every 1.5 hours. After compensating for the infinite (Open) and zero (Short) impedance of the inductance (L), capacitance (C), and resistance (R) (LCR) meter, the oriented samples were placed between two brass electrodes covered with filter papers saturated in seawater and sandwiched between two insulated rubber pads as the outer layer. A 0.3-kg weight was placed on top of the rubber pad to ensure that the electrode and sample were in complete contact. The magnitude ($|Z|$) and phase (θ) of the complex impedance were

measured at 10 kHz and 1000 mV between opposite cube faces in the z direction (parallel to the depth). The electrical resistivity for the z direction (i.e., R_z) was computed from the complex impedance measured along the oriented direction and the sample dimension defined by face lengths (L):

$$R_z = |Z_z| \cos \theta_z \left(\frac{L_x L_y}{L_z} \right)$$

Physical property cross-correlation (resistivity-porosity, velocity-porosity)

The delineation of the physical property relationships versus porosity with hydrologic and elastic properties such as P-wave velocity, electric resistivity, and permeability provide consolidation curves that are useful for: (1) estimating unknown properties, (2) understanding the effects of pore structure, particle size (clay content), lithology, and geochemical properties on consolidation, and (3) comparing these characteristics among different sediment compositions, textures, and pressure-temperature (P-T) conditions [e.g., *Erickson and Jarrard*, 1998; *Hoffman and Tobin*, 2004; *Hamahashi et al.*, 2013; 2015; *Daigle and Sreaton*, 2015].

I used cross-plots of porosity and resistivity to determine the cementation exponent and consolidation state of sediments [e.g., *Ewing and Hunt*, 2006; *Montaron*, 2009; *Kozlov et al.*, 2012] across the lithologic units. The approximate correlation between porosity and resistivity is empirically known as Archie's law [*Archie*, 1942], which is formulated as:

$$F = R_{eff} / R_f = b \phi^{-m}$$

where F is the formation factor, R_{eff} is the resistivity of fluid-saturated rock, R_f is

the resistivity of the fluid within the rock, ϕ is the porosity of the rock, and b and m (“cementation exponent”) are fitting parameters.

I used the cross-plots of P-wave velocity and porosity to examine the consolidation trends subjected to various ranges of P-T conditions and different compositions [e.g., *Erickson and Jarrard, 1998; Hoffman and Tobin, 2004*].

Optical microscope

I examined 84 samples with an optical microscope (BX51TRD, OLYMPUS) equipped at the University of Tokyo. Core samples were first impregnated with resin and then cut in two directions: parallel and horizontal to the depth direction in the borehole. Oriented samples were then polished and occasionally impregnated with additional resin, and then made into thin sections for microstructural observations in the vertical and horizontal directions for each sample.

Field emission scanning electron microscopy (FE-SEM) and energy dispersive X-ray spectrometry (EDS)

Fourteen samples and thin sections were examined using a Hitachi S-4500 field emission scanning electron microscope (FE-SEM) equipped at the University of Tokyo. Secondary electron and backscattered electron imaging were used to determine texture, particle shape and size, and mineralogy. The standard operating conditions were 15 kV acceleration voltage and 15 μ A emission current. For the secondary and backscattered electron imaging, samples and thin sections were first impregnated with resin for polishing and then carbon-coated prior to the measurements. Qualitative and quantitative elemental analyses of selected phases were performed using energy-dispersive X-ray

spectrometer (EDS). The secondary and back-scattered electron imaging were conducted in the vertical and horizontal directions for each sample.

Particle size measurement

I analyzed 153 samples for the particle size measurement, using a Malvern Mastersizer 2000 laser diffraction particle size analyzer equipped at KCC. Samples were dispersed with water and propan-2-ol (isopropyl-alcohol) in a beaker and then placed in an ultrasonic bath for 30–50 minutes. The detector array consisting of many individual detectors within the optical bench of the Mastersizer collects the light scattering from a particular range of angles, and prepared samples were delivered to the optical bench where the light-scattering pattern was captured for each sample. The detector array takes 2,000 snapshots of the scattering pattern for each measurement and averages the results. The raw data were analyzed to quantify the particle sizes using the Malvern software based on the Mie theory, which predicts the light scattering behavior of spherical particles.

X-ray fluorescence (XRF) analysis

The concentrations of 10 major elements (SiO₂, TiO₂, Al₂O₃, Fe₂O₃, MnO, MgO, CaO, Na₂O, K₂O, and P₂O₅) in 44 samples from Site 1380 were determined by an X-ray fluorescence (XRF) analysis of fused glass disks, using an XRF spectrometer PANalytical Axios equipped with an Rh tube at the University of Tokyo. Each sample was ignited at 1100°C prior to making the fused glass disk, and the loss on ignition (LOI) was then calculated. The measurement settings were at 60 kV and 66 mA for Fe₂O₃ and MnO, at 40 kV and 100 mA for TiO₂, and at 32 kV and 125 mA for SiO₂, Al₂O₃, MgO, CaO, Na₂O, K₂O, and P₂O₅. The measurement time was 3 minutes and 40 seconds for each sample.

The 1σ relative standard deviation of the measurements were $\pm 0.050\%$ for SiO_2 , $\pm 0.005\%$ for TiO_2 , $\pm 0.024\%$ for Al_2O_3 , $\pm 0.007\%$ for Fe_2O_3 , $\pm 0.001\%$ for MnO , $\pm 0.010\%$ for MgO , ± 0.010 for CaO , $\pm 0.013\%$ for Na_2O , $\pm 0.007\%$ for K_2O , and $\pm 0.002\%$ for P_2O_5 .

Since Al_2O_3 is more abundant in detrital sources than in biogenic sources, I used the cross-plots between Al_2O_3 and the other nine major elements to determine the elements contained in the detrital and biogenic components.

X-ray diffraction (XRD) analysis

The relative mineral proportions in 44 bulk samples recovered from Site 1380 were examined from powder X-ray diffraction (XRD) patterns which were recorded using a PANalytical X'Pert PRO MPD X-ray diffractometer system with $\text{CuK}\alpha$ radiation at the University of Tokyo. The measurements were taken at 45 kV and 40 mA, with 0.8-mm-thick 0.25° and 0.3-mm-thick 0.125° divergence slits, a 6-mm-thick anti-scattering slit and a receiving slit, at a scan rate of 0.006° per minute at a scan step of 0.008° in 2θ , over a 4° – 34° 2θ range. Diagnostic reflections from individual mineral species were processed (with linear background subtraction and the assessment of the integrated peak intensity) by using the standard PANalytical peak analysis software.

To identify the two different types of zeolite minerals, i.e., heulandite and laumontite, I distinguished the intensity peaks from clinoptilolite and plagioclase respectively, bearing in mind that heulandite and laumontite should break down at $\sim 250^\circ\text{C}$. Representative samples from each lithostratigraphic unit were selected for measurement and the bulk powders were heated in an oven at 350°C for 8 hours. I compared the XRD patterns for the heated and non-heated samples to distinguish the peak between heulandite and clinoptilolite at $9.91^\circ 2\theta$ and the peak between laumontite and plagioclase at $12.45^\circ 2\theta$.

For the clay mineral analysis, representative samples from each lithostratigraphic unit were selected for measurement and the bulk powders were gently crushed and then dispersed ultrasonically in distilled water. The clay fraction at $<2.0\ \mu\text{m}$ particle size was separated by centrifugation. Clay suspensions were washed in distilled water and carefully dropped onto glass slides to prepare oriented mounts by air-drying on a hot-plate at 60°C . These mounts were subsequently saturated with ethylene-glycol vapor in an oven at 50°C for 3 hours. For a different set of the same samples, the oriented mounts were saturated with hydrochloric acid and air-dried on a hot-plate at 60°C for 5 hours. Generally, chlorite is known to dissolve in acid whereas kaolinite does not, and this technique was applied to distinguish the intensity peak between chlorite and kaolinite at $12.5^\circ 2\theta$, referring to the solubility of clay minerals in acid.

The XRD patterns for the oriented mounts were recorded using a PANalytical X'Pert PRO MPD system with $\text{CuK}\alpha$ radiation at 45 kV and 40 mA, with 0.8-mm-thick 0.25° and 0.3-mm-thick 0.125° divergence slits, a 6-mm-thick anti-scattering slit and a receiving slit, at a scan rate of 0.03° per minute at a scan step of 0.008° in 2θ , over the 3° – 23° 2θ range. The expandability of smectite in a chlorite-smectite mixed layer is proportional to the abundance of smectite, and this was determined from the saddle/peak ratio of 001 reflection in the ethylene-glycol-treated XRD pattern. The presence of smectite and chlorite was identified from the peaks at $6.28^\circ 2\theta$ by conducting the heated (350°C) sample measurements described above, referring to the fact that smectite will disappear when heated and will be shifted to $8.92^\circ 2\theta$ while chlorite remains.

For the quantitative analysis of XRD patterns of zeolite (analcime, laumontite, and heulandite), I prepared samples mixed with standards of analcime, laumontite, and heulandite of known weight, and conducted XRD using the natural samples and standard-

mixed samples. Each zeolite standard was preheated in an oven at 60°C for 6 hours, and the weight of the standard was measured before it was blended into each natural sample. Representative samples from each lithostratigraphic unit were selected and the XRD patterns for the standard-mixed samples were recorded in the same measurement setting as that used for the bulk sample measurement. The zeolite abundance in each natural sample was obtained from the relationship between the intensity of diagnostic reflection and the weight % of each zeolite by plotting the results from the standard-mixed samples and natural samples.

To investigate the lateral variation of the mineral composition of the sediments at the slope, I compared the mineral compositions between the middle and upper slopes by conducting XRD measurements on four samples at the drilled range of 0–584 mbsf at the upper-slope Site 1413, using the same method as that applied for the Site 1380 samples.

4. Results and Discussion

The data presented here are post-cruise research data obtained by the author except for the shipboard physical property measurements: porosity, P-wave velocity, thermal conductivity, and the thermal gradient.

4.1 Consolidation trend based on microstructural observations and physical properties

Based on my microstructural observations of representative samples, it was apparent that the Unit 1 sediments consist of large-particle-sized lithic fragments with various major minerals such as smectite, chlorite, quartz, plagioclase, and calcite, and zeolites (laumontite and heulandite) as minor minerals (Figure 18). Sand tended to increase in abundance and particle size with depth in Unit 1.

Across the unconformity, where the porosity decreases significantly in Unit 2, the sediments are more indurated and dewatered than in Unit 1, and a sharp contrast in microstructure is observed (Figure 19). Below the unconformity, zeolites (analcime, laumontite, and heulandite) are present as major minerals, existing as pore-filling materials within the sediments of Units 2 and 3. Siltstone, sandstone, and conglomerate layers are moderately cemented by calcite, and the coarse-grained lithic and biogenic materials tend to build cohesive microstructures where they are common. The fine grained clay-rich samples contain abundant lithic fragments that form a less cohesive texture where they are sparser, and a more cohesive structure where they are denser.

Across the slight porosity increase within Unit 2 at ~700 mbsf, a gradational transition in microstructure is observed, where the lithic fragments become smaller and form cohesive structures (Figure 20). The microstructure of representative samples from

Unit 3 gradually change to a more homogeneously dense texture formed by smaller lithic fragments, where coarse sands are less abundant and grains are well-sorted (Figure 20).

The grain sizes of the sediments obtained from the particle size analyses do not vary significantly with depth, indicating that the lithology dependence on the porosity-depth transition is minimal (Figure 21). The overall clay/silt/sand volume % of the sediments derived from particle size analysis range from ~60% to 75%, ~25% to 30%, and ~10% to 25% respectively throughout the depth at all intervals (Figure 21). The grain size distribution is larger in number for the finer particle sizes, suggesting that finer grains and minerals may contribute to compaction, e.g., by filling pores between larger grains (Figure 21). In light of these observations, I suggest that the lithology difference along the depth is minimal, and the major factors that control the porosity-depth curve/transition of the sediments are burial compaction and consolidation.

4.1.1 Zeolite precipitation as pore-filling minerals

However, the decrease in porosity with depth and the consolidation state of the sediments is not accounted for by only burial compaction. Under the optical and scanning electron microscope, the zeolites analcime ($\text{NaAlSi}_2\text{O}_6 \cdot \text{H}_2\text{O}$), laumontite ($\text{CaAl}_2\text{Si}_4\text{O}_{12} \cdot 4\text{H}_2\text{O}$), and heulandite ($(\text{Ca}, \text{Na}_2)\text{Al}_2\text{Si}_7\text{O}_{18} \cdot 6\text{H}_2\text{O}$) were observed to precipitate as pore-filling minerals and veins in the sediments (Figure 22). Analcime is present mainly as ~50- μ m-sized particles only in Units 2 and 3, precipitating in pores among lithic fragments and in shells of nannofossil, diatom, foraminifera. Heulandite and laumontite are present in much smaller crystal size compared to analcime, and are precipitated occasionally in shells and pores between particles and as veins in Units 1, 2

and 3, where laumontite is observed mainly in Unit 1 and upper Unit 2. The crystal geometry of the analcimes that are precipitated in shells and pores between particles are not angular and exhibit smooth outlines, indicating slow formation during burial diagenesis rather than rapid precipitation from an external source. In addition to burial compaction, the consolidation state of the sediments is likely to be controlled by the precipitation of these minerals. Investigations of the precipitation conditions of these minerals would provide information on the mineral diagenesis, burial temperature, and fluid-sediment interaction of the sediments, which is examined in Section 4.2 below.

4.1.2 Cross-correlation of physical properties

To determine the consolidation curve and the relationships among the geophysical signatures and lithologic units, I examined the cross-plots of physical properties among porosity, P-wave velocity, and resistivity (formation factor) obtained from the shipboard discrete measurements (Figure 23) and the discrete sample measurements in this study (Figure 24).

The cross-plot between porosity and P-wave velocity does not change significantly across the unconformity, and is relatively consistent among Units 1, 2, and 3 (Figure 23). The velocity values of Unit 1 can be fit by the empirical relationship described by *Hoffman and Tobin* [2004] from the underthrust sediments in the Shikoku basin of the Nankai Trough drilled during Ocean Drilling Program Legs 131, 190, and 196. In contrast, the values of Units 2 and 3 plot above the curve (Figure 23). This may indicate the normal consolidation state in Unit 1 and higher consolidation state in Units 2 and 3 in reference to the Shikoku basin sediments.

The electrical resistivity values obtained from the discrete sample measurement in

the present study are higher in Units 2 and 3 (~1.62–4.28 Ωm) compared to Unit 1 (~1.53 Ωm) (Figure 24). The porosity and resistivity in Units 1, 2, and 3 each show a negative or power law relationship, and the cross-plot at this interval is well fit by Archie's law [Archie, 1942] with $m=1.36$ (Figure 24). The resistivity at Site 1380 are plotted with relatively high m values above the normal compaction curve, indicating high consolidation in the porosity range of ~20%–55%.

4.2 Element and mineral compositions of the sediments

The results of the XRF analysis revealed that Al_2O_3 , K_2O , TiO_2 tend to concentrate in the higher-porosity sediments of Unit 1, whereas SiO_2 , CaO , P_2O_5 , MgO , Na_2O , and MnO concentrate in the lower porosity sediments of Units 2 and 3 (Figure 25). Across the porosity increase within Unit 2, CaO is less abundant with the increases in SiO_2 and K_2O (Figure 25). However, these differences in element composition are minimal, and the overall geochemical compositions among Units 1, 2, and 3 are not significantly different, except for the contrast in Al_2O_3 between Units 1 and 2.

Though the cross-plots between Al_2O_3 and the other nine major elements are relatively scattered, nearly all elements (as oxides) except for CaO show a positive correlation with Al_2O_3 in Units 1, 2, and 3 (Figure 26). The elements with a positive correlation are likely contained in the detrital component which has abundant Al_2O_3 , whereas the element with a negative correlation (CaO) is likely to be affected by a biogenic or diagenetic component devoid of Al_2O_3 .

Typical examples of bulk XRD for the sediment samples are shown next to the lithostratigraphic column in Figure 27. Major mineral components of the sediments are phyllosilicates including chlorite and smectite, quartz, plagioclase, calcite, and zeolite.

Zeolites appear as minor minerals in Unit 1, whereas they are abundant in Units 2 and 3. Unit 2 is characterized by the appearance of a zeolite-type mineral, analcime, and in Unit 1 analcime is rare to absent. The black lines in Figure 27 represent the samples before heating, and the red lines are measurements taken using the heated samples. I consider the two peaks at 9.91° and $11.18^{\circ}2\theta$ to represent laumontite and heulandite because they disappeared when heated (Figure 27).

The mineral components across the unconformities are marked by the transitions in zeolite composition among the Na-type zeolite analcime, the Na/Ca-type zeolite heulandite and the Ca-type zeolite laumontite. The zeolite composition in Unit 1 consists of heulandite and laumontite, and below the unconformity in Unit 2, the sediments consist of heulandite, laumontite and analcime (Figure 27). Below the porosity increase in Units 2 and 3, laumontite is less abundant, and heulandite and analcime become the major zeolites (Figure 27). The quantitative bulk analyses for representative samples from each lithostratigraphic unit revealed that the weight percentages of heulandite and laumontite in Unit 1 range from $\sim 1.0\%$ to 1.1% and from $\sim 3.2\%$ to 4.5% , respectively, whereas those of analcime, heulandite and laumontite in Unit 2 are $\sim 6.1\%$ to 7.2% , $\sim 1.2\%$ to 1.6% , $\sim 2.2\%$, respectively. In Unit 3, the weight percentages of analcime and heulandite are $\sim 7.9\%$ and $\sim 1.2\%$, respectively (Figure 28).

I identified the peak at $6.28^{\circ}2\theta$ as a mixed layer of smectite and chlorite, since the peak did not disappear with heating, indicating both the presence of chlorite and that smectite had shifted from $6.28^{\circ}2\theta$ to $8.92^{\circ}2\theta$ (Figure 27). In the clay-fraction XRD of the sediment samples, the peak at $6.28^{\circ}2\theta$ shifted to $5.15^{\circ}2\theta$, indicating the presence of smectite. Chlorite is likely to be rare in the clay-fraction of this peak, but is likely to be more abundant in the silt/sand-fraction. Smectite had higher expandability after the

ethylene-glycol treatment of the Unit 1 samples compared to those of Units 2 and 3 (Figure 27), indicating that pure smectite is more abundant in Unit 1.

4.2.1 Experienced temperature range of sediments and precipitation conditions of zeolite assemblages

In a wide range of environments from shallow surfaces to hot hydrothermal alterations and to deeper burial depths, zeolites generally form from volcanic glass in ashes and vitric tuffs, and then ultimately change to thermodynamically stable alkali feldspars or other non-zeolite minerals through intermediate zeolites such as Na-type zeolites (e.g., analcime) and Ca-type zeolites (e.g., laumontite), and Na/Ca-type zeolites (e.g., heulandite) [e.g., *Iijima*, 1986]. These zeolite reactions in different types of events create a characteristic zonal distribution of unaltered glass zones, zeolite zones, and authigenic feldspar zones attributing to the environment's geothermal and/or geochemical gradients [e.g., *Coombs et al.*, 1959; *Iijima and Utada*, 1972; *Iijima*, 1986; *Yoshimura*, 1994; *Ogiwara*, 1996] (Figure 29).

In marine sediments, the vertical zonal distribution is produced primarily in response to the geothermal gradient during burial diagenesis and/or hydrothermal alteration. At $\sim 50^{\circ}\text{C}$, volcanic glass dissolve, hydrolyze and produce pores where clinoptilolite and mordenite precipitate within [*Iijima*, 1986]. The clinoptilolite and mordenite transforms to analcime and heulandite at temperatures between $86^{\circ}\pm 5^{\circ}\text{C}$ and $122^{\circ}\pm 2^{\circ}\text{C}$, whereas laumontite is formed at temperatures higher than 100°C , and at temperatures over $122^{\circ}\pm 2^{\circ}\text{C}$, analcime changes to albite [e.g., *Iijima*, 1986; *Ogiwara*, 1996] (Figure 29).

The Na-type zeolite analcime, Na/Ca-type zeolite heulandite, and Ca-type zeolite

laumontite are likely to form under different source and conditions. At $86^{\circ}\pm 5^{\circ}\text{C}$ ~ $122^{\circ}\pm 2^{\circ}\text{C}$, the Na-type zeolite analcime is reported to transform from clinoptilolite through micro-dissolution-precipitation stimulated by the increase of temperature and Na ion ratio in pore water [e.g. *Ogiwara*, 1996]. The Na/Ca-type zeolite heulandite in contrast, is known to transform from clinoptilolite by an interaction with Ca-rich pore water through microdissolution-precipitation, starting from a relatively higher temperature than that of analcime [e.g. *Ogiwara*, 1996]. The Ca-type zeolite laumontite is likely to form under higher temperature ($>\sim 100^{\circ}\text{C}$) than that of analcime and heulandite, requiring a source abundant in Ca, such as Ca-rich pore water and/or dissolved carbonates.

The reported temperature ranges of the zeolites [e.g. *Iijima*, 1986] is based on 10 boreholes from hydrocarbon explorations from on-land and offshore freshwater/seawater environments selected as the best natural laboratory where active burial diagenesis and fluid-sediment interaction of the zeolites were observed. Owing to the temperature-dependency of zeolite formation, the zeolite assemblage produced (especially during burial diagenesis) is broadly applied as a geothermometer to conduct sedimentary basin analysis, thermal history estimation and evaluation of thermal aging of organic materials [*Nishimura et al.*, 1980].

The present study's mineral analyses revealed that analcime is present only in Units 2 and 3, exhibiting a microstructure indicative of precipitation during burial diagenesis as described in Section 4.1.1 above. Heulandite and laumontite, in contrast, are present in both Units 1 and 2, and are likely to originate from different source and mechanism with analcime. Heulandite exist in Units 1, 2, and 3, and laumontite is distributed mainly in Unit 1 and the upper Unit 2 below the unconformity. Heulandite and laumontite exhibit much smaller crystal size compared to analcime, occasionally existing in veins. The Na-

type zeolite analcime, the Na/Ca-type zeolite heulandite and the Ca-type zeolite laumontite coexist, despite their generally different origins and formation mechanisms. Answering the question of how these different types of zeolites formed and coexist, in relation to the source materials, provide important information about the geologic processes that these sediments have undergone. The observations in the present study indicate that analcime was produced due to burial diagenesis from volcanic glass, whereas heulandite and laumontite are not likely to have formed from burial diagenesis with analcime but were instead formed through different source through high-temperature fluid-interaction.

Other than the changes described for the zeolites, the sediments do not exhibit significant changes in mineral assemblage (Figure 27), indicating that the observed analcime, laumontite and heulandite are not detrital, and thus are not likely to originate from a debris flow. This is also supported by the relatively low thermogenic stability of these minerals [e.g., *Iijima*, 1986; *Yoshimura*, 1994; *Ogiwara*, 1996].

In light of these observations and from the burial diagenetic temperatures of analcime below the unconformity, the experienced maximum temperature of the sediments in Units 2 and 3 can be estimated to range between $86^{\circ}\pm 5^{\circ}\text{C}$ and $122^{\circ}\pm 2^{\circ}\text{C}$. These temperatures are above the in situ temperatures of $\sim 25^{\circ}\text{--}32^{\circ}\text{C}$ in the drilled depth range (~ 800 mbsf) derived from the currently reported geothermal gradient ($\sim 51.4^{\circ}\text{C}/\text{km}$) (Figure 17, 30). This suggest that the sediments of Unit 2 and 3 have once been buried deeper than their current depth ($\sim 550\text{--}800$ mbsf) and experienced heating. The maximum burial may have occurred at the depth range of $\sim 1600\text{--}3000$ mbsf, if assuming a constant thermal gradient and a constant heat flow with depth (Figure 30). The inferred temperature range is also supported by the low expandability of smectite in Units 2 and 3

compared to Unit 1 and the presence of mixed layers of smectite and chlorite (Figure 27). The high paleo-temperature of the sediments are also consistent with the vitrinite reflectance studies by A. Sakaguchi's research group at Yamaguchi University [Sakaguchi and Yamashita, 2015]. After burial, the sediments of Units 2 and 3 are inferred to have reached their present depth through uplift and sediment removal.

These observations indicate that the porosity transition and physical property gaps across the unconformity were created by uplift, sediment removal and/or fault displacement, the deposition of slope sediments and subsidence. The necessary next step is an investigation using the porosity-depth curve on the burial depth range and the amount of uplift, sediment removal, and subsidence of the sediments. These are quantified in Section 4.3 below.

Laumontite and heulandite, on the other hand, are likely to have formed by accumulating Ca from sources such as dissolved calcite cements and/or precipitation from external fluid [e.g., Iijima, 1986; Ogiwara, 1996]. The formation of laumontite in Units 1 and 2 in the vicinity of the unconformity and heulandite in Units 1, 2, and 3 suggest that the sediments have been in contact with a high temperature (from $86^{\circ}\pm 5^{\circ}\text{C}$ to $122^{\circ}\pm 2^{\circ}\text{C}$) fluid migration before or after the initial burial (Figure 27, 29). This is supported by the shipboard pore water geochemistry results, which revealed signatures of a high-temperature fluid interaction ($>60^{\circ}\text{C}$) from a depth in Unit 1 along the unconformity [Harris *et al.*, 2013] (Figure 15). Furthermore, it is notable that laumontite is concentrated in the vicinity of the major unconformity and decreases with depth, which may have interacted with a higher temperature ($>\sim 100^{\circ}\text{C}$) fluid that has localized near the unconformity. The high-temperature fluid probably came from a depth through fault zones and erosional boundaries during the uplift and removal of the sediments in Unit 2,

warming the sediments at a relatively higher temperature than the geothermal gradient. The upward fluid flow from the depth may also require an overall uplift of the sediment column and/or a mechanism for trapped fluid isolated at depth but later released at shallower depths. The timing of the laumontite and heulandite formation in relation with the burial diagenesis of analcime, is yet to be clarified, however, and further microstructural observation is necessary to reveal whether the fluid-interaction occurred before or after initial burial.

The measured thermal gradient of the sediments estimated from the data at shallow depth [Harris *et al.*, 2013] appears to be unaffected by the presence of the warm fluids at depth identified in the drilled range (Figure 17). It may be possible that the fluid flow occurred and dissipated without affecting the shallow thermal gradient. In addition, the coexistence of smectite and zeolite in the inferred temperature range suggests that the mineral reaction rate of zeolites can be faster than that of clay minerals during the heating due to burial diagenesis and the fluid interaction suggested by the present study.

The initial analcime burial diagenesis of Units 2 and 3 is likely to have been cut off by the sediment removal across the unconformity between Units 1 and 2 during uplift, and it may have been affected by secondary consolidation due to interaction with high temperature fluid forming the laumontite and heulandite. The tectonic effect of uplift and sediment removal, geochemical alterations due to fluid flow, and their effects on consolidation are indicated by the mineral assemblages and microstructures across the unconformity, suggesting the need for a further evaluation of the material flux during these events from the porosity-depth transition (Next sections).

4.2.2 The effect of zeolite precipitation and sediment-fluid interaction on the porosity

decrease

The zeolites that were formed during burial diagenesis (i.e., analcime) likely precipitated in pores of dissolved volcanic glass, replacing the pre-existing materials. I consider in this study that the analcime formation due to burial diagenesis did not affect the porosity-depth curve during initial burial and that a secondary consolidation due to analcime is minimal. In contrast, the zeolites that were formed due to fluid-sediment interaction (i.e., laumontite and heulandite) likely precipitated along the fluid paths (e.g., pores and cracks) filling the initial porosity and contributing to a secondary consolidation. Therefore, if these zeolites (i.e., laumontite and heulandite) precipitated through a geochemical interaction with fluid ‘after initial burial’, they may have affected the primary porosity-depth curve of the sediments formed during the burial compaction.

In order to re-evaluate the burial compaction trend from the porosity-depth curve and to assess the burial depth range and the amount of sediment removal from the porosity-depth transition, it is necessary to quantify the effect of the fluid-interaction (laumontite and heulandite precipitation) on the porosity decrease. In this study, I calculated the amount of porosity filled by laumontite and heulandite in Units 1, 2 and 3 from the quantified weight percent of these zeolites (see Section 4.2 above). I then recalculated the porosity-depth curve of the sediments before the fluid-interacted zeolite precipitation, which would be the initial burial compaction trend if these zeolites formed after the burial.

The values of porosity filled by zeolites can be calculated using the following formula:

$$\phi_Z = (W_Z \div D_Z) \div (100 \div D_B) \div 100$$

where ϕ_Z is the porosity (%) filled by zeolite, W_Z is the weight percentage of zeolite,

D_z is the density of zeolite, and D_B is the bulk density of the sediments.

I quantified the porosity ϕ_z filled by laumontite and heulandite using W_z obtained from the quantitative bulk XRD analyses (Section 4.2 above), the D_z values of laumontite (2.3 g/cc) and heulandite (2.23 g/cc), and the D_B obtained from the shipboard measurements (~1.9–2.2 g/cc). The results from representative samples revealed that the porosity filled by laumontite is ~2.7%–3.8% in Unit 1 and ~2.1% in Unit 2, whereas heulandite fills ~0.9% in Unit 1, ~1.2%–1.6% in Unit 2 and ~1.1% in Unit 3 (Figure 28). The total amount of filled porosity due to zeolite formed during the sediment-fluid interaction (i.e., laumontite and heulandite) is ~3.6%–4.7% in Unit 1 and ~3.6% in Unit 2 near the unconformity (Figure 28). Below ~701 mbsf, laumontite decreases and the filled porosity due to heulandite is ~1.2% in Unit 2 and ~1.1% in Unit 3 (Figure 28).

The calculation of the porosity-depth curve before the fluid-interacted zeolite precipitation is possible by adding the porosity filled by the zeolites quantified above to the porosity of the natural samples. By using the representative values of the porosity filled by zeolites obtained for each lithostratigraphic unit (Figure 28), the modified porosity-depth curve is shifted to higher porosity above and below the unconformity, increasing the slope/inclination of the porosity-depth curve in Unit 1 (Figure 31).

4.3 The initial compaction curve derived from the porosity-depth transition and the maximum burial depth range below the unconformity

The consolidation trend in Units 1, 2, and 3 is controlled primarily by burial compaction and zeolite precipitation due to fluid-sediment interaction, and the initial porosity-depth curve due to burial compaction is not affected by the lithology differences

among Units 1, 2, and 3 as indicated by the microstructural observations and physical property cross-correlations (Section 4.1 above). Although rapid sedimentation throughout the sediments could cause under-compaction, it cannot explain the porosity difference between Units 1 and 2. The burial temperature ranges of analcime and heulandite in Units 2 and 3 indicate that these sediments were once buried at greater depths, and the events of uplift and sediment removal (erosion/fault displacement) occurred across the unconformity, creating the porosity transition and physical property gaps. The consistent burial compaction trend enables to assume a composite porosity-depth curve among Units 1, 2, and 3, and the maximum burial depth range of the sediments in Unit 2 can be estimated from the porosity gap.

Since the timing of the fluid interaction (laumontite and heulandite formation) in relation with the initial burial (diagenesis of analcime) is yet to be clarified, I considered the porosity-depth curve as the initial burial compaction trend in two cases in this study: porosity that includes and excludes the fluid-interacted zeolite (laumontite, heulandite) precipitation (hereafter referred to as ‘case A’ and ‘case B’ respectively), where case B uses the modified porosity-depth curve described in Section 4.2.2 above. If the fluid-interacted zeolites precipitated before burial, the initial burial compaction trend would correspond to the porosity-depth curve including these zeolites (case A), whereas if the zeolites precipitated after burial, the burial compaction trend would correspond to the modified porosity-depth curve that excludes the zeolite precipitation (case B). Here, B includes the case of fluid-sediment interaction occurring after burial in Unit 1 but might have occurred during burial or before maximum burial in Unit 2, since the sediments of Unit 2 have experienced a deeper region than Unit 1 where it is easier to have contact with high-temperature fluid.

The porosity-depth curve of the sediments is best-fit by an exponential curve [e.g., *Bray and Karig, 1985*], and the approximate curve in the present study obtained from Unit 1 (Figure 32) was formulated as:

$$\phi = 68.322e^{-0.00082278D} \quad (R=0.89), \text{ (with fluid-interacted zeolite, case A)}$$

$$\phi = 66.437e^{-0.0006548D} \quad (R=0.83), \text{ (without fluid-interacted zeolite, case B)}$$

where D is the depth from the seafloor (mbsf) and ϕ is the sediment porosity (%).

The approximate curve for Units 2 and 3 (Figure 32) was formulated as:

$$\phi = 48.08e^{-0.00047865D} \quad (R=0.34), \text{ (with fluid-interacted zeolite, case A)}$$

$$\phi = 62.224e^{-0.00090551D} \quad (R=0.60), \text{ (without fluid-interacted zeolite, case B)}$$

Units 2 and 3 have been buried deeper as indicated by the zeolite assemblage, and the burial depth range of these sediments can be estimated using the approximate porosity-depth curves of Unit 1 described above. The depth along the approximate curve of Unit 1 that corresponds to the porosity of the sediments at the top of Unit 2 corresponds to its maximum burial depth range below the unconformity.

The porosity range of the sediments below the unconformity were obtained from the maximum and minimum values of the data scatter range, which is 30.8%–37.6% for case A and 34.4%–41.2% for case B (Figure 33). In order to study the depth range along the porosity-depth curve of Unit 1 that corresponds to this porosity range below the unconformity (Figure 34), I predicted the range of data scatter along the approximate curve for case A and B from the measured data of Unit 1 (Figure 35). The depth along the approximate curve including the range of data scatter that matches the porosity range below the unconformity were 600–1200 mbsf for case A and 600–1400 mbsf for case B

(Figure 36). From these observations, the overall maximum burial depth range of the sediments below the unconformity is considered to be 1000 ± 400 mbsf. In the present study, I did not consider the effect of decompaction due to the relatively large error scales (~ 100 m).

This burial depth range is relatively shallower than the range estimated from the temperature range of analcime using the current temperature gradient (Section 4.2.1 above), possibly because the applied temperature gradient estimated using temperature measurements from the shallow depth does not reflect the thermal perturbation at greater depth (Section 2.3.3 above) (Figure 17). I propose that the depth range obtained from the porosity-depth curve in this study is more reliable than the estimates from the current thermal gradient. At this depth range, the sediments have likely experienced the maximum temperature of $86\pm 5^\circ\text{C} \sim 122\pm 2^\circ\text{C}$. This may also indicate that the paleo-isotherm may have ranged between $60^\circ \sim 200^\circ\text{C}/\text{km}$ with a relatively high maximum value.

4.4 The uplift, material removal, subsidence, and deposition inferred from the porosity-depth transition

As described in Section 2.3.1 above, an approx. 12-m-thick beach deposit consisting of unconsolidated sand layers with abundant shell fragments was found across the unconformity (Figure 13), indicating the uplift of sediments in Units 2 and 3 to sea level in the nearshore environment. An approx. 55-m-thick damage zone is also observed above the unconformity, exhibiting a normal stress field (Figures 13, 14), which suggests that normal faulting occurred during uplift. The sediments below the unconformity were situated at the maximum burial depth range of 1000 ± 400 mbsf and have likely uplifted to

the ocean surface and reached the current depth through sediment removal (surface erosion) and fault displacement.

An examination of the burial range, uplift, sediment removal, fault displacement, and subsidence of the sediments indicated by the zeolite assemblage can be performed based on the porosity gap across the unconformity and the burial compaction curve derived from the porosity-depth relationship of the sediments.

The porosity gap and missing material across the unconformity are probably due to surface erosion and/or normal fault displacement. If the missing material is due mainly to surface erosion (hereafter referred to as ‘Model 1’), the sediments below the unconformity were uplifted from the maximum burial depth to the sea surface, and the exposed sediments above the sea surface were removed through surface erosion such as landslide(s), followed by subsidence to the current depth and deposition of Unit 1 (Figure 37).

In contrast, if the missing material is due mainly to normal fault displacement (hereafter ‘Model 2’), the minimum uplift to the sea surface and the subsidence and deposition of Unit 1 were followed by normal faulting that uplifted Unit 2 to the current depth (Figure 37).

To evaluate these tectonic processes across the unconformity, I quantified the uplift, material removal, fault displacement, and subsidence that produced the porosity gap by considering the two models: Model 1 (maximum uplift and surface erosion, minimum normal faulting) and Model 2 (minimum uplift and surface erosion, maximum normal faulting) in Sections 4.4.1 and 4.4.2 as follows.

4.4.1 Model 1: Rapid, maximum uplift and material removal

The maximum burial depth range 1000 ± 400 mbsf of the sediments of Unit 2 that was indicated from the approximate curve of the porosity-depth transition extended to depth is likely to be the sum of the original thickness of Unit 2 before the uplift and the thickness of the missing material across the unconformity (Figure 38). After this burial, Unit 2 was uplifted, exposing the current top of Unit 2 to near sea level, and it gained the beach deposits in the nearshore environment (Figure 38). Assuming that the current water depth of ~ 500 m has been constant and that the seafloor is the depositional surface, the amount of uplift is estimated to be 1500 ± 400 m ($=1000\pm 400 + 500$ m) (Figure 38). During this uplift, the top of Unit 2 (i.e., the 1000 ± 400 m thick sediments) was removed through erosion, i.e., gravity collapse (e.g., a submarine landslide) and normal faulting (Figure 38).

From the core structural observation, the bedding of the sediments at Site 1380 generally dip between 10° and 30° northeast and southwest respectively [Harris *et al.*, 2013] (Figure 14, Section 2.3.2), and the current taper angle of the wedge offshore Osa Peninsula is $\sim 13^\circ$. Considering that the dip angle of the slope ranges between $\sim 10^\circ$ – 30° based on these observations, this thickness of mass movement would correspond to the distance of 4600 ± 3400 m parallel to the slope.

The age of Unit 2 below the unconformity is estimated as 2.20 ± 0.25 Ma based on the nannofossil record and magnetostratigraphy findings (Section 2.3.2 above). Therefore, the age of the sediments at the top of the missing intervals in Unit 2 is younger than 2.20 ± 0.25 Ma. This age range ($< 2.20\pm 0.25$ Ma) is likely to represent the timing of the start of the uplift and material removal events.

According to Model 1, after the uplift, material removal, and accumulation of beach deposits, Unit 2 subsided to its current depth: ~ 550 mbsf (Figure 38). Assuming that the

current water depth is constant and that the seafloor is the depositional surface, the thickness of the subsidence is estimated to be ~ 1050 m ($= \sim 550 + 500$ m) (Figure 38). The subsidence is likely to have been caused by basal erosion and/or fault displacement, as indicated by the observed fractured intervals above the unconformity. The deposition of Unit 1 (~ 550 m) occurred during this subsidence, and created the current porosity gap between Units 1 and 2 (Figure 38). The age of Unit 1 above the unconformity is estimated to range between 2.20 ± 0.25 Ma and 1.71 ± 0.24 Ma from nannofossil records (Section 2.3.2), and this age range is likely to correspond to the timing of the end of the uplift and erosion, and the start of subsidence.

The sediments below the unconformity preserves high paleo-temperature due to burial heating but may also have been subjected to high paleo-thermal gradient. Fluid flow that originated from the depth probably started during the events of uplift, erosion, and subsidence, which have likely flowed along weak planes of the fault zones and the unconformity. The contact with this high-temperature fluid caused the precipitation of zeolites (laumontite, heulandite) and likely caused a secondary consolidation of the sediments in Units 1 and 2.

Subsequent to the uplift, erosion, and subsidence, the sediments of Unit 2 originally at the depth of 1000 ± 400 mbsf were overall uplifted to ~ 550 mbsf in the current location (Figure 38). This model involves a rapid, maximum amount of uplift and material removal in a relatively short time frame, compared to Model 2 (see Section 4.4.2 below), and requires a larger sedimentation rate as discussed later in Section 4.6.

4.4.2 Model 2: Normal faulting, uplift, and minimum material removal

I consider here an alternative model (Model 2) that involves the least possible uplift

and material removal accommodated by the maximum amount of fault displacement.

According to this model, the sediments of Unit 2 below the unconformity were originally buried at the depth of 450 ± 400 mbsf ($=1000\pm 400 - 550$ m) prior to the uplift of the seafloor to sea level (Figure 39). Assuming that the current water depth of ~ 500 m is constant and that the seafloor is the depositional surface, the amount of uplift is estimated to be ~ 500 m (Figure 39). Here, beach sediments have deposited on top of Unit 2, without significant erosion.

The timing of the start of the uplift and exhumation which corresponds to the age of the sediments at the top of the missing intervals in Unit 2 is less than 2.20 ± 0.25 Ma (which is the age of Unit 2 below the unconformity as indicated by the nannofossil record and magnetostratigraphy results described in Section 2.3.2 above).

After the uplift event, the sediments of Unit 2 subsided to the original depth, i.e., ~ 550 mbsf, and the amount of subsidence is calculated as ~ 1050 m ($= \sim 500 + 550$ m) under the same assumption as that made for Model 1 (Figure 39). During this subsidence, the sediments of Unit 1 (~ 550 m thick) deposited on top of Unit 2. At this stage, the sediments of Unit 2 below the present-day unconformity were buried at the maximum depth range of 1000 ± 400 mbsf, as estimated using the approximate porosity-depth curve described above (Figure 39).

After the deposition of Unit 1, gently dipping normal faulting (which is likely to be related to the landslide and gravity collapse that occurred between Units 1 and 2) caused a normal displacement of a 450 ± 400 -m-depth interval (Figure 39). Considering the dip angle of the fault plane to be $\sim 10^\circ$ – 30° as was the case for Model 1, the thickness of the fault displacement would correspond to a distance of 2500 ± 2400 m parallel to the fault. This created the porosity gap across the present unconformity, and uplifted the sediments

of Unit 2 below the unconformity from their burial depth (1000 ± 400 mbsf). The age range of the sediments in Unit 1 above the unconformity, i.e., between 2.20 ± 0.25 Ma and 1.71 ± 0.24 Ma, is likely to coincide with the timing of the end of the uplift event and the start of the subsidence, deposition, and normal faulting.

The normal faulting is consistent with the normal fault stress regime observed from the structural analysis of the drilled cores [Harris *et al.*, 2013] (Figure 14). These normal faults are also supported by seismic reflection profiles in the Costa Rica wedge (Figure 4, 5, 11) where dense patterns of normal faults were observed in the slope and shelf above and below the unconformity based on multi-beam bathymetry, backscatter, and 3-D seismic data [Kluesner *et al.*, 2013; Bangs *et al.*, 2015]. The comparison with the structures indicated from 2D seismic profile BGR99-7 at Site 1380 is further discussed in Section 4.7 below.

The sediments below the unconformity preserves high paleo-temperature due to burial heating but may also have been subjected to high paleo-thermal gradient. Fluid flow that originated from a depth was probably initiated during the events of uplift, subsidence, and normal faulting, which most likely flowed along the weak planes of fault zones across the unconformity. Interaction with this high-temperature fluid caused both the precipitation of zeolites (laumontite, heulandite) and possibly a secondary consolidation of the sediments.

Through uplift, subsidence, and fault displacement, the sediments of Unit 2 originally at the depth of 450 ± 400 mbsf eventually reached the depth of ~ 550 mbsf at the current location (Figure 39).

4.5 Comparison with the upper slope Site 1379 and Site 1413

It is important to determine the burial, depositional and tectonic history and the possible marine landslides and sediment removal at this margin and to compare these between the upper and middle slopes, because an interesting question is whether the inferred uplift, mass movement, normal faulting, and high-temperature fluid-sediment interaction occurred locally or are widespread.

When comparing the P-wave velocity-porosity and the resistivity-porosity cross-correlation of the sediments recovered from the upper slope, the middle slope and the trench sites, it is notable that the relationship can be approximately fit with a similar curve, indicating that the consolidation trend does not vary significantly along the wedge slope (Figure 40). However, there are slight differences in the inclination of the porosity-depth curve between the upper slope and middle slope, which may reflect the differences in lithology such as the grain size and the clay/silt/sand content (Figure 41). The variation in lithology may also account for the different transects of the drilling location in Site 1413 from Site 1379 and Site 1380 (Section 2.3.4 above).

A comparison of the middle-slope Site 1380 and the upper-slope Site 1379 reveals that the porosity gap and the indicated amount of sediment removal is larger for the upper slope compared to the middle slope (Figure 41). The porosity gap observed at Site 1379 across the unconformity between Unit 3 consisting of fine-to-medium sandstone (~33%) and Unit 5 of medium to coarse sandstone and breccia (~17%) is ~16%, whereas the porosity gap at Site 1380 is ~10%. The unconformity observed at the upper slope exists at the greater depth ~900 mbsf compared to the middle-slope Site 1380. Here, similar beach deposits of shell-bearing sand layers (Unit 4) are distributed across the unconformity, indicating uplift to the nearshore environment.

If a consistent compaction trend is assumed and assuming that Unit 2 was deposited

when Unit 3 was at the seafloor and that the water depth ~ 130 m is constant, the geologic events that may have occurred across the unconformity can be considered using similar models based on the porosity gap, as was discussed for Site 1380. From the approximate porosity-depth curve, the maximum burial depth of the sediments below the unconformity is inferred to range between ~ 1500 and 1600 m.

When considering the maximum uplift and sediment removal (Model 1), the sediments at Site 1379 may have uplifted ~ 1630 – 1730 m ($=\sim 1500 + 130$ m, $\sim 1600 + 130$ m) to the ocean surface, allowing beach sediments to deposit and a material removal of ~ 1500 – 1600 m thickness to be eroded through gravity collapse; mass movement and normal faulting. If the dip angle of the slope is considered to be $\sim 10^\circ$ – 30° , the thickness of mass movement would correspond to the distance of ~ 3000 – 9200 m parallel to the slope. After these uplift and erosion events, the slope subsided ~ 1030 m ($=130 + 900$ m), depositing the current slope sediments on top (~ 900 m). These events occurred in the age range of ~ 0.61 m.y. (between 1.95 and 2.56 Ma). Through these events of uplift, material removal and subsidence, sediments below the unconformity may have experienced a net uplift of ~ 600 – 700 m.

In contrast, when considering minimum uplift/sediment removal and maximum normal fault displacement (Model 2), the sediments at Site 1379 may have uplifted ~ 730 – 830 m, depositing beach sediments on top, followed by subsidence of ~ 1030 m. The current slope sediments (~ 900 m) deposited later, burying the sediments below the current unconformity to the depth of ~ 1500 – 1600 mbsf. After burial, normal faulting probably caused displacement of ~ 600 – 700 m and exhumed the sediments to the current depth. Considering an approx. $\sim 10^\circ$ – 30° dip angle of the fault plane, the thickness of the fault displacement would correspond to the distance of ~ 1200 – 4000 m parallel to the fault.

These events would have occurred between 1.95 and 2.56 Ma, within the age range less than ~0.61 m.y.

These tectonic events consequently led to an overall uplift of ~600–700 m in Model 1 and an overall subsidence of ~200–300 m in Model 2 of the consolidated sediments below the unconformity. In Model 1, if the missing material of ~1500–1600 m was removed completely by a marine landslide and/or subaerial erosion, and both deposition and erosion occurred within 0.61 m.y., high sedimentation rates of more than ~2460 m/my at Site 1379 (=1500 m/0.61 m.y.) would be required, whereas in Model 2, the required sedimentation rate would be more than ~1150 m/my (=700/0.61 m.y.).

The amount of uplift of the seafloor reported from benthic foraminifera studies by *Vannucchi et al.* [2013] is ~800 m across the unconformity, which is close to the estimated events of Model 2. The amount of subsidence inferred by *Vannucchi et al.* [2013] is ~1200 m, which is also consistent with the estimates of ~1030 m in this study. Integrative studies of the paleo-water depths inferred from benthic foraminifera and the maximum burial conditions of the sediments inferred from this study are important to evaluate the recorded amounts of uplift and subsidence. The burial condition and the maximum burial depth range of the sediments below the unconformity examined in this study enables to assess the amount of surface erosion and/or fault displacement associated with these uplift and subsidence events.

The previous studies did not examine the zeolite compositions at the upper slope, and the presence of zeolites are not reported from the shipboard X-ray diffraction analysis measured during Expedition 334. The lateral variation in minerals between the middle and upper slopes revealed by the XRD measurements using samples from Site 1413 in the present study demonstrated that the major mineral components of the sediments at the

upper slope are phyllosilicates (including smectite and chlorite, plagioclase, quartz, and calcite), similar to the sediments at Site 1380 (Figure 42). However, zeolites are not present above ~40 mbsf in Unit 1 (silty clay with sand), but are present in Unit 2 (calcareous clayey siltstone and minor sandstone) and Unit 3 (fine-to-medium sandstone) consisting of mainly heulandite, with laumontite at the interval between 40- and 130 mbsf (Figure 42).

It is notable that analcime is not present in the samples from the drilled intervals at Site 1413, similar to the composition of Unit 1 at Site 1380. The zeolite distributions indicate that the temperature range at the upper-slope Site 1413 range from $86^{\circ}\pm 5^{\circ}\text{C}$ to $122^{\circ}\pm 2^{\circ}\text{C}$ below ~40 mbsf. Laumontite and heulandite probably formed due to an external source such as an interaction with high-temperature fluid, which may be related to the fluid flow observed along the unconformity at Site 1380. The consolidation state due to zeolite precipitation and fluid-sediment interaction is likely to be a common feature of the middle and upper slopes. It is notable that the inferred high-temperature fluid has flowed to shallower depth at the upper-slope Site 1413 compared to the middle-slope Site 1380.

The major seismic reflector across the unconformity is observed in both the lower and upper slopes, suggesting that the uplift, mass movement of sediments, subsidence and fault activity across the unconformity are regional rather than a local re-arranging of sediments. It is notable that the depth of the unconformity and the amount of uplift, material removal, subsidence, and fault displacement are larger in the upper slope compared to the middle slope, suggesting that the material flux during these events was variable along the overall wedge slope (Figure 41). The sediment removal and normal fault displacement across the unconformity may have had a significant impact on the

average wedge-scale taper angle and basal friction if they occurred in wide scale. The mass movement and normal faulting are likely to be regional, but it remains to be clarified where the removed sediments went and whether they reach the trench.

4.6 Major events at the wedge slope offshore Costa Rica inferred from this study and the relationship with the Cocos Ridge/seamount subduction

One of the major findings from this Expedition was that the consolidated upper plate material below the major unconformity at the Costa Rica margin was not composed of accreted oceanic lithologies (igneous rocks) or old accreted sediments as was anticipated before the Expedition (see Section 2.1.2 above). Instead, the upper plate material below the unconformity was revealed to be relatively new lithified terrigenous sediments. The comparably small age gap across the unconformity indicates that the rapid sedimentation and tectonic events occurred in the upper plate during a relatively short time frame at this margin.

I have examined the tectonic events in the upper plate of the Costa Rica margin involving uplift, material removal (erosion and mass movement), subsidence and normal faulting using two models (Model 1: maximum uplift and sediment removal, Model 2: maximum normal faulting).

At the middle-slope Site 1380, Model 1 predicts that the uplift event started at the time range between 2.20 ± 0.25 Ma and 1.71 ± 0.24 Ma, causing 1500 ± 400 m of maximum uplift and 1000 ± 400 m of maximum sediment removal via mass movement and normal faulting, within less than $\sim 0.48\text{--}0.97$ m.y (Figure 43). If the dip angle of the slope is considered to be $\sim 10^\circ\text{--}30^\circ$, this thickness of mass movement would correspond to the distance of 4600 ± 3400 m parallel to the slope. The events of uplift and material removal

probably modified the wedge geometry significantly from a high-taper wedge to a low-taper wedge, followed by subsidence of ~1050 m via fault displacement and/or basal erosion, starting at $< 2.20 \pm 0.25$ Ma $\sim 1.71 \pm 0.24$ Ma.

In contrast, Model 2 at Site 1380 predicts that the uplift event started around the time range between 2.20 ± 0.25 Ma and 1.71 ± 0.24 Ma, causing ~500 m of minimum uplift in less than ~0.48–0.97 m.y (Figure 43). This uplift event was followed by subsidence of ~1050 m and normal faulting that caused the maximum displacement of 450 ± 400 m, starting at $< 2.20 \pm 0.25$ Ma $\sim 1.71 \pm 0.24$ Ma. If the dip angle of the fault plane is considered to be $\sim 10^\circ$ – 30° , the thickness of the fault displacement would correspond to a distance of 2500 ± 2400 m parallel to the fault.

The start of uplift events at the time range between 2.20 ± 0.25 Ma to 1.71 ± 0.24 Ma in the upper plate inferred from both models is likely to be consistent with the timing of the arrival of the Cocos Ridge associated with multiple seamount chains offshore the Osa Peninsula, i.e., ~1–3 Ma, as reported from on-land chronological studies and recent modern plate reconstructions [e.g. *Morell*, 2015] (see Section 2.1.1 above). The geologic events in the slope of the upper plate inferred from the present study are likely to be related and thus due to the impact of the subduction of the Cocos Ridge and other associated seamounts. These seamounts are likely to have the height of ~1000–2500 m as currently observed, moving at the rate of ~90 mm/yr. The observed uplift event may have been caused by the topographic high of the Cocos Ridge and/or subsequent seamount chains that lifted the upper plate temporarily, followed by the gravitational collapse of the slope and normal faulting. The subsidence event observed in this study, in contrast, may have been due to basal erosion occurring at the asperity of the seamount along the plate boundary.

The age range 2.20 ± 0.25 Ma to 1.71 ± 0.24 Ma is also consistent with the uplift age (2.3-2 Ma) inferred from benthic foraminifera by *Vannucchi et al.* [2013] and the age range from nanofossils, i.e., 1.95–2.56 Ma across the unconformity [*Vannucchi et al.*, 2012] (Section 4.5 above). However, it is notable that these event ages for the upper slope may be slightly older than those for the middle slope in this study, which should be the opposite if the events were due to the same subducting seamount. The current distance between the upper and middle slopes is approx. 10 km, and if the seamount subducted at the rate of 90 mm/yr, the unconformity should be ~ 0.1 m.y. younger at the upper slope. Thus, the tectonic events in the middle slope may be due to a younger seamount, or the upper slope event could be explained by a slightly older seamount subduction such as the Quepos ridge ($\sim 2\text{--}3$ Ma).

These observations indicate that although the unconformity is continuous along the slope due to a sequential seamount arrival, the depth and age of the unconformity may be heterogeneous due to structural variations and individual events of multiple seamounts, as also discussed in Section 4.5 above in light of the porosity-depth transitions at the upper and middle slopes.

The events of uplift, material removal, subsidence and normal faulting inferred from both Models 1 and 2 probably modified the wedge geometry, causing significant deformation in the upper plate and abundant fluid flow along the fault zones (Figure 43). The amount of uplift and material removal are predicted to be larger by Model 1. The maximum and minimum conditions for these events to occur in Models 1 and 2 can be evaluated by considering the sediment thickness and required sedimentation rate and age range.

Here, the net sediment thickness with depth accounting for the porosity-depth

transition can be formulated as follows:

$$T_s = \int_{D_1}^{D_2} (1 - \phi) dD$$

where T_s is the sediment thickness, ϕ is the sediment porosity, and D_1 and D_2 are depth intervals.

The sedimentation rates can be recalculated from the net sediment thickness, and the estimation of the age of the sediments at the top of the missing material in Unit 2 can be accomplished if the sedimentation rate is known, assuming that the value is constant along the depth:

$$A_s = T_s \div R_s$$

where A_s is the sediment age and R_s is the sedimentation rate. From the recalculated sediment thickness of the NN 18 zone in Unit 2, i.e., ~122 m, the sedimentation rate of Unit 2, i.e., over ~600 m/m.y. (Section 2.3.2 above) would be greater than ~250 m/m.y.

In Model 1, the net sediment thickness of the missing material (1000±400 m) that has been removed is recalculated as ~280–770 m. My calculation of the net sediment thickness, age, and net sedimentation rate indicated that a sedimentation rate > 530±250 m/m.y. is necessary in order to deposit this amount of sediment within the age range 2.20±0.25 Ma to 1.71±0.24 Ma. In contrast, in Model 2, the net sediment thickness of the missing material (i.e., 450±400 m prior to uplift) is recalculated as 11–425 m, and a sedimentation rate > 220±210 m/m.y. is necessary in order to deposit this amount of sediment within the age range mentioned above.

The geologic events in Model 1 — maximum uplift and surface erosion — are more likely to occur under the condition of a high sedimentation rate for the missing zone of Unit 2 and extreme rapid uplift. Further investigations of the sedimentation rate and age

constraint are necessary to determine which model is more likely. However, the most essential insights derived from both models is that they predict an overall exhumation of 50–850 m of the deeply buried sediments despite the erosion, material removal and subsidence, indicating that these events during seamount subduction overall contributed to high consolidation of the forearc wedge.

4.7 Comparison of the structures from the 2D seismic profile BGR99-7 at Site 1380 and the 3D seismic reflection surveys

The erosional unconformity and mass transport deposit, slope sediment cover, faulting and folding interpreted from 2D seismic profiles (BGR99-7) at Site 1380 (Figures 11, 12) in Section 2.3.1 are consistent with the geologic history examined from the middle and upper slopes in the present study (Figures 11, 12). The events of uplift and subaerial erosion across the unconformity as characterized by Model 1 are supported by the seismically imaged erosional unconformity that cuts the landward-dipping reflectors in the margin wedge below (Figure 12, Stage 1). Above the unconformity, the characteristic zones where layer reflections are less defined indicate materials of incoherent fabric which may represent mass transport deposits (Figures 11, 12). The uplift events have likely induced landslide and mass movement, associated with normal fault and reverse fault displacement (Figure 12, Stage 2), which is consistent with the subaerial erosion and normal faulting as was depicted in Models 1 and 2. The slope sediments accompanied with mass transport materials deposited on top of the unconformity, possibly creating additional unconformity due to erosion (Figure 12, Stage 3). Similar zones of less defined reflection layers are also inferred in the shallower regions of the slope (Figure 11), indicating that multiple events of landslides have occurred at this horizon. Normal

faulting and landslides are not likely to have extended to the trench, but may have been divided into multiple events of mass movement. The events of uplift and erosion were associated with subsidence and the deposition of slope sediments.

The slope sediment deposition probably involved mass transport deposits, occasionally forming several unconformities in the shallower regions through erosion as observed from the seismic data (Figures 11, 12). The unconformities in the shallower region may be related with the recent uplift events inferred by *Vannucchi et al.* [2013] from benthic foraminifera at 1.9 Ma to now in the upper-slope Site 1379 (Section 2.2.2 above) and in the past 0.5 m.y. in the middle-slope Site 1378 drilled during Expedition 334.

The seamount subduction during the period 2.20 ± 0.25 Ma to 1.71 ± 0.24 Ma that caused most of the events described in this study is likely to have currently subducted beneath the Caribbean plate at the depth of 65–150 km, assuming the rate of subduction to be ~ 90 mm/m.y. and the distance from the trench where the slab steepens to be ~ 75 km [*Dinc et al.*, 2010; *Dzierma et al.*, 2010; 2011], although the actual seamount cannot be imaged at present at this depth due to the limited resolution at this range.

However, the 3D seismic transect reported by *Bangs et al.* [2015] has revealed a domed structure at ~ 6 km depth, indicating the features of the currently subducting seamount. Here, abundant thrust faults and folding characterizes the deeper structures in the upper plate below the unconformity, whereas normal faults are more concentrated in the slope above and below the unconformity [*Bangs et al.*, 2015]. These studies indicate that the events of uplift caused by seamount subduction are likely to have accompanied these various faulting, causing compression in the deeper margin and extension in the shallower range. The seaward-dipping thrust faults were observed to form along the

seaward side of the domed structure [Bangs *et al.*, 2015]. The domed structure is likely to be affecting the fault structures, where a change in fault orientation between landward- and seaward-dipping faults and fabrics was observed [Bangs *et al.*, 2015]. These changes in fault orientation may have occurred due to differences in stress conditions between the frontal and rear tracks of the seamount as the upper plate experienced the geologic events inferred in this study, i.e., uplift, subaerial erosion (gravity collapse), faulting, and subsidence during seamount subduction.

4.8 Characteristics of erosive wedge development affected by seamount subduction: –A high consolidation state and the effects during subduction erosion

The processes observed in the Costa Rica margin in this study provide insights into the characteristics of the development of an erosive wedge affected by seamount/ridge subduction (Figures 43, 44, 45). The events of uplift, subsidence, surface erosion, and normal faulting are likely to play major roles during subduction erosion.

During seamount/ridge subduction, a significant uplift occur mirroring the topography of the undergoing seamount, causing over-steepening of the wedge. The increase in the wedge taper leads to an unstably critical wedge, initiating gravity collapse through mass movement, submarine landslides, and normal faulting. These events of material removal are likely to decrease the wedge geometry if they are widespread. The upper plate is subjected to strong deformation and abundant fluid flow along weak paths such as fault zones. However, the sediment-fluid interaction causes mineral precipitation, and the uplift of sediments from deeper origins tends to preserve pore-filling materials produced under high temperatures, making the sediments more consolidated.

In light of these observations, the development of an erosive wedge is characterized

by a high consolidation state and high rock strength of the sediments due to uplift and an abundant sediment-fluid interaction, undergoing significant changes in wedge geometry during uplift, mass movement, and subsidence caused by seamount/ridge subduction (Figures 43, 44, 45). The amount of uplift inferred from this study, 1500 ± 400 m (maximum; Model 1) and ~ 500 m (minimum; Model 2) at Site 1380 may correspond to approx. $4^\circ\text{--}7^\circ$ and $\sim 2^\circ$ taper increases of the wedge if these events were widespread throughout the slope.

In contrast, the material removal indicated by this study, i.e., 1000 ± 400 m (Model 1, maximum mass movement) and 450 ± 400 m (Model 2, maximum fault displacement) may correspond approx. $2^\circ\text{--}5^\circ$ and $\sim 0.5^\circ\text{--}3^\circ$ taper reductions. These changes in the taper angle may be associated with the transition in wedge physical properties such as the basal friction coefficient and internal strength.

Despite the forearc subsidence and subduction erosion that are expected in erosive margins [von Huene and Scholl, 1991; Clift and Vannucchi, 2004], the present investigation of the balance among the tectonic events of uplift, sediment removal, normal faulting and subsidence revealed that these processes can result in either net uplift or net subsidence. However, the quantified material flux calculated in this study indicates that the deeply buried sediments were exhumed through erosion and extension. These erosive margins affected by rough topography are likely to be characterized by the high consolidation and large internal strength of the forearc wedge through exhumation effects.

4.9 The exhumation of consolidated sediments through surface erosion and faulting during seamount subduction and insights into seismogenic behaviors and fluid/heat flow

Figure 44 is a schematic drawing of upper plate deformation and the response predicted to occur during seamount/ridge subduction and the events that were quantified in this study offshore Costa Rica. Here, significant uplift is caused by the bathymetric highs on the subducting plate, followed by subsidence and extension along the post-collision decollement, and compression in the wake of the seamount. The upper plate is subjected to uplift, surface erosion and faulting, and it undergoes vast subsidence along the track of the seamount.

I have focused herein on the specific events during the uplift and subsidence, and I quantified the subsequent events and material flux using continuous physical property measurements and the maximum experienced burial conditions of the sediments. The sediments below the unconformity have likely uplifted to the ocean surface and reached the current depth through sediment removal (surface erosion) and fault displacement (Figures 44, 45). The forearc may uplift and exhume above the sea-level, creating significant surface erosion (Model 1). Alternatively, the forearc may be subjected to mainly normal fault displacement with minimum uplift and surface erosion (Model 2).

Through these processes, the uplift in the wake of the seamount causes a characteristic exhumation of consolidated sediments and higher paleo-isothermal distribution. The forearc wedge is characterized by a significant exhumation of deeper rocks through surface erosion (gravity collapse, mass movement) and extension (normal faulting) (Figure 45). The shallow isotherm at $\sim 100^{\circ}\text{--}150^{\circ}\text{C}$ observed in this study provides insights into the location of the up-dip limit of the seismogenic zone. Due to the erosional and extensional exhumation of deeply buried sediments, the high consolidation in the upper plate and the high geothermal gradient may consequently lift the seismogenic zone to a shallower depth range. This may explain the reason for the shallow ($\sim 6\text{-km}$ -

deep) earthquakes along the plate boundary abundantly observed during the 2002 Mw 6.4 Osa earthquake and its aftershocks that were characteristic in the Costa Rica margin, where the epicenter is located close to and below the CRISP drilling areas [Arroyo *et al.*, 2014].

In the Costa Rica margin, the 1999 Mw 6.9 Quepos earthquake occurred in the vicinity of a subducted seamount at ~10–30 km depth, indicating that the buried seamounts may also act as an asperity. Generally, various conceptual models and field observations have suggested that subducted seamounts/ridges act as asperities contributing to the nucleation of large earthquakes [Cloos, 1992; Scholz and Small, 1997; Yang *et al.*, 2012] and/or weak barriers that stop coseismic rupture propagation [e.g., Mochizuki *et al.*, 2008; Singh *et al.*, 2011]. Others have argued that seamounts behave predominantly aseismically, creating small to moderate size earthquakes, tremors, slow slips and creeps, due to pervasive fracturing and weakening in the upper plate [Wang and Bilek, 2014]. Although creeps and slow slips are reported along the Costa Rica margin and margins with rough topography subduction [Wang and Bilek, 2014], the question of whether the conditions of basal friction and the internal strength of the forearc wedge affected by high topography on the subducting plate are transitional with depth and the question of what controls these properties and fault slip behaviors are fundamental issues that require further investigation.

The upper plate of the Costa Rica margin is subjected to strong deformation and abundant fluid flow along weak paths such as fault zones. Seamounts and basement highs are thought to play important roles in hydrothermal states in the forearc wedge, because they may form high-permeability zones of recharge and/or discharge for fluid flow and may affect the fluid-thermal-circulation [Villinger *et al.*, 2002; Fisher *et al.*, 2003; Fisher

and Wheat, 2010; Fisher and Harris, 2010]. As seamounts subduct, hydrologic properties may vary due to deformation in the upper plate, producing fluid-rich fracture zones and abundant fluid seeps that are pervasively observed in the forearc wedge indicated by both clear low-velocity zones in seismic reflection studies and bathymetric features [*Sahling et al., 2008; Kluesner et al., 2013; Bangs et al., 2015*] and anomalously high heat flux in the trench and scatter in heat flux values throughout the wedge [*Harris et al., 2010ab; Spinelli et al., 2011*]. As observed in the present study, the sediment-fluid interaction causes mineral precipitation, and the exhumation of sediments from deeper origins tends to preserve the pore-filling materials produced under high temperature, making the sediments more consolidated. The high temperature fluids were probably heated due to deeper origin along faults and/or due to elevated isotherm during uplift.

5. Conclusion

In the present study, to quantify the deformation events during seamount subduction, I examined the consolidation process and physical property transitions of sediments across the major unconformity developed in the wedge slope of the Middle America Trench offshore Costa Rica, Osa Peninsula, where the aseismic Cocos Ridge and subsequent seamount chains subduct beneath the Caribbean Plate. The major unknowns of this margin investigated herein were the nature of the seismic reflectors and the major unconformity imaged from previous geophysical surveys, the lithology and consolidation state of the upper plate material beneath the unconformity, and their relationship of the geologic processes in the forearc wedge with seamount subduction.

On the basis of sediment microstructural observations, physical property measurements, and geochemical composition analyses using the sediment cores from the middle-slope Site 1380 recovered during IODP Expedition 344, I investigated the effects of burial diagenesis and fluid-sediment interactions on the porosity-depth transition to extract the initial burial compaction curve. I assessed the maximum burial conditions below the unconformity based on the porosity-depth curve and quantified the tectonic events of uplift, subsidence, surface erosion and fault displacement that have occurred across the unconformity as described below.

The upper plate material below the unconformity at the middle slope consisting of lithified terrigenous sediments of clayey siltstone (Units 2, 3) and the slope sediments above consisting of silty clay (Unit 1) were revealed to be characterized by consolidation due primarily to burial compaction and mineral precipitation of zeolites. A Na-type zeolite analcime which formed during burial diagenesis was observed to be present only below the unconformity, whereas a Na/Ca type zeolite heulandite and a Ca-type zeolite

laumontite were precipitated due to interaction with high-temperature fluid ($\sim 100^{\circ}\text{C}$) that has likely localized in the vicinity of the unconformity. The experienced maximum temperature of the sediments below the unconformity based on the formation of analcime during burial diagenesis is estimated to range from $86^{\circ}\pm 5^{\circ}\text{C}$ to $122^{\circ}\pm 2^{\circ}\text{C}$, which is higher than the current geothermal gradient. The change in zeolite assemblage indicates that the events of uplift from a greater depth, the transition of pressure-temperature (P-T) conditions, and sediment removal have occurred across the unconformity.

By quantifying the weight percentages of zeolites, I estimated the effect of laumontite and heulandite precipitation on porosity and recalculated the porosity-depth curve eliminating the effect of the fluid-sediment interaction. Based on microstructural observations, the lithology difference across the unconformity was minimal and the burial compaction trend was consistent among Units 1, 2 and 3, enabling to assume a composite initial porosity-depth curve of the sediments. The depth along the approximate curve of the porosity-depth transition of Unit 1 that matches the porosity of the sediments at the top of Unit 2 corresponds to the maximum burial depth range of the sediments below the unconformity: 1000 ± 400 meters below the seafloor (mbsf).

The distribution of the beach deposits consisting of shell fragments and the damage zones of normal fault regime across the unconformity were observed from the drilled cores, indicating that the sediments that have experienced the maximum burial depth range of 1000 ± 400 mbsf have likely uplifted to the ocean surface and reached the current depth through surface erosion and/or fault displacement.

In this study, the examination of the maximum sediment removal (surface erosion) (Model 1) and maximum fault displacement (Model 2) during uplift and subsidence events were made from the porosity gap across the unconformity and the burial

compaction curve derived from the porosity-depth relationship of the sediments. The results suggest that after the initial burial, the sediments uplifted ~ 500 m (Model 2) to 1500 ± 400 m (Model 1) to near sea level, followed by ~ 1050 m subsidence, associated with a mass movement of 1000 ± 400 m maximum (Model 1) and/or normal fault displacement of 450 ± 400 m maximum (Model 2) to reach the current depth range. Under an approx. 10° – 30° dip angle of the slope and fault plane, this thickness of maximum mass movement and normal faulting would correspond to the distances of 4600 ± 3400 m (Model 1) and 2500 ± 2400 m (Model 2) parallel to the slope and fault, respectively.

These events occurred during the time range between 2.20 ± 0.25 Ma and 1.71 ± 0.24 Ma inferred from nannofossil age, which is likely to be consistent with the timing of the onset of the subduction of the Cocos Ridge and the subsequent seamount chains reported by previous studies. The observations in this study suggest that the major unconformity in the wedge slope at the Costa Rica margin were developed through the geologic processes during Cocos Ridge/seamount subduction, in which significant uplift occurred mirroring the topography of the undergoing seamount, causing over-steepening of the wedge, followed by subsidence and erosion due to normal faulting, mass movement, and basal erosion.

The erosional unconformity, slope sediment cover, mass transport deposit, faulting and folding are indicated by 2D seismic reflection data near the middle-slope Site 1380, and they are consistent with the geologic events quantified from the sediment cores in this study. The events of uplift and subaerial erosion across the unconformity are supported by the seismically imaged erosional unconformity that cuts the landward-dipping reflectors in the margin wedge below. The uplift events have likely induced multiple events of landslide and mass movement, associated with normal fault and reverse

fault displacement. The slope sediments and mass transport materials deposited on top of the unconformity, possibly creating additional unconformity due to erosion in the shallower region. The major unconformity and the sedimentary layers were later folded, cut by and accompanied with abundant faults. The fluid paths that enable the significant sediment-fluid-thermal interaction in high temperature which caused zeolite precipitation promoting sediment consolidation revealed from this study may be related to the transitions in hydrologic properties during seamount subduction that initiated abundant fluid flow along the landward- and seaward-dipping high-amplitude reflectors that penetrate from greater depths and occasionally cut the unconformity.

The geologic events across the widespread unconformity observed in both the upper and middle slopes are likely to be regional. However, when comparing the major unconformity developed in the Costa Rica margin between the middle and upper slopes, the unconformity is shallower in the middle slope and the porosity gap and the indicated amount of sediment removal is larger in the upper slope. Although the unconformity is continuous along the slope due to sequential seamount arrival, the depth and age of the unconformity may be heterogeneous due to structural variations corresponding to multiple events of subsequent seamounts.

My investigation of the balance among tectonic events of uplift, sediment removal, normal faulting and subsidence during seamount subduction revealed that these processes resulted in a significant exhumation of deeper rocks to a shallower region through surface erosion (gravity collapse, mass movement) and/or extension (normal faulting), contributing to the high consolidation of the forearc wedge. The exhumation of the lithified, deeply buried sediments preserving the higher paleo-isotherm in the upper plate may thus have lifted the up-dip limit of the seismogenic zone to a shallower depth range.

The events of uplift, subsidence, surface erosion and normal faulting during seamount subduction are likely to play major roles in subduction erosion. The questions of whether the conditions of mechanical properties such as basal friction and the internal strength of the forearc wedge affected by high topography on the subducting plate are transitional with depth and what controls these properties and fault slip behaviors, remain to be addressed in future studies.

6. Acknowledgements

I express my profound gratitude to Professor Gaku Kimura for giving me the opportunity to study subduction zone geology. I am thankful for the numerous advice he has given me and the valuable discussions we went through during my doctoral, M.S. and undergraduate courses and theses. I am especially grateful to Professor Liz Screaton whom I met during the Costa Rica Seismogenesis Project (CRISP) for her constructive advice and discussions on physical properties and for allowing my visit to University of Florida and making my stay very fruitful. The critical and positive reviews and comments by Professor Hiroshi Sato, Professor Takashi Iidaka, Professor Naoshi Hirata, Dr. Ryosuke Ando, and Dr. Yasuhiro Yamada have greatly helped improve this thesis. I would like to acknowledge Dr. Shigenori Ogiwara for his constructive advice on zeolite XRD analysis and microstructural observation. I am grateful to Dr. Akihiro Kobayashi who has helped me conduct XRD measurements at the University of Tokyo. I am thankful to Dr. Koji Ichimura for his support on my SEM analysis on the thin sections. I express my gratitude to Dr. Hideto Yoshida for helping me with XRF measurements. I wish to thank Dr. Takashi Sakai who gave me advice upon making thin sections. I am very thankful to Dr. Satoshi Takahashi for giving me advice on geochemical analysis and helping me with XGT measurements. Mr. Yoshiaki Suzuki has given me a lot of advice on XRF analysis. Dr. Wataru Tanikawa has accepted me as JAMSTEC Research Student and allowed me to conduct physical property measurements (resistivity, P- and S-wave velocity, porosity) at Kochi Core Center (KCC), and gave me advice on physical properties. I would like to express my gratitude to Dr. Wataru Tanikawa, Dr. Weiren Lin, Dr. Takehiro Hirose, and Dr. Yohei Hamada in the Fault mechanics research group at KCC for accepting me to conduct physical property measurements. Dr. Osamu Tadai and Dr. Kentaro Hatakeda

have helped me greatly on the measurements and also taught me the background science at KCC. I am grateful to Mr. Takuya Matsuzaki, Ms. Shizu Yanagimoto, and Professor Masashi Murayama for accepting our use of the Center for Advanced Marine Core Research, Kochi University (CMCR) Nationwide Joint Use System for conducting research on the Nobeoka Thrust drill cores. I am grateful to Dr. Yoshitaka Hashimoto, Dr. Saneatsu Saito, and Dr. Kylara Martin whom I was lab groups with during CRISP for their research advice and encouragements. It was very exciting to measure physical properties of the drilled cores with them on the Joides Resolution. The discussions on sediment properties and core-log-seismic integration with them have always been very helpful. I wish to thank Dr. Arito Sakaguchi, Dr. Rob Harris, and Dr. Katerina Petronotis who were Co-Chief scientists and staff scientist during CRISP, for letting me participate in IODP Expedition 344 as a physical property specialist and for helping me greatly during and after the cruise. The discussions with Dr. Kohtaro Ujiie and Dr. Yuzuru Yamamoto on physical properties and microstructures of the Costa Rica and Nankai Trough sediments have been very helpful. I am thankful to Dr. Ken'ichi Ohkushi, for research discussion and for kindly hosting the CRISP domestic meetings at Kobe University, where I was able to discuss and exchange feedbacks on the Costa Rica research with the Expedition members in Japan. I am very thankful to Ms. Hitomi Uchimura whom I met during the Expedition, for her friendship and encouragements. I learned a lot from the discussions with Ms. Yuka Namiki and Dr. Akito Tsutsumi on frictional properties of ooze distributed near the trench and reference sites. The discussions on consolidation tests with Ms. Ayaka Saeki have been very helpful and exciting. I am very thankful to Dr. Xixi Zhao and Dr. Yong-Xiang (Frank) Li for their help in the lab during Expedition 344 and for hosting the post-cruise meeting in Shanghai

and the field excursion to Tibet in 2015 June-July. The discussions and fieldwork with Dr. Steffen Kutterolf and Ms. Julie Schindlbeck on tephra layers and chronology have been very helpful. I am thankful to Dr. Paola Vannucchi for her comments at science meetings. I would like to express my profound gratitude to Professor Robert Geller, Professor Satoshi Ide, Professor Kazuhito Ozawa, Dr. Yasutaka Ikeda, Dr. Hidemi Tanaka, Dr. Tsuyoshi Iizuka, Dr. Ichiko Shimizu, and Dr. Ataru Sakuraba for the numerous research discussions, seminars and classes, and for teaching me the geophysical and geochemical aspects of solid earth science. I am very thankful to Dr. Nathan Bangs for his research advice and discussions on seismic reflection data. I am grateful to Dr. Casey Moore for allowing my short visit to UC Santa Cruz in December 2013 and for the discussions on sediment distribution variety in subduction zones. I express my gratitude to Professor Tim Byrne and Professor Will Ouimet for accepting me to participate in the Taiwan Field Geology Course in January 2015, and giving me the chance to study the subduction zone geology in Taiwan. I would like to express my gratitude to Dr. David Okaya for giving me the opportunity to discuss and learn about synthetic modeling using acoustic logging data. I am very thankful to Ms. Stephanie James, Dr. John Ezell, Mr. Matt Farrell, Ms. Lanie Merideth, Ms. Karen Vyverberg, Ms. Jin Li, Ms. Michelle Penkrot, Ms. Xiaowen Zhang, Mr. Xingqian Cui, Ms. Alina Bricker, Dr. Amy Brown, Mr. Peter Chutcharavan, Ms. Alexandra Skrivanek, Dr. Kelly Deuerling, Ms. Andrea Portier, Ms. Iliya Smithka, Mr. Austin Sagul, Dr. Christian Stanciu, Ms. Megan Torpey, Dr. Amanda Waite, Mr. Paul Bremner, and everyone in the University of Florida Department of Geological Sciences for helping me during my stay in 2013 and 2014. I learned a lot from the marine geology class taught by Professor Ellen Martin and the geophysics class taught by Dr. Mark Panning at UF. I am grateful to Dr. Tania Villasenor and Dr. John Jaeger for giving me

advice on clay minerals and XRD analysis at UF. I am very thankful to Dr. Asuka Yamaguchi, Dr. Yujin Kitamura, and Dr. Jun Kameda for their advice and helpful discussions. I enjoyed the fieldworks in the Shimanto Belt, Nobeoka Thrust and Mino Belt, Gifu with them which has been a great opportunity for me to observe the structural geology of ancient accretionary prisms. I learned a lot from the field excursions at Boso and Miura Peninsula of the sedimentary rocks in young accretionary prism with Dr. Yuzuru Yamamoto and Ms. Nana Kamiya. I am thankful to Dr. Tatsu Kuwatani for allowing me to participate in the Joint Usage Program of ERI where I was able to learn data-driven science and modeling applied to geoscience. Rina Fukuchi, Mayuko Shimizu, Hiroaki Koge, Ryoji Kawasaki, and Takayoshi Otsuka were research group-mates who have always encouraged me, and I am very thankful for their valuable support and research discussions. I am thankful to Ms. Manami Kitamura, Mr. Masakazu Fujii, Mr. Kenji Kurosaki, Mr. Takeshi Akuhara, Ms. Sayako Inoue, Ms. Arisa Seki, and Ms. Kazue Suzuki for their encouragements and kind friendship. Mr. Yuan-min Tsai and Ms. Wendy Tsai have helped me a lot during the Taiwan Field Geology Course, and I am thankful for their friendship. Dr. Chastity Aiken, Mr. John Aiken, and Dr. Ray Chuang have inspired and encouraged me greatly and I am very grateful for their friendship and discussions. I wish to thank Dr. Keisuke Nishida, Dr. Daisuke Wakabayashi, Dr. Naofumi Aso, Mr. Suguru Yabe, Ms. Kumiko Matsui, Mr. Tomoaki Nishikawa, Mr. Masamichi Ara, and Mr. Junji Kikuchi for their support and encouragements. I am very thankful to Ms. Kyoko Tonegawa, Ms. Fumiko Fukuda, and Ms. Sumiko Kakizawa for their numerous support and for always making a good research environment. I am grateful to all the members of the Solid Earth Group and Earth and Planetary Science Department at University of Tokyo. I am thankful to my family for allowing me to enter the Ph.D. program and for

their numerous support and encouragements.

This work was supported by JSPS Grants-in-Aid for Scientific Research Fellowship for Young Scientists 02610283 (2014-2016), International Ocean Discovery Program (IODP) Post-cruise Research Fund (IODP Expedition 344) (2013-2016), Japan Agency for Marine-Earth Science and Technology (JAMSTEC) Research Student System (2014-2016), Tokyo Tech/Univ. Tokyo Global COE Program (GCOE) (2013), and Univ. Tokyo Ph.D. program research assistantship (2013).

7. References

- Abratis, M., and G. Wörner (2001), Ridge collision, slab-window formation, and the flux of Pacific asthenosphere into the Caribbean realm, *Geology*, 29(2), 127-130, doi: 10.1130/0091-7613(2001)029<0127:RCSWFA>2.0.CO;2.
- Adamek, S., F. Tajima, and D. A. Wiens (1987), Seismic rupture associated with subduction of the Cocos Ridge, *Tectonics*, 6(6), 757-774, DOI: 10.1029/TC006i006p00757.
- Arce, M. F., and D. I. Doser (2009), Relocation and waveform modeling of the 1924 Orotina, Costa Rica, earthquake (M S 7.0), *Tectonophysics*, 479(3), 197-202, doi:10.1016/j.tecto.2009.08.010.
- Archie, G. E. (1942), The electrical resistivity log as an aid in determining some reservoir characteristics, *Transactions of the AIME*, 146(01), 54-62, <http://dx.doi.org/10.2118/942054-G>.
- Arroyo, I. G., I. Grevemeyer, C. R. Ranero, and R. Von Huene (2014), Interplate seismicity at the CRISP drilling site: The 2002 Mw 6.4 Osa Earthquake at the southeastern end of the Middle America Trench, *Geochemistry, Geophysics, Geosystems*, 15(7), 3035-3050, DOI: 10.1002/2014GC005359.
- ASTM International (1990), Standard method for laboratory determination of water (moisture) content of soil and rock (Standard D2216-90), in *Annual Book of ASTM Standards for Soil and Rock*, vol. 04.08: Philadelphia (Am. Soc. Testing Mater.), [revision of D2216-63, D2216-80].
- Bangs, N. L., K. D. McIntosh, E. A. Silver, J. W. Kluesner, and C. R. Ranero (2015), Fluid accumulation along the Costa Rica subduction thrust and development of the seismogenic zone, *Journal of Geophysical Research: Solid Earth*, 120(1), 67-86,

DOI: 10.1002/2014JB011265.

Barckhausen, U., C. R. Ranero, R. v. Huene, S. C. Cande, and H. A. Roeser (2001), Revised tectonic boundaries in the Cocos Plate off Costa Rica: Implications for the segmentation of the convergent margin and for plate tectonic models, *Journal of Geophysical Research: Solid Earth*, 106(B9), 19207-19220,

DOI: 10.1029/2001JB000238.

Bassett, D., and A. B. Watts (2015), Gravity anomalies, crustal structure, and seismicity at subduction zones: 1. Seafloor roughness and subducting relief, *Geochemistry, Geophysics, Geosystems*, 16(5), 1508-1540, DOI: 10.1002/2014GC005684.

Bekins, B., A. M. McCaffrey, and S. J. Dreiss (1994), Influence of kinetics on the smectite to illite transition in the Barbados accretionary prism, *Journal of Geophysical Research: Solid Earth*, 99(B9), 18147-18158, DOI: 10.1029/94JB01187.

Bilek, S. L., S. Y. Schwartz, and H. R. DeShon (2003), Control of seafloor roughness on earthquake rupture behavior, *Geology*, 31(5), 455-458, doi: 10.1130/0091-7613(2003)031<0455:COSROE>2.0.CO;2.

Blum, P. (1997), Physical properties handbook: a guide to the shipboard measurement of physical properties of deep-sea cores, *ODP Tech. Note*, 26, <http://www-odp.tamu.edu/publications/tnotes/tn26/INDEX.HTM>.

Bray, C., and D. Karig (1985), Porosity of sediments in accretionary prisms and some implications for dewatering processes, *Journal of Geophysical Research: Solid Earth*, 90(B1), 768-778, DOI: 10.1029/JB090iB01p00768.

Bullard, E. (1939), Heat flow in South Africa, *Proceedings of the Royal Society of London. Series A, Mathematical and Physical Sciences*, 474-502, <http://www.jstor.org/stable/97404>.

- Clift, P., and P. Vannucchi (2004), Controls on tectonic accretion versus erosion in subduction zones: Implications for the origin and recycling of the continental crust, *Reviews of Geophysics*, 42(2), RG2001, DOI: 10.1029/2003RG000127.
- Cloos, M. (1992), Thrust-type subduction-zone earthquakes and seamount asperities: A physical model for seismic rupture, *Geology*, 20(7), 601-604, doi: 10.1130/0091-7613(1992)020<0601:TTSZEA>2.3.CO;2.
- Collins, L. S., A. G. Coates, J. B. Jackson, and J. A. Obando (1995), Timing and rates of emergence of the Limón and Bocas del Toro basins: Caribbean effects of Cocos Ridge subduction?, *Geological Society of America Special Papers*, 295, 263-290, doi: 10.1130/SPE295-p263.
- Coombs, D., A. Ellis, W. Fyfe, and A. Taylor (1959), The zeolite facies, with comments on the interpretation of hydrothermal syntheses, *Geochimica et cosmochimica acta*, 17(1-2), 53-107, doi:10.1016/0016-7037(59)90079-1.
- Corrigan, J., P. Mann, and J. C. INGLE (1990), Forearc response to subduction of the Cocos Ridge, Panama-Costa Rica, *Geological Society of America Bulletin*, 102(5), 628-652, doi: 10.1130/0016-7606(1990)102<0628:FRTSOT>2.3.CO;2.
- Daigle, H., and E. Sreaton (2015), Evolution of sediment permeability during burial and subduction, *Geofluids*, 15(1-2), 84-105, DOI: 10.1111/gfl.12090.
- de Boer, J. Z., M. S. Drummond, M. J. Bordelon, M. J. Defant, H. Bellon, and R. C. Maury (1995), Cenozoic magmatic phases of the Costa Rican island arc (Cordillera de Talamanca), *Geological Society of America Special Papers*, 295, 35-56, doi: 10.1130/SPE295-p35.
- DeMets, C. (2001), A new estimate for present - day Cocos - Caribbean plate motion: Implications for slip along the Central American volcanic arc, *Geophysical Research*

Letters, 28(21), 4043-4046, DOI: 10.1029/2001GL013518.

DeShon, H. R., S. Y. Schwartz, S. L. Bilek, L. Dorman, V. Gonzalez, J. Protti, E. R. Flueh, and T. H. Dixon (2003), Seismogenic zone structure of the southern Middle America trench, Costa Rica, *Journal of Geophysical Research: Solid Earth*, 108(B10), 2491, DOI: 10.1029/2002JB002294.

Dinc, A. N., I. Koulakov, M. Thorwart, W. Rabbel, E. R. Flueh, I. Arroyo, W. Taylor, and G. Alvarado (2010), Local earthquake tomography of central Costa Rica: transition from seamount to ridge subduction, *Geophysical Journal International*, 183(1), 286-302, doi: 10.1111/j.1365-246X.2010.04717.x.

Dominguez, S., S. Lallemand, J. Malavieille, and R. von Huene (1998), Upper plate deformation associated with seamount subduction, *Tectonophysics*, 293(3), 207-224, doi:10.1016/S0040-1951(98)00086-9.

Dzierma, Y., M. M. Thorwart, W. Rabbel, E. R. Flueh, G. Alvarado, and M. Mora (2010), Imaging crustal structure in south central Costa Rica with receiver functions, *Geochemistry, Geophysics, Geosystems*, 11(8), Q08526, DOI: 10.1029/2009GC002936.

Dzierma, Y., W. Rabbel, M. M. Thorwart, E. R. Flueh, M. Mora, and G. Alvarado (2011), The steeply subducting edge of the Cocos Ridge: Evidence from receiver functions beneath the northern Talamanca Range, south - central Costa Rica, *Geochemistry, Geophysics, Geosystems*, 12(4), Q04530, DOI: 10.1029/2010GC003477.

Erickson, S. N., and R. D. Jarrard (1998), Velocity - porosity relationships for water - saturated siliciclastic sediments, *Journal of Geophysical Research: Solid Earth*, 103(B12), 30385-30406, DOI: 10.1029/98JB02128.

Ewing, R., and A. Hunt (2006), Dependence of the electrical conductivity on saturation

- in real porous media, *Vadose Zone Journal*, 5(2), 731-741, doi:10.2136/vzj2005.0107.
- Expedition 315 Scientists, (2009), Expedition 315 Site C0002, In Kinoshita, M., Tobin, H., Ashi, J., Kimura, G., Lallemand, S., Sreaton, E.J., Curewitz, D., Masago, H., Moe, K.T., and the Expedition 314/315/316 Scientists, *Proc. IODP*, 314/315/316: Washington, DC (Integrated Ocean Drilling Program Management International, Inc.). doi:10.2204/iodp.proc.314315316.124.2009
- Fisher, A., E. Davis, M. Hutnak, V. Spiess, L. Zühlendorff, A. Cherkaoui, L. Christiansen, K. Edwards, R. Macdonald, and H. Villinger (2003), Hydrothermal recharge and discharge across 50 km guided by seamounts on a young ridge flank, *Nature*, 421(6923), 618-621, doi:10.1038/nature01352.
- Fisher, A. T., and R. N. Harris (2010), Using seafloor heat flow as a tracer to map subsurface fluid flow in the ocean crust, *Geofluids*, 10(1 - 2), 142-160, DOI: 10.1111/j.1468-8123.2009.00274.x.
- Fisher, A. T., and C. G. Wheat (2010), Seamounts as conduits for massive fluid, heat, and solute fluxes on ridge flanks, *Oceanography*, 23(1), 74-87, <http://dx.doi.org/10.5670/oceanog.2010.63>.
- Fisher, D. M., T. W. Gardner, P. B. Sak, J. D. Sanchez, K. Murphy, and P. Vannucchi (2004), Active thrusting in the inner forearc of an erosive convergent margin, Pacific coast, Costa Rica, *Tectonics*, 23(2), TC2007, DOI: 10.1029/2002TC001464.
- Güendel, F., K. McNally, J. Lower, M. Protti, R. Saenz, E. Malavassi, J. Barquero, R. Van der Laat, V. González, and C. Montero (1989), First results from a new seismographic network in Costa Rica, Central America, *Bulletin of the Seismological Society of America*, 79(1), 205-210.

- Gardner, T. W., D. Verdonck, N. M. Pinter, R. Slingerland, K. P. Furlong, T. F. Bullard, and S. G. Wells (1992), Quaternary uplift astride the aseismic Cocos ridge, Pacific coast, Costa Rica, *Geological Society of America Bulletin*, 104(2), 219-232, doi: 10.1130/0016-7606(1992)104<0219:QUATAC>2.3.CO;2.
- Gardner, T. W., D. M. Fisher, K. D. Morell, and M. L. Cupper (2013), Upper-plate deformation in response to flat slab subduction inboard of the aseismic Cocos Ridge, Osa Peninsula, Costa Rica, *Lithosphere*, 5(3), 247-264, doi:10.1130/L251.1.
- Geist, E. L., M. A. Fisher, and D. W. Scholl (1993), Large-scale deformation associated with ridge subduction, *Geophysical Journal International*, 115(2), 344-366, doi: 10.1111/j.1365-246X.1993.tb01191.x.
- Goes, S., A. Velasco, S. Schwartz, and T. Lay (1993), The April 22, 1991, Valle de la Estrella, Costa Rica (Mw= 7.7) earthquake and its tectonic implications- A broadband seismic study, *Journal of geophysical research*, 98, 8127-8142, DOI: 10.1029/93JB00019.
- Gräfe, K., W. Frisch, I. Villa, and M. Meschede (2002), Geodynamic evolution of southern Costa Rica related to low-angle subduction of the Cocos Ridge: constraints from thermochronology, *Tectonophysics*, 348(4), 187-204, doi:10.1016/S0040-1951(02)00113-0.
- Hamahashi, M., S. Saito, G. Kimura, A. Yamaguchi, R. Fukuchi, J. Kameda, Y. Hamada, Y. Kitamura, K. Fujimoto, and Y. Hashimoto (2013), Contrasts in physical properties between the hanging wall and footwall of an exhumed seismogenic megasplay fault in a subduction zone—an example from the Nobeoka Thrust Drilling Project, *Geochemistry, Geophysics, Geosystems*, 14(12), 5354-5370, DOI: 10.1002/2013GC004818.

- Hamahashi, M., Y. Hamada, A. Yamaguchi, G. Kimura, R. Fukuchi, S. Saito, J. Kameda, Y. Kitamura, K. Fujimoto, and Y. Hashimoto (2015), Multiple damage zone structure of an exhumed seismogenic megasplay fault in a subduction zone—a study from the Nobeoka Thrust Drilling Project, *Earth, Planets and Space*, 67(1), 1-21, doi:10.1186/s40623-015-0186-2.
- Harris, R. N., I. Grevemeyer, C. R. Ranero, H. Villinger, U. Barckhausen, T. Henke, C. Mueller, and S. Neben (2010a), Thermal regime of the Costa Rican convergent margin: 1. Along - strike variations in heat flow from probe measurements and estimated from bottom - simulating reflectors, *Geochemistry, Geophysics, Geosystems*, 11(12), Q12S28, DOI: 10.1029/2010GC003272.
- Harris, R. N., G. Spinelli, C. R. Ranero, I. Grevemeyer, H. Villinger, and U. Barckhausen (2010b), Thermal regime of the Costa Rican convergent margin: 2. Thermal models of the shallow Middle America subduction zone offshore Costa Rica, *Geochemistry, Geophysics, Geosystems*, 11(12), Q0AD16, DOI: 10.1029/2010GC003273.
- Harris, R., A. Sakaguchi, K. Petronotis, and the Expedition 344 Scientists (2013), *Proceedings of the Integrated Ocean Drilling Program*, 344: College Station, TX (Integrated Ocean Drilling Program), doi:10.2204/iodp.proc.344.2013.
- Hauff, F., K. Hoernle, H.-U. Schmincke, and R. Werner (1997), A Mid Cretaceous origin for the Galapagos hotspot: Volcanological, petrological and geochemical evidence from Costa Rican oceanic crustal segments, *Geologische Rundschau*, 86(1), 141-155, DOI: 10.1007/PL00009938.
- Hauff, F., K. Hoernle, G. Tilton, D. Graham, and A. C. Kerr (2000), Large volume recycling of oceanic lithosphere over short time scales: geochemical constraints from the Caribbean Large Igneous Province, *Earth and Planetary Science Letters*,

174(3), 247-263, doi:10.1016/S0012-821X(99)00272-1.

Hoernle, K., P. van den Bogaard, R. Werner, B. Lissinna, F. Hauff, G. Alvarado, and D. Garbe-Schönberg (2002), Missing history (16–71 Ma) of the Galápagos hotspot: Implications for the tectonic and biological evolution of the Americas, *Geology*, 30(9), 795-798, doi: 10.1130/0091-7613(2002)030<0795:MHMOTG>2.0.CO;2.

Hoffman, N. W. and H. J. Tobin (2004), An Empirical relationship between velocity and porosity for underthrust sediments in the Nankai Trough accretionary prism, in Mikada, H., G. Moore, A. Taira, K. Becker, J. Moore, and A. Klaus (Eds), *Proceedings of the Ocean Drilling Program, Scientific Results*, 190/196, 1-23, <http://www-odp.tamu.edu/publications/190196SR/VOLUME/CHAPTERS/355>.
PDF.

Husen, S., E. Kissling, and R. Quintero (2002), Tomographic evidence for a subducted seamount beneath the Gulf of Nicoya, Costa Rica: The cause of the 1990 Mw= 7.0 Gulf of Nicoya earthquake, *Geophysical Research Letters*, 29(8), 79-1 – 79-4, DOI: 10.1029/2001GL014045.

Husen, S., R. Quintero, E. Kissling, and B. Hacker (2003), Subduction-zone structure and magmatic processes beneath Costa Rica constrained by local earthquake tomography and petrological modelling, *Geophysical Journal International*, 155(1), 11-32, doi: 10.1046/j.1365-246X.2003.01984.x.

Iijima, A., and M. Utada (1972), A critical review on the occurrence of zeolites in sedimentary rocks in Japan, *Jpn Geol Geogr*, 42, 61-84.

Iijima, A. (1986), Occurrence of natural zeolites, *Journal of the Clay Science Society of Japan*, 26(2), 90-103, <http://doi.org/10.11362/jcssjndokagaku1961.26.90>.

Johnson, G., and A. Lowrie (1972), Cocos and Carnegie Ridges result of the Galapagos

“hot spot”?, *Earth and Planetary Science Letters*, 14(2), 279-280, doi:10.1016/0012-821X(72)90020-9.

Kluesner, J. W., E. A. Silver, N. L. Bangs, K. D. McIntosh, J. Gibson, D. Orange, C. R. Ranero, and R. Huene (2013), High density of structurally controlled, shallow to deep water fluid seep indicators imaged offshore Costa Rica, *Geochemistry, Geophysics, Geosystems*, 14(3), 519-539, DOI: 10.1002/ggge.20058.

Kobayashi, D., P. LaFemina, H. Geirsson, E. Chichaco, A. A. Abrego, H. Mora, and E. Camacho (2014), Kinematics of the western Caribbean: Collision of the Cocos Ridge and upper plate deformation, *Geochemistry, Geophysics, Geosystems*, 15(5), 1671-1683, DOI: 10.1002/2014GC005234.

Kolarsky, R. A., and P. Mann (1995), Structure and neotectonics of an oblique-subduction margin, southwestern Panama, *Geological Society of America Special Papers*, 295, 131-158, doi: 10.1130/SPE295-p131.

Kozlov, B., M. Schneider, B. Montaron, M. Lagues, and P. Tabeling (2012), Archie's law in microsystems, *Transport in porous media*, 95(1), 1-20, DOI: 10.1007/s11242-012-0029-6.

LaFemina, P., T. H. Dixon, R. Govers, E. Norabuena, H. Turner, A. Saballos, G. Mattioli, M. Protti, and W. Strauch (2009), Fore - arc motion and Cocos Ridge collision in Central America, *Geochemistry, Geophysics, Geosystems*, 10(5), Q05S14, DOI: 10.1029/2008GC002181.

Linkimer, L., S. L. Beck, S. Y. Schwartz, G. Zandt, and V. Levin (2010), Nature of crustal terranes and the Moho in northern Costa Rica from receiver function analysis, *Geochemistry, Geophysics, Geosystems*, 11(1), Q01519, DOI: 10.1029/2009GC002795.

- Lonsdale, P., and K. D. Klitgord (1978), Structure and tectonic history of the eastern Panama Basin, *Geological Society of America Bulletin*, 89(7), 981-999, doi: 10.1130/0016-7606(1978)89<981:SATHOT>2.0.CO;2.
- Lonsdale, P. (2005), Creation of the Cocos and Nazca plates by fission of the Farallon plate, *Tectonophysics*, 404(3), 237-264, doi:10.1016/j.tecto.2005.05.011.
- MacMillan, I., P. B. Gans, and G. Alvarado (2004), Middle Miocene to present plate tectonic history of the southern Central American Volcanic Arc, *Tectonophysics*, 392(1), 325-348, doi:10.1016/j.tecto.2004.04.014.
- McCann, W. R., and R. E. Habermann (1989), Morphologic and geologic effects of the subduction of bathymetric highs, in *Subduction Zones Part II*, edited, pp. 41-69, Springer, DOI: 10.1007/978-3-0348-9140-0_4.
- Mochizuki, K., T. Yamada, M. Shinohara, Y. Yamanaka, and T. Kanazawa (2008), Weak interplate coupling by seamounts and repeating $M \sim 7$ earthquakes, *Science*, 321(5893), 1194-1197, DOI: 10.1126/science.1160250.
- Montaron, B. (2009), Connectivity theory—a new approach to modeling non-Archie rocks, *Petrophysics*, 50(02), 102-115, SPWLA-2009-v50n2a2.
- Morell, K. D., E. Kirby, D. M. Fisher, and M. Soest (2012), Geomorphic and exhumational response of the Central American Volcanic Arc to Cocos Ridge subduction, *Journal of Geophysical Research: Solid Earth*, 117(B4), B04409, DOI: 10.1029/2011JB008969.
- Morell, K. D. (2015), Late Miocene to recent plate tectonic history of the southern Central America convergent margin, *Geochemistry, Geophysics, Geosystems*, 16(10), 3362-3382, DOI: 10.1002/2015GC005971.
- Nishimura, T., A. Iijima, and M. Utada (1980), Zeolitic burial diagenesis and basin

- analysis of the Izumi Group in Shikoku and Awaji Islands, Southwest Japan, *The Journal of the Geological Society of Japan*, 86(5), 341-351.
- Ogiwara, N. (1996), The mechanism of transformation of clinoptilolite to analcime or heulandite during burial diagenesis, *Journal of Clay Science Society of Japan*, 36(2), 73-85, <http://doi.org/10.11362/jcssjnendokagaku1961.36.73>.
- Perry, E. A. (1970), Burial diagenesis in Gulf Coast pelitic sediments, *Clays and Clay Minerals*, 18, 165-177, DOI: 10.1346/CCMN.1970.0180306.
- Protti, M., F. Gu, and K. McNally (1994), The geometry of the Wadati-Benioff zone under southern Central America and its tectonic significance: results from a high-resolution local seismographic network, *Physics of the Earth and Planetary Interiors*, 84(1-4), 271-287, doi:10.1016/0031-9201(94)90046-9.
- Protti, M., F. Giendel, and K. McNally (1995), Correlation between the age of the subducting Cocos plate and the geometry of the Wadati-Benioff zone under Nicaragua and Costa Rica, *Geological Society of America Special Papers*, 295, 309-326, doi: 10.1130/SPE295-p309.
- Ranero, C. R., and R. von Huene (2000), Subduction erosion along the Middle America convergent margin, *Nature*, 404(6779), 748-752, doi:10.1038/35008046.
- Ranero, C. R., I. Grevemeyer, H. Sahling, U. Barckhausen, C. Hensen, K. Wallmann, W. Weinrebe, P. Vannucchi, R. Von Huene, and K. McIntosh (2008), Hydrogeological system of erosional convergent margins and its influence on tectonics and interplate seismogenesis, *Geochemistry, Geophysics, Geosystems*, 9(3), Q03S04, DOI: 10.1029/2007GC001679.
- Rosenbaum, G., and W. Mo (2011), Tectonic and magmatic responses to the subduction of high bathymetric relief, *Gondwana Research*, 19(3), 571-582,

doi:10.1016/j.gr.2010.10.007.

- Sahling, H., D. G. Masson, C. R. Ranero, V. Hühnerbach, W. Weinrebe, I. Klaucke, D. Bürk, W. Brückmann, and E. Suess (2008), Fluid seepage at the continental margin offshore Costa Rica and southern Nicaragua, *Geochemistry, Geophysics, Geosystems*, 9(5), Q05S05, DOI: 10.1029/2008GC001978.
- Sak, P. B., D. M. Fisher, and T. W. Gardner (2004), Effects of subducting seafloor roughness on upper plate vertical tectonism: Osa Peninsula, Costa Rica, *Tectonics*, 23(1), TC1017, DOI: 10.1029/2002TC001474.
- Sakaguchi, A. and J. Yamashita (2015), Thermal dependent displacement and recurrent intervals of subduction large earthquakes in case of the Costa Rica seismogenic zone, presented at *The Geological Society of Japan 122th Annual Meeting*, Nagano, 11-13 September 2015, Abstract: R13-O-4.
- Scholz, C. H., and C. Small (1997), The effect of seamount subduction on seismic coupling, *Geology*, 25(6), 487-490, doi: 10.1130/0091-7613(1997)025<0487:TEOSSO>2.3.CO;2.
- Shipboard Scientific Party (1980), Sites 438 and 439: Japan Deep Sea Terrace, Leg 57, *In* von Huene, R., Nasu, N., Arthur, M.A., Barron, J.A., Bell, G.D., Cadet, J.P., Carson, B., Fujioka, K., Honza, E., Keller, G., Moore, G.W., Reynolds, R., Sato, S., and Shaffer, B.L., *Deep Sea Drilling Project Initial Reports Volume 56 & 57*, 23-191, doi:10.2973/dsdp.proc.5657.102.1980.
- Shipboard Scientific Party (2002), Site 808, *In* Mikada, H., Becker, K., Moore, J.C., Klaus, A., et al., *Proc. ODP, Init. Repts.*, 196: College Station, TX (Ocean Drilling Program), 1–68. doi:10.2973/odp.proc.ir.196.104.2002.
- Singh, S. C., N. Hananto, M. Mukti, D. P. Robinson, S. Das, A. Chauhan, H. Carton, B.

- Gratacos, S. Midnet, and Y. Djajadihardja (2011), Aseismic zone and earthquake segmentation associated with a deep subducted seamount in Sumatra, *Nature Geoscience*, 4(5), 308-311, doi:10.1038/ngeo1119.
- Sinton, C. W., R. A. Duncan, and P. Denyer (1997), Nicoya Peninsula, Costa Rica: A single suite of Caribbean oceanic plateau magmas, *Journal of Geophysical Research*, 102(B7), 15507-15520, DOI: 10.1029/97JB00681.
- Sitchler, J. C., D. M. Fisher, T. W. Gardner, and M. Protti (2007), Constraints on inner forearc deformation from balanced cross sections, Fila Costeña thrust belt, Costa Rica, *Tectonics*, 26(6), TC6012, DOI: 10.1029/2006TC001949.
- Spinelli, G., and R. Harris (2011), Thermal effects of hydrothermal circulation and seamount subduction: Temperatures in the Nankai Trough Seismogenic Zone Experiment transect, Japan, *Geochemistry, Geophysics, Geosystems*, 12(12), Q0AD21, DOI: 10.1029/2011GC003727.
- Stavenhagen, A., E. Flueh, C. Ranero, K. McIntosh, T. Shipley, G. Leandro, A. Schulze, and J. Danobeitia (1998), Seismic wide-angle investigations in Costa Rica: A crustal velocity model from the Pacific to the Caribbean coast, *Z. Geol. Palaontol*, 1(3-6), 393-406.
- Syracuse, E. M., G. A. Abers, K. Fischer, L. MacKenzie, C. Rychert, M. Protti, V. González, and W. Strauch (2008), Seismic tomography and earthquake locations in the Nicaraguan and Costa Rican upper mantle, *Geochemistry, Geophysics, Geosystems*, 9(7), Q07508, DOI: 10.1029/2008GC001963.
- Torres, M. E., J. M. Muratli, and E. A. Solomon (2014), Data report: minor element concentrations in pore fluids from the CRISP-A transect drilled during Expedition 334, in Vannucchi, P., K. Ujiie, N. Stroncik, and A. Malinverno the Expedition 334

- Scientists (2012), *Proceedings of the Integrated Ocean Drilling Program*, 334: Tokyo (Integrated Ocean Drilling Program Management International, Inc.), doi:10.2204/iodp.proc.334.201.2014.
- Vacquier, V. (1985), The measurement of thermal conductivity of solids with a transient linear heat source on the plane surface of a poorly conducting body, *Earth and planetary science letters*, 74(2), 275-279, doi:10.1016/0012-821X(85)90027-5.
- Vannucchi, P., D. M. Fisher, S. Bier, and T. W. Gardner (2006), From seamount accretion to tectonic erosion: Formation of Osa Mélangé and the effects of Cocos Ridge subduction in southern Costa Rica, *Tectonics*, 25(2), TC2004, DOI: 10.1029/2005TC001855.
- Vannucchi, P., K. Ujiie, N. Stroncik, A. Malinverno, and the Expedition 334 Scientists (2012), *Proceedings of the Integrated Ocean Drilling Program*, 334: Tokyo (Integrated Ocean Drilling Program Management International, Inc.), doi:10.2204/iodp.proc.334.2012.
- Vannucchi, P., P. B. Sak, J. P. Morgan, K. i. Ohkushi, and K. Ujiie (2013), Rapid pulses of uplift, subsidence, and subduction erosion offshore Central America: Implications for building the rock record of convergent margins, *Geology*, 41(9), 995-998, doi:10.1130/G34355.1.
- Villinger, H., I. Grevemeyer, N. Kaul, J. Hauschild, and M. Pfender (2002), Hydrothermal heat flux through aged oceanic crust: where does the heat escape?, *Earth and Planetary Science Letters*, 202(1), 159-170, doi:10.1016/S0012-821X(02)00759-8.
- Vogt, P. (1973), Subduction and aseismic ridges, *Nature*, 241, 189-191, doi:10.1038/241189a0.
- von Huene, R., and S. Lallemand (1990), Tectonic erosion along the Japan and Peru

- convergent margins, *Geological Society of America Bulletin*, 102(6), 704-720, doi: 10.1130/0016-7606(1990)102<0704:TEATJA>2.3.CO;2.
- von Huene, R., and D. W. Scholl (1991), Observations at convergent margins concerning sediment subduction, subduction erosion, and the growth of continental crust, *Reviews of Geophysics*, 29(3), 279-316, DOI: 10.1029/91RG00969.
- von Huene, R., J. Bialas, E. Flueh, B. Cropp, T. Csernok, E. Fabel, J. Hoffmann, K. Emeis, P. Holler, and G. Jeschke (1995), Morphotectonics of the Pacific convergent margin of Costa Rica, in *Geologic and tectonic development of the Caribbean Plate boundary in southern Central America*, 295, 291.
- von Huene, R., C. R. Ranero, W. Weinrebe, and K. Hinz (2000), Quaternary convergent margin tectonics of Costa Rica, segmentation of the Cocos Plate, and Central American volcanism, *Tectonics*, 19(2), 314-334, DOI: 10.1029/1999TC001143.
- Walther, C. H. (2003), The crustal structure of the Cocos ridge off Costa Rica, *Journal of Geophysical Research: Solid Earth*, 108(B3), 2136, DOI: 10.1029/2001JB000888.
- Wang, K., and S. L. Bilek (2014), Invited review paper: Fault creep caused by subduction of rough seafloor relief, *Tectonophysics*, 610, 1-24, doi:10.1016/j.tecto.2013.11.024.
- Wegner, W., G. Wörner, R. S. Harmon, and B. R. Jicha (2011), Magmatic history and evolution of the Central American Land Bridge in Panama since Cretaceous times, *Geological Society of America Bulletin*, 123(3-4), 703-724, doi:10.1130/B30109.1.
- Werner, R., K. Hoernle, U. Barckhausen, and F. Hauff (2003), Geodynamic evolution of the Galápagos hot spot system (Central East Pacific) over the past 20 my: Constraints from morphology, geochemistry, and magnetic anomalies, *Geochemistry, Geophysics, Geosystems*, 4(12), 1108, DOI: 10.1029/2003GC000576.
- Yang, H., Y. Liu, and J. Lin (2012), Effects of subducted seamounts on megathrust

earthquake nucleation and rupture propagation, *Geophysical Research Letters*, 39, L24302, DOI: 10.1029/2012GL053892.

Yoshimura, N. (1994), Evaluation of thermal history of sedimentary basin from a mineralogical point of view, *The Japanese Association for Petroleum Technology*, 59(4), 271-278, <http://doi.org/10.3720/japt.59.271>.

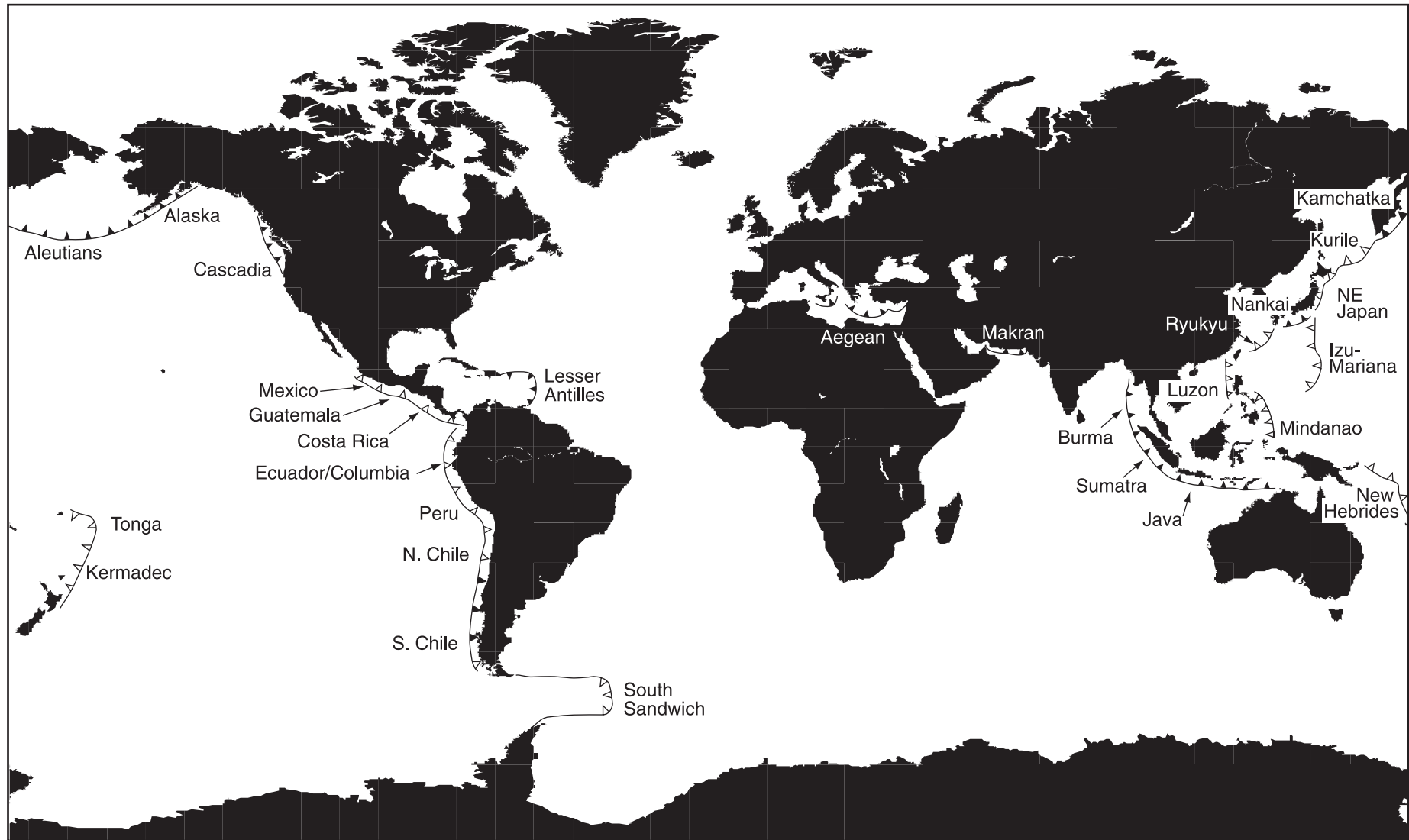


Figure 1. Map of the distribution of subduction zones worldwide from Clift and Vannucchi (2004). Solid triangles along convergent margins show the subduction zones considered to be 'accretionary margins' . Open triangles represent regions known as 'erosive margins' .

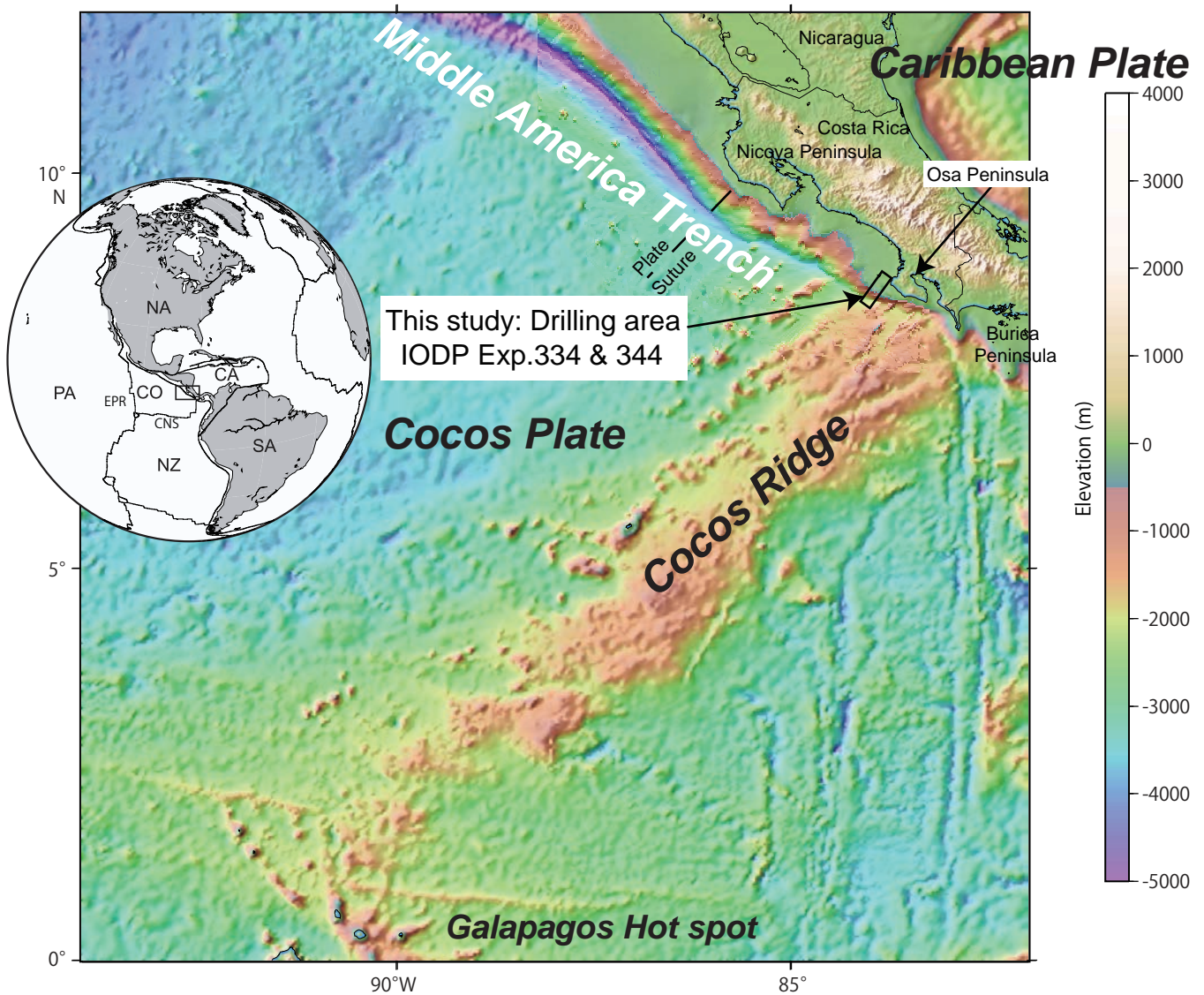


Figure 2. Topographic and bathymetric map of the study area along the Middle America Trench offshore Costa Rica and the subducting Cocos ridge, modified from Harris et al. (2013). The seafloor bathymetry presented here is based on satellite gravimetry and swath mapping (Barckhausen et al., 2001; Fisher et al., 2003; von Huene et al., 2000). *Inset:* The plate tectonics background of this region. NA: North America, CA: Caribbean Plate, SA: South America, CO: Cocos Plate, PA: Pacific, EPR: East Pacific Rise, CNS: Cocos-Nazca Spreading Center, NZ: Nazca.

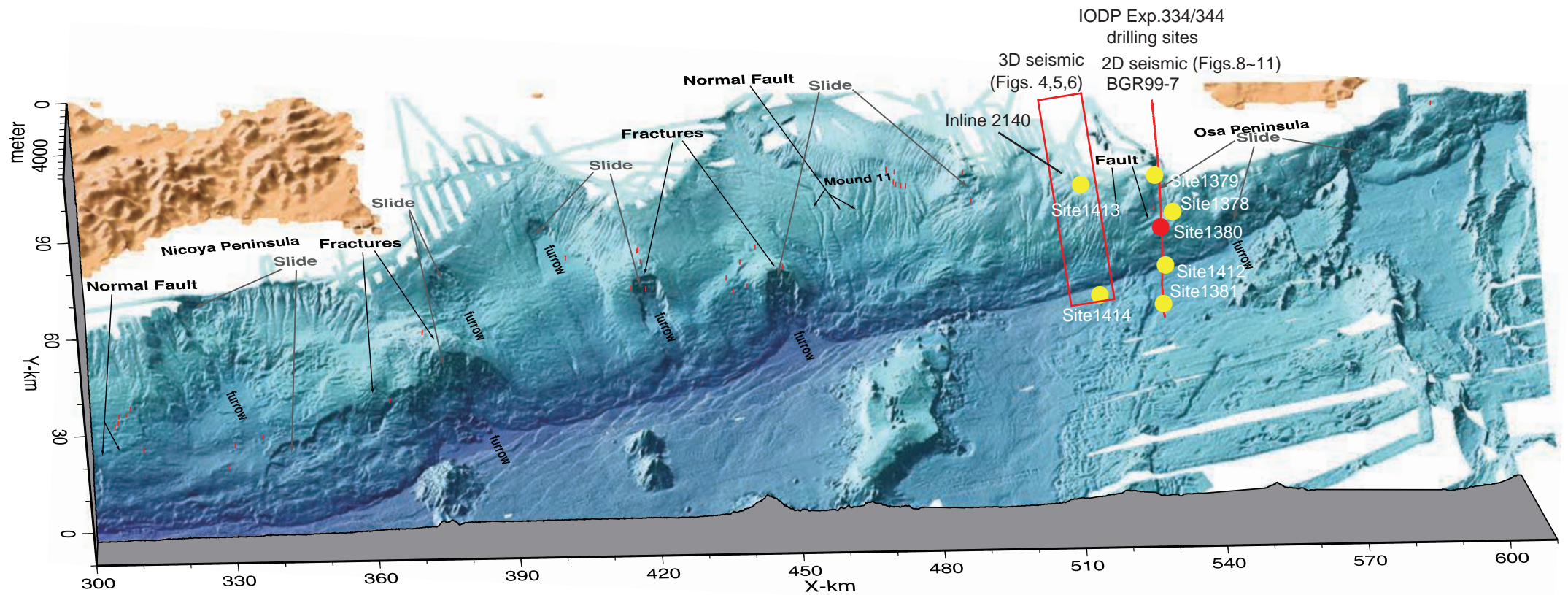


Figure 3. Multi-beam bathymetry map (SRTM mission) offshore the Costa Rica margin along the Middle America Trench (modified from Ranero et al., 2008). Structures associated with rough seafloor subduction such as fault, slide, reentrant, scarp, and seamounts are indicated from the bathymetry. Red short lines indicate the locations of seafloor seeps. Yellow and red circles represent the drilling location of IODP Expeditions 334 and 344, respectively (red circle: Site 1380). Red line: the 2D seismic reflection transect described in Figs. 8~11. Red box: the 3D seismic reflection transect described in Figs. 4~6.

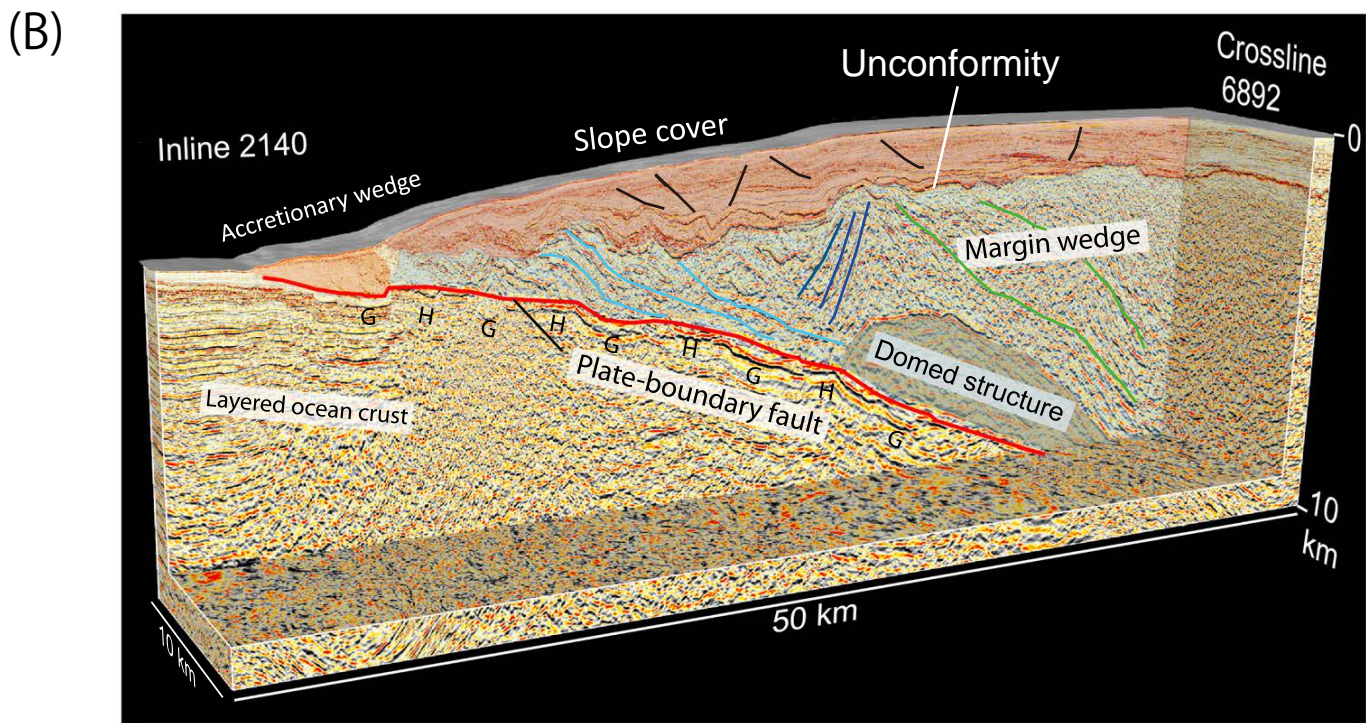
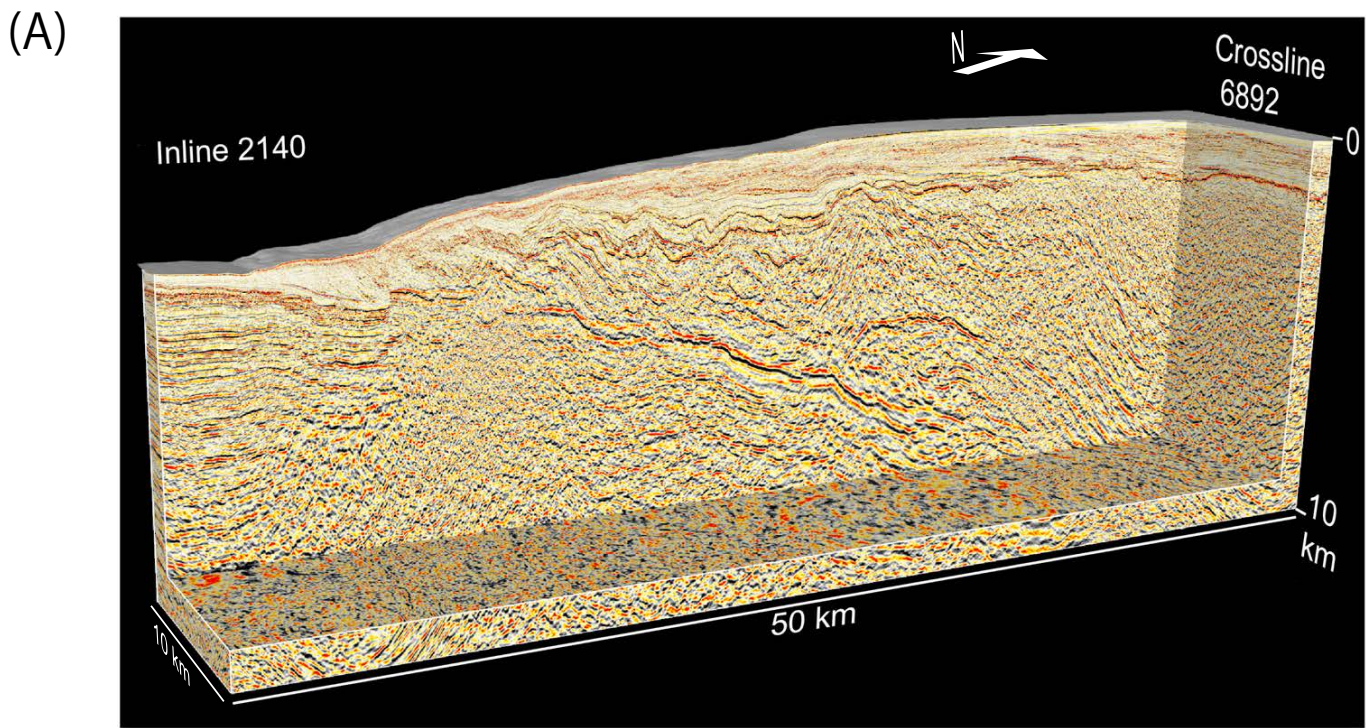


Figure 4. (A) The 3D seismic reflection transect along Inline 2140 from Bangs et al. (2015). The location is displayed in Fig. 3. (B) Structural interpretation of the wedge (Bangs et al., 2015). A major unconformity exists below the slope, which is cut by abundant normal faults (black lines). Below the unconformity, the wedge is strongly deformed by folding and faulting. Landward-dipping and seaward-dipping thrust faults are distributed from deeper regions in the wedge (colored in light blue/green and dark blue, respectively). Along the plate boundary fault, a domed structure exists at ~6 km depth, providing evidence of seamount subduction. At the trench, a small accretionary wedge has formed. The plate boundary is characterized by horst and graben structures (H, G).

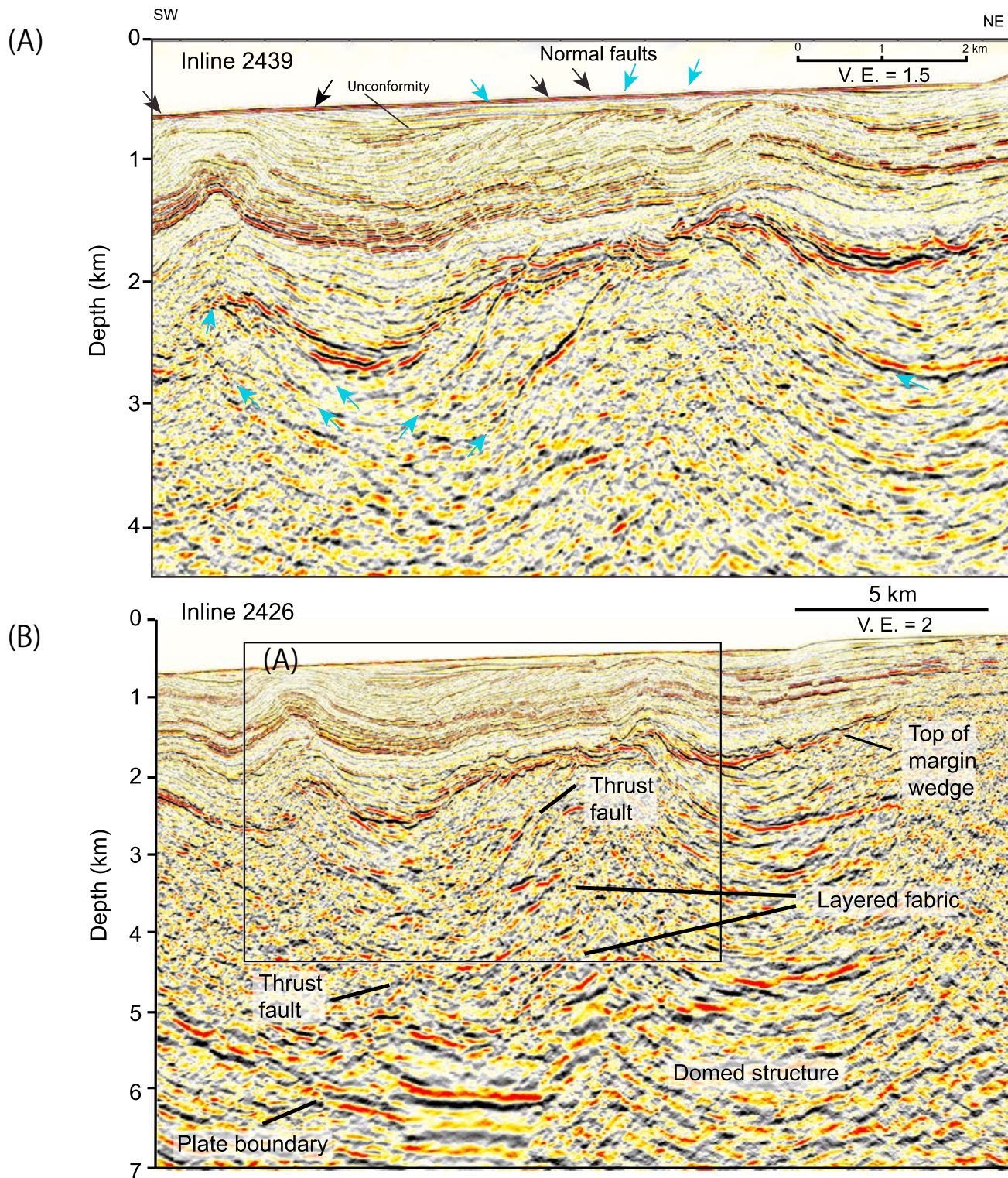


Figure 5. Representative example of structures in the slope indicated from 3D seismic reflection (Inline 2439, 2426) above the domed structure observed in Fig. 4. from Bangs et al. (2015). (A) The unconformity below the slope cover is folded, accompanied by normal faults that are abundant in the slope cover, and thrust faults that are concentrated below the unconformity cutting into the slope cover. Thrust faults occasionally cut normal faults and are associated with the folding, indicating later occurrence. Thrust faults extend down to near the plate boundary. Fault planes are characterized by high-amplitude reversed-polarity reflection. Blue and black arrows represent faults with and without fault reflections, respectively. (B) Blow-up image of the wedge along Inline 2426. Black box: the location from which panel (A) is projected.

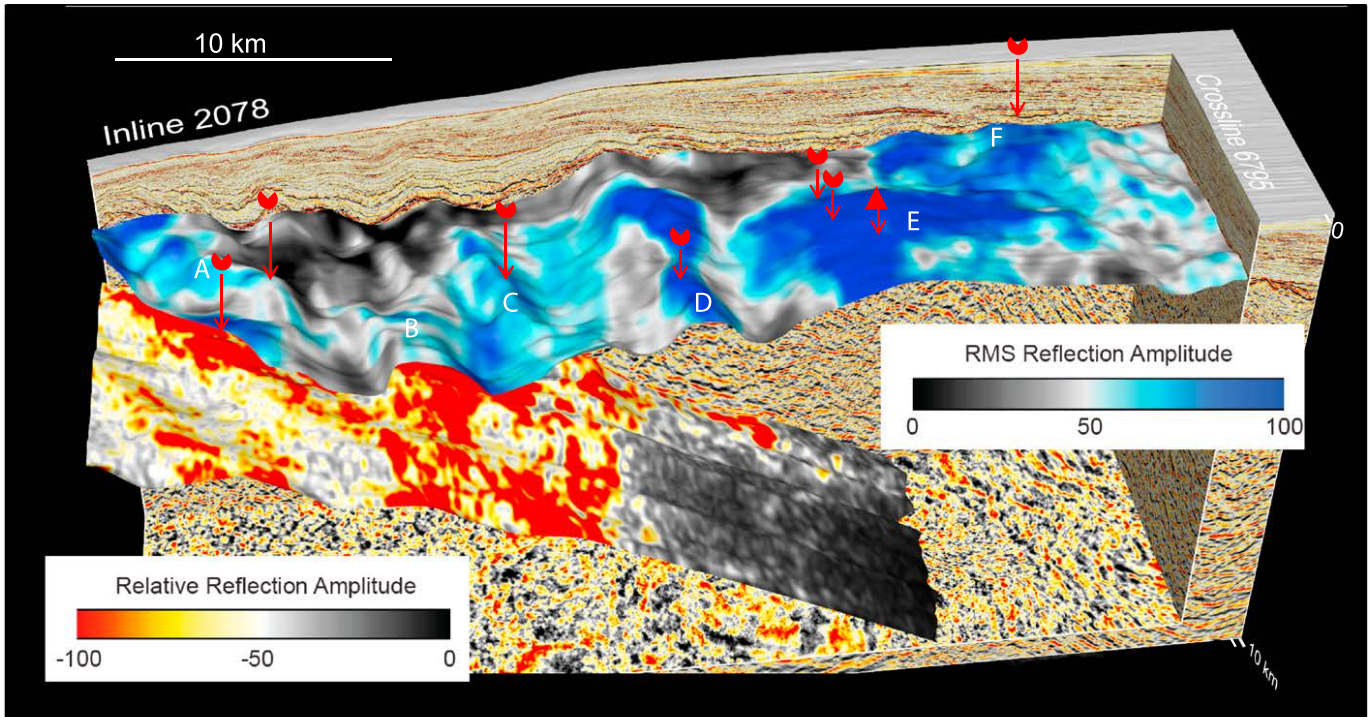


Figure 6. RMS reflection amplitude along the major unconformity and relative reflection amplitude along the plate boundary fault from 3D seismic data Inline 2078 from Bangs et al. (2015). The dark blue areas of high RMS reflection amplitude indicate zones of abundant fluid/gas migration, which is also consistent with multi-beam bathymetry studies that have detected pockmarks (red halfmoon), mud mounds, and active gas plumes (red triangle) on the seafloor (Kluesner et al. 2013). The relative reflection amplitude along the plate boundary fault shows high values until ~6 km depth, which may characterize the contrast in fluid distribution at the updip limit of the seismogenic zone (Bangs et al., 2015).

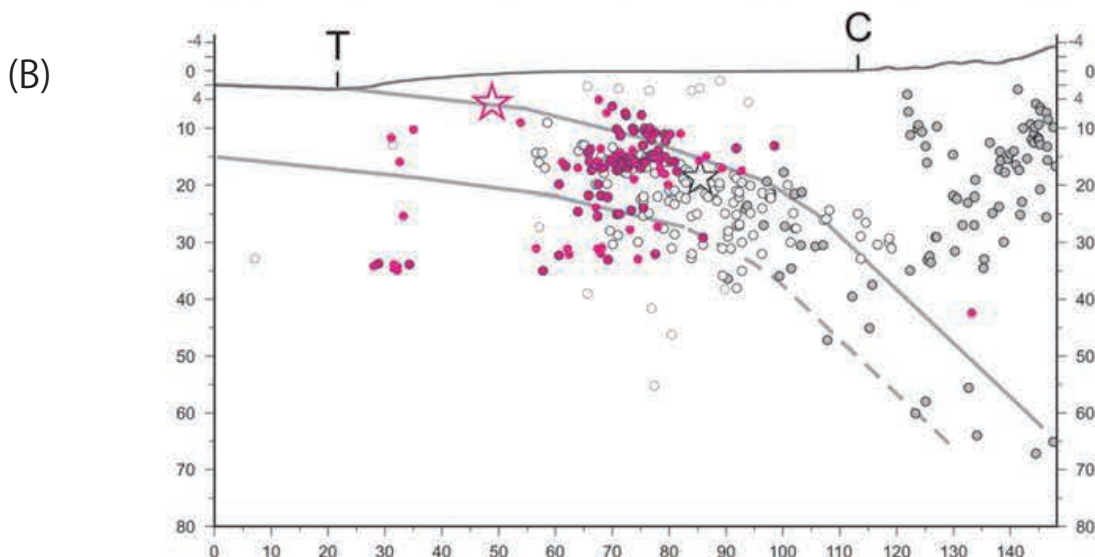
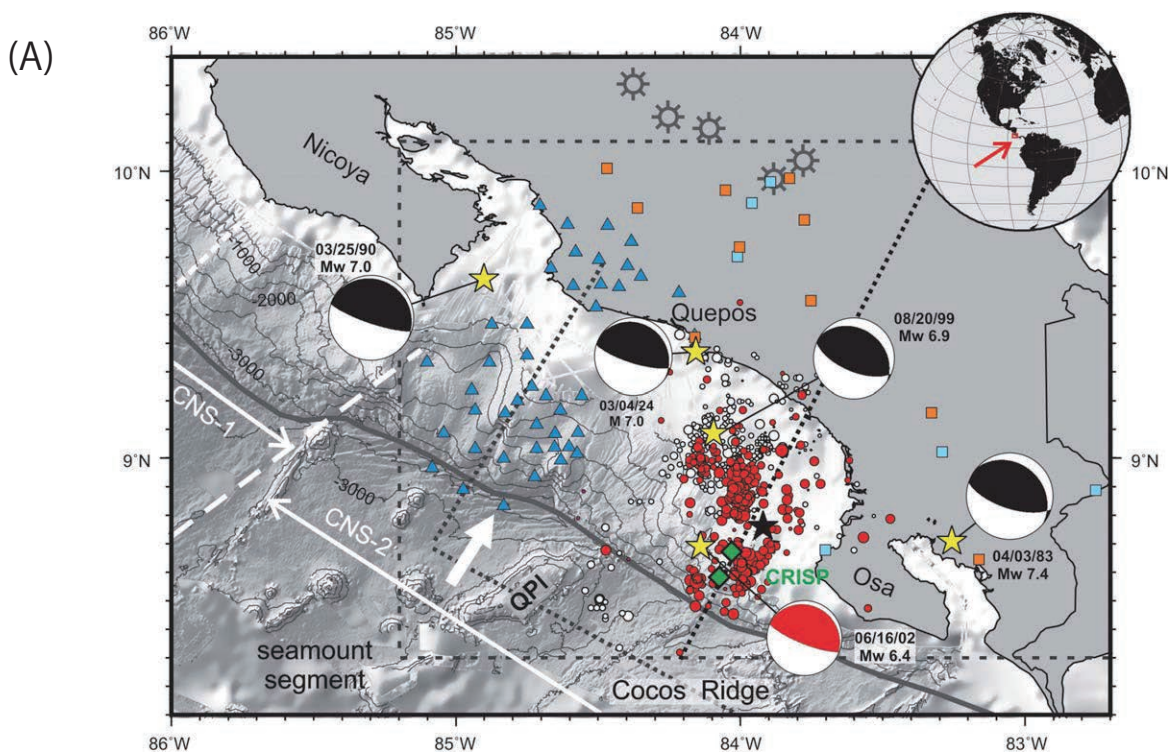


Figure 7. (A) Recent seismicity offshore Costa Rica from Arroyo et al. (2014). Red circles: the 2002 Mw 6.4 Osa earthquake sequence. White circles: the aftershocks of the 1999 Mw 6.9 Quepos sequence (DeShon et al. 2003). Blue triangles: SFB574. Orange squares: permanent networks RSN. Blue squares: OVSICORI. Yellow stars: epicenters of recent large earthquakes associated with subduction of bathymetric highs: 1924 M7.0 Quepos (Arce and Doser, 2009), 1983 Mw7.4 Golfito (Adamek et al., 1987), 1990 Mw7.0 Cobano (Husen et al., 2002), 1999 Mw6.9 Quespos (RSN), and 2002 Mw6.4 Osa (gCMT). Black star: the global location of the 2002 Osa main shock from NEIC. Green diamond: the drilling location of IODP Expedition 334 and 344. (B) Seismicity cross-section of 1D relocation from Arroyo et al. (2014). Magenta and white stars: the main shock relocations of the 2002 Mw6.4 Osa earthquake (Arroyo et al., 2014) and the 1999 Mw6.9 Quespos earthquake by RSN, respectively. Magenta and white circles: aftershocks for the Osa and Quespos events, respectively. Gray circles: earthquakes based on tomography data from Husen et al. (2003). T: trench axis. C: coast positions.

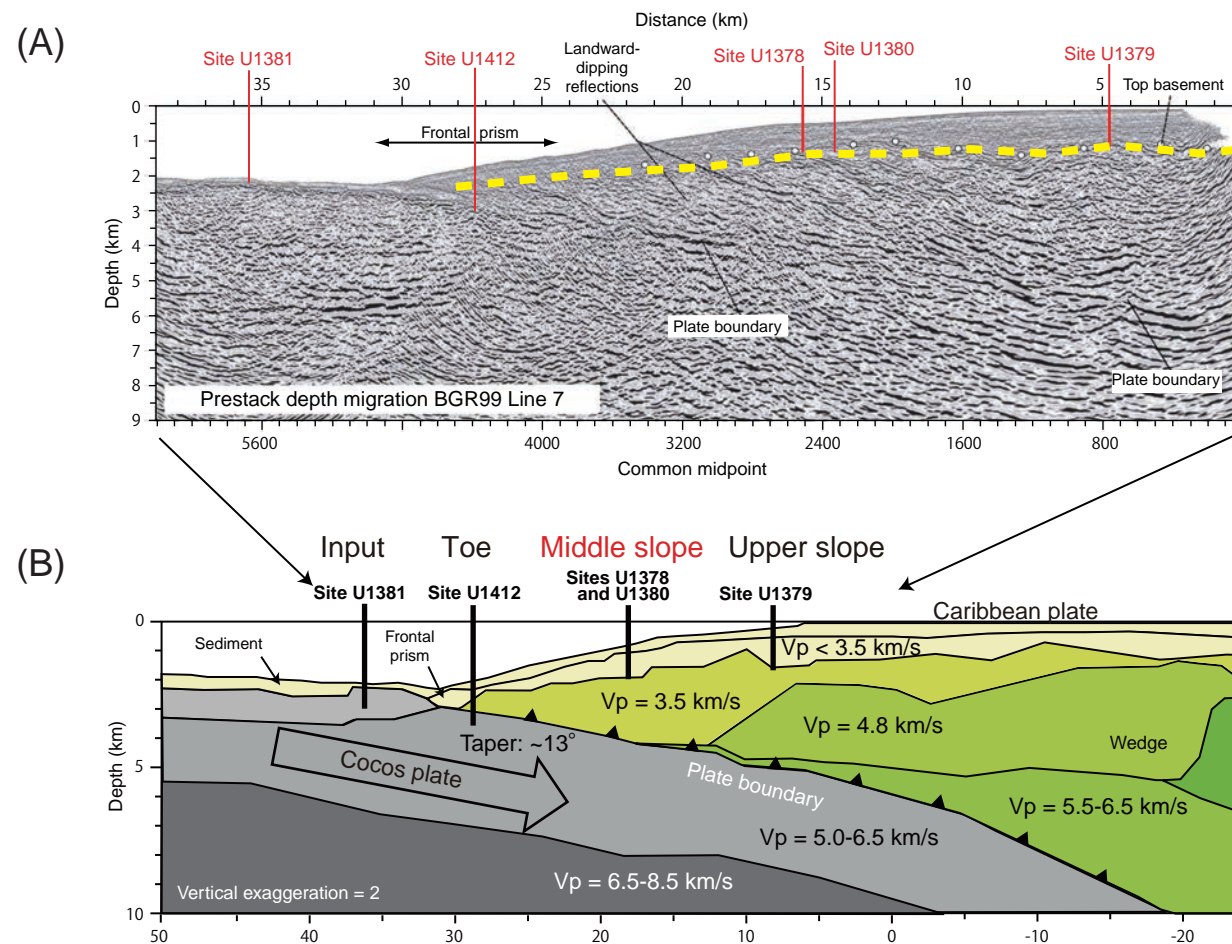


Figure 8. (A) Seismic Line BGR99-7 showing the location of the Expedition 344 drill sites from C. R. Ranero, unpubl. data reproduced in Harris et al. (2013). Yellow-dotted line: the major seismic reflector beneath the slope. (B) Schematic P-wave velocity structure through the drill sites offshore Osa Peninsula from Harris et al. (2013) based on an interpreted wide-angle seismic section from Stavenhagen et al. (1998).

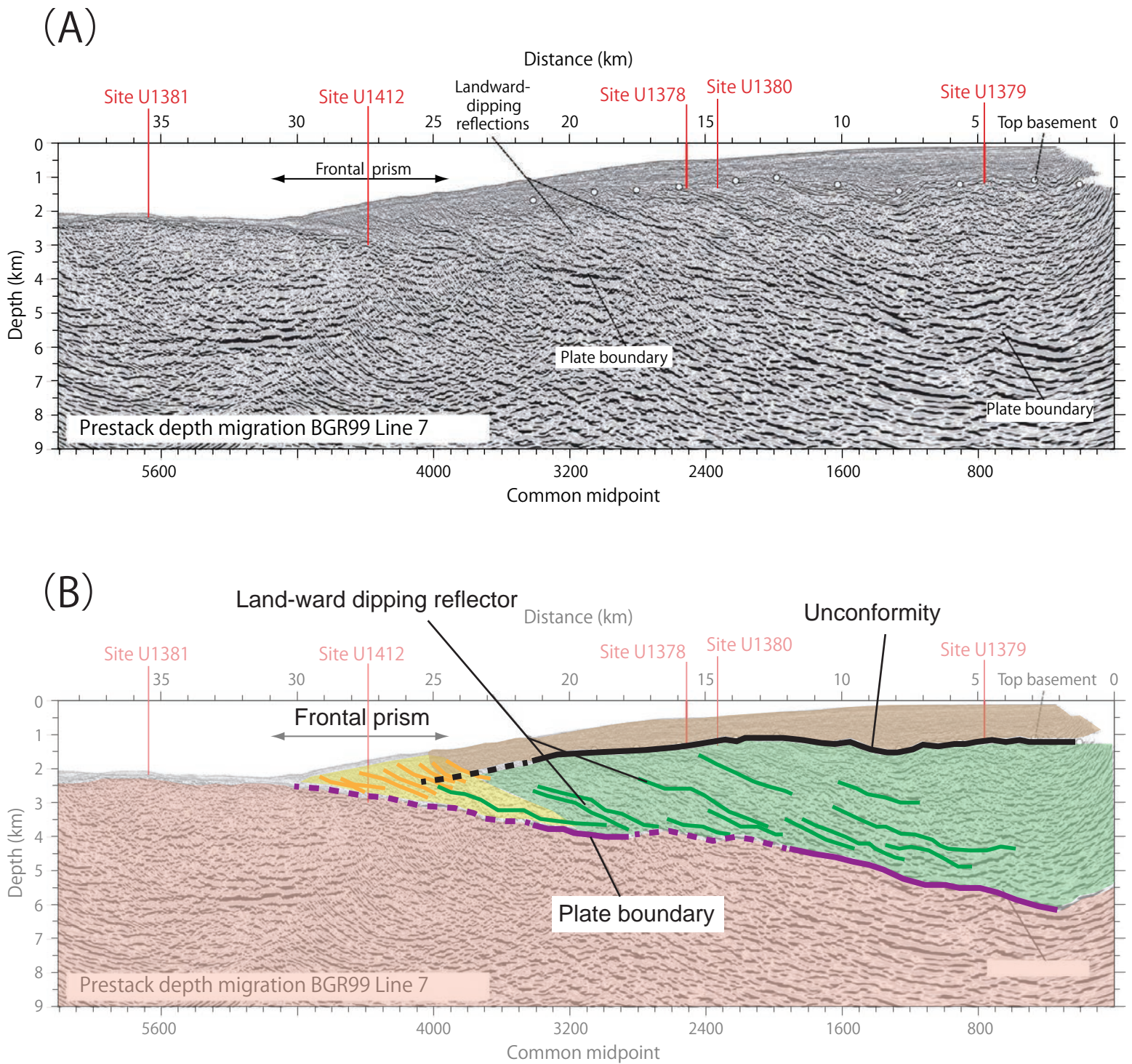


Figure 9. (A) Seismic Line BGR99-7 along the drilling transect of Expedition 344 from C. R. Ranero, unpubl. data reproduced in Harris et al. (2013). (B) Structural interpretation of the wedge based on the seismic image of (A). Black line: the major unconformity beneath the slope. Purple line: the plate boundary. Shaded green: the wedge margin beneath the major unconformity. Green line: the land-ward dipping reflectors in the wedge margin beneath the major unconformity. Shaded yellow: the frontal accretionary prism. Orange line: the land-ward dipping reflectors in the frontal prism. Shaded light brown: the slope cover above the major unconformity. Shaded pink: the subducting Cocos Plate.

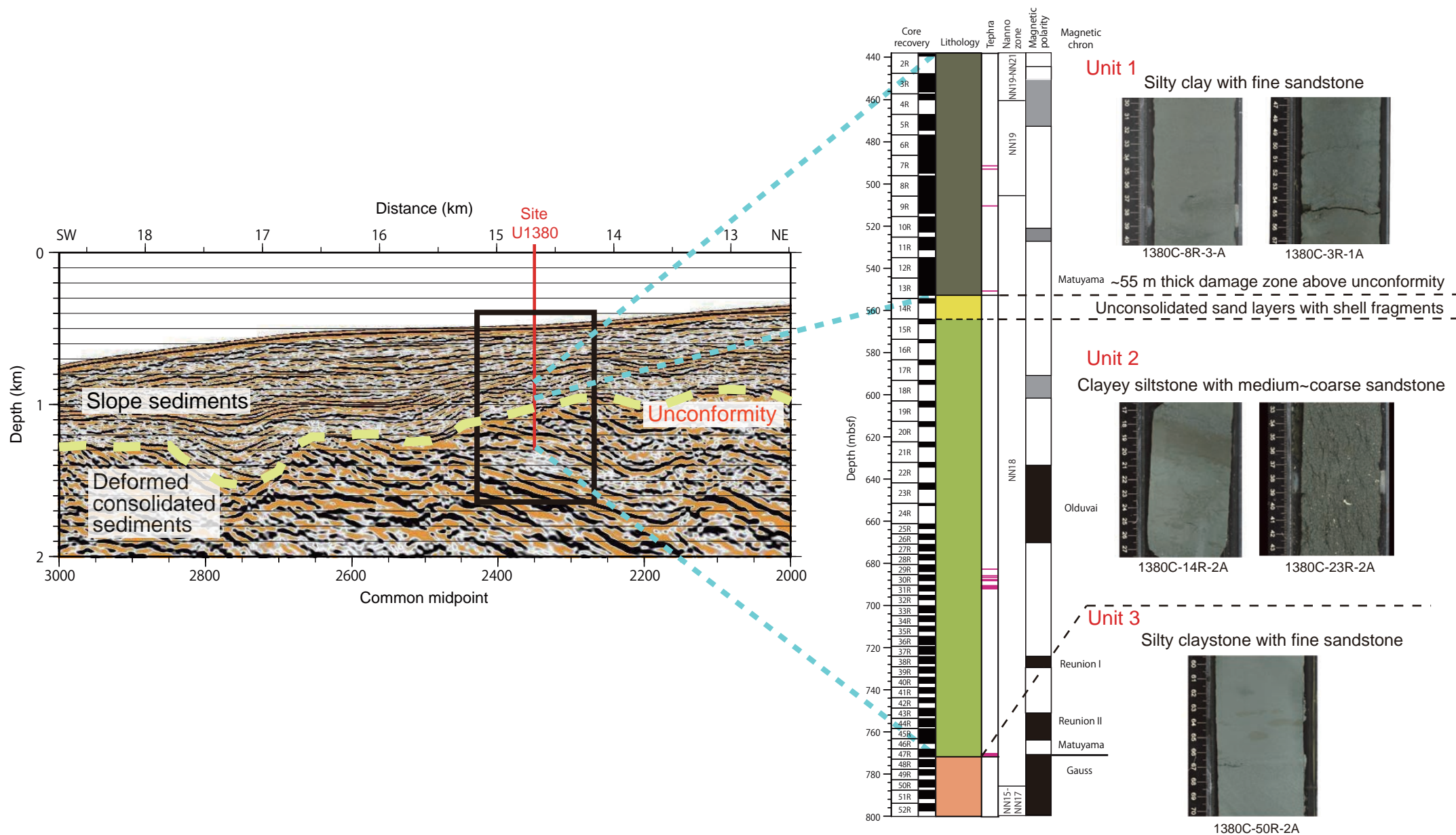


Figure 10. *Left:* Prestack time-migrated depth section along the seismic Line BGR99-7 centered at Site 1380 (C. R. Ranero, unpubl. data reproduced in Harris et al., 2013) (black box). Yellow dotted line: the major seismic facies boundary. Blue dotted line: the drilled range at Site 1380 during Expedition 344. *Right:* Lithostratigraphic summary of Site 1380C and representative image of Units 1, 2, and 3 (from Harris et al., 2013). Biostratigraphic zones determined by nannofossil content and paleomanostratigraphy/magnetic chronology based on the results of characteristic remanence (Black: normal polarity, white: reversed polarity, gray: uncertain polarity) during Expedition 344. Red bars indicate distribution of tephra layers.

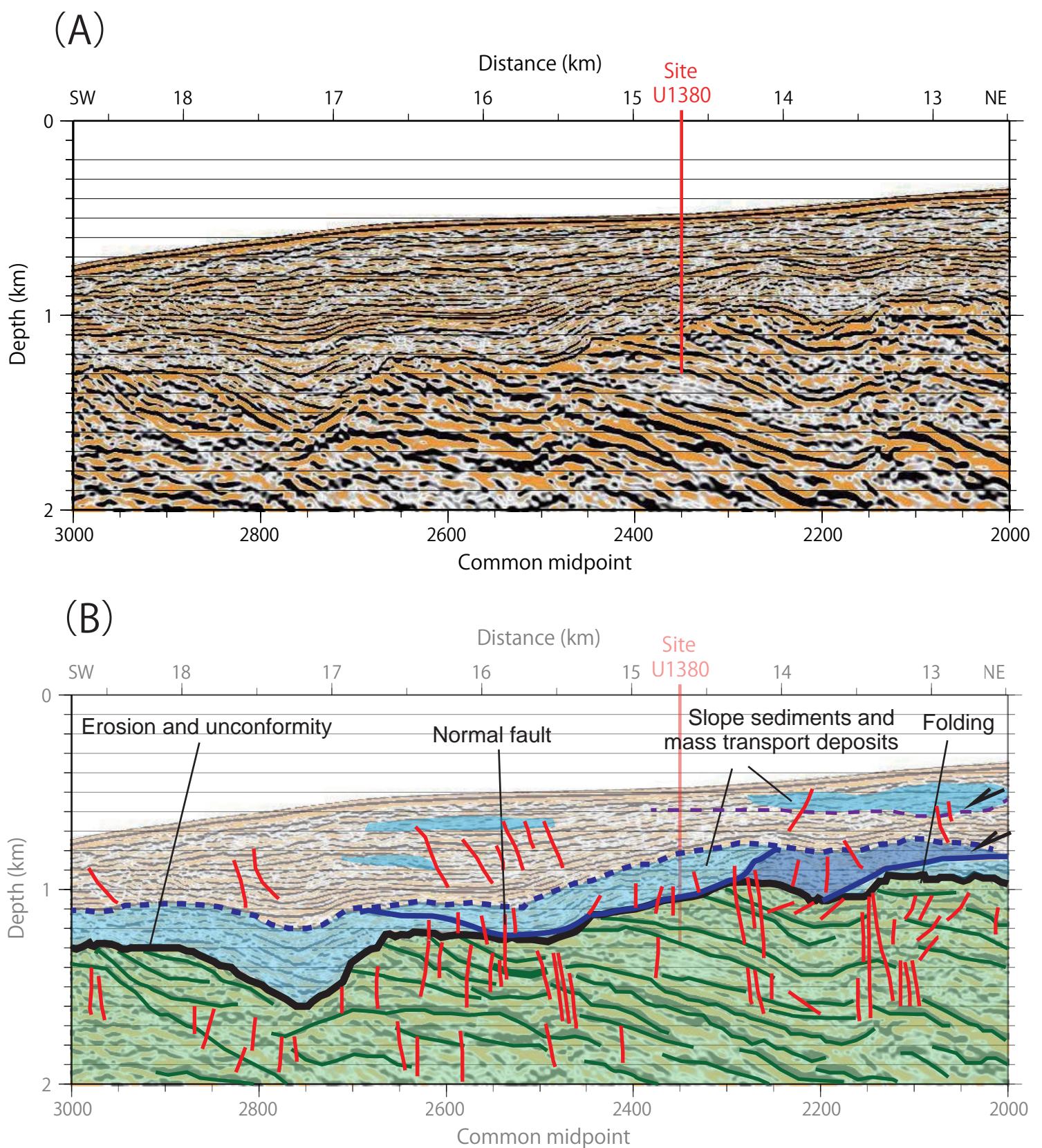


Figure 11. (A) Enlarged prestack time-migrated seismic section BGR99-7 focusing on Site 1380 (from C. R. Ranero, unpubl. data reproduced in Harris et al., 2013). **(B)** Structural interpretation of (A) in this study. The major unconformity beneath the slope is represented by the black line, and abundant faults that are mainly normal faults are colored in red. Below the unconformity, landward-dipping reflectors are present cut clearly by the unconformity, indicating erosion. Above the unconformity, a zone including areas where the layers are less defined is present, which may characterize mass transport deposits (colored in blue; slump deposits are especially indicated in dark blue-colored zones). Slope failure and mass movement have likely occurred along the unconformity, especially along smooth outlines (blue lines). The unconformity and sedimentary layers are folded, accompanied by faulting. Mass movement may form a new unconformity above the sediment deposits (blue-dotted line). Similar mass transport deposits are also inferred to exist within the shallower portion of the slope.

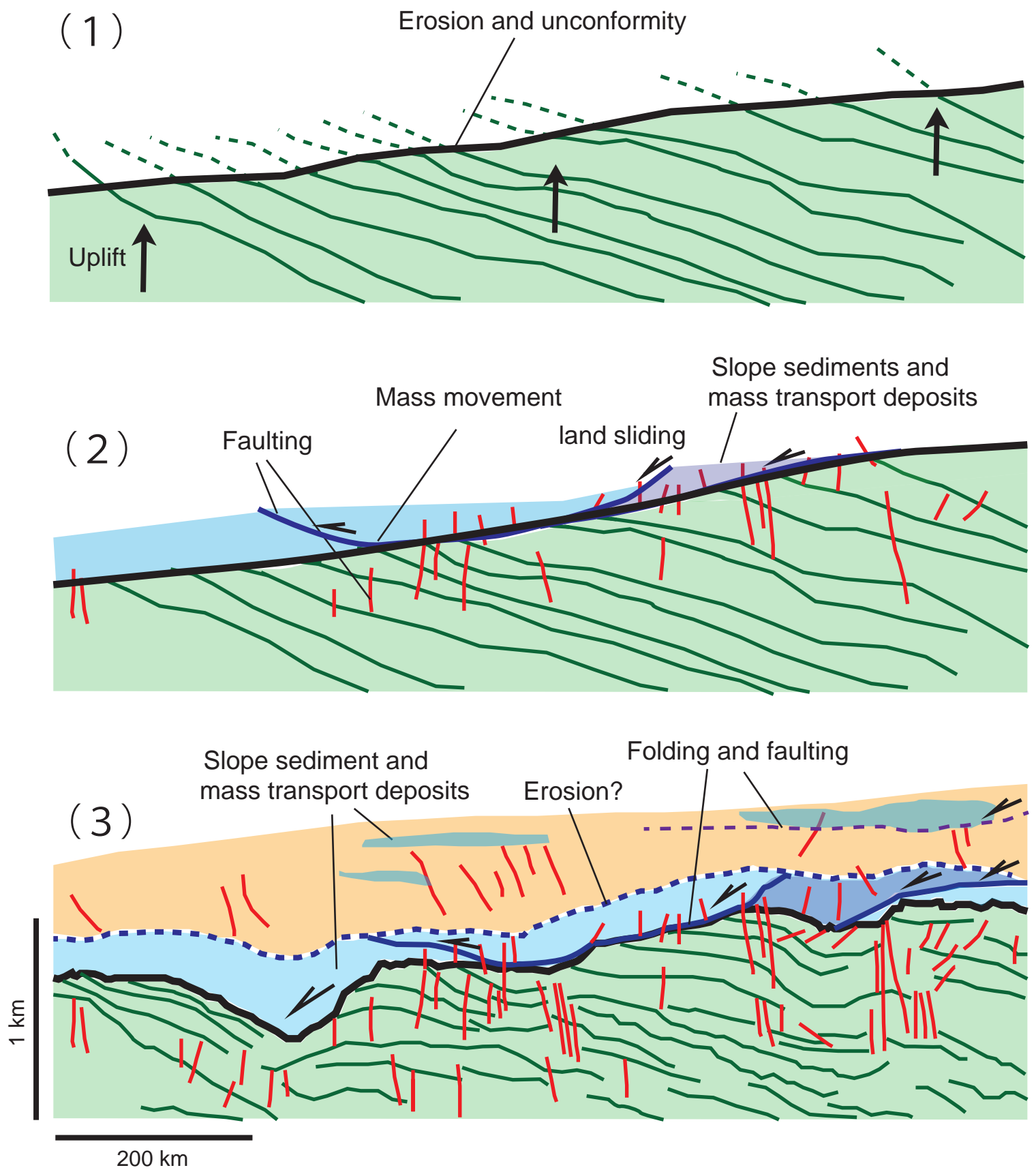


Figure 12. Structural development in the order of occurrence in the study area (Site 1380) interpreted from the seismic image (Fig.11). (1) Uplift and erosion of the wedge (shaded green) involving mass movement, creating the unconformity (black line). (2) Slope sediments and mass transport material (colored blue) are deposited above the unconformity. The mass movement (along the blue line) involves normal faulting (blue and red lines). (3) The mass movement may create additional erosion (blue dotted line) followed by slope sediment deposition. The unconformity and sedimentary layers are folded, cut by and accompanied by abundant faulting. A landslide also occurred in the shallow portion of the slope associated with faulting and folding.

(A)



(B)

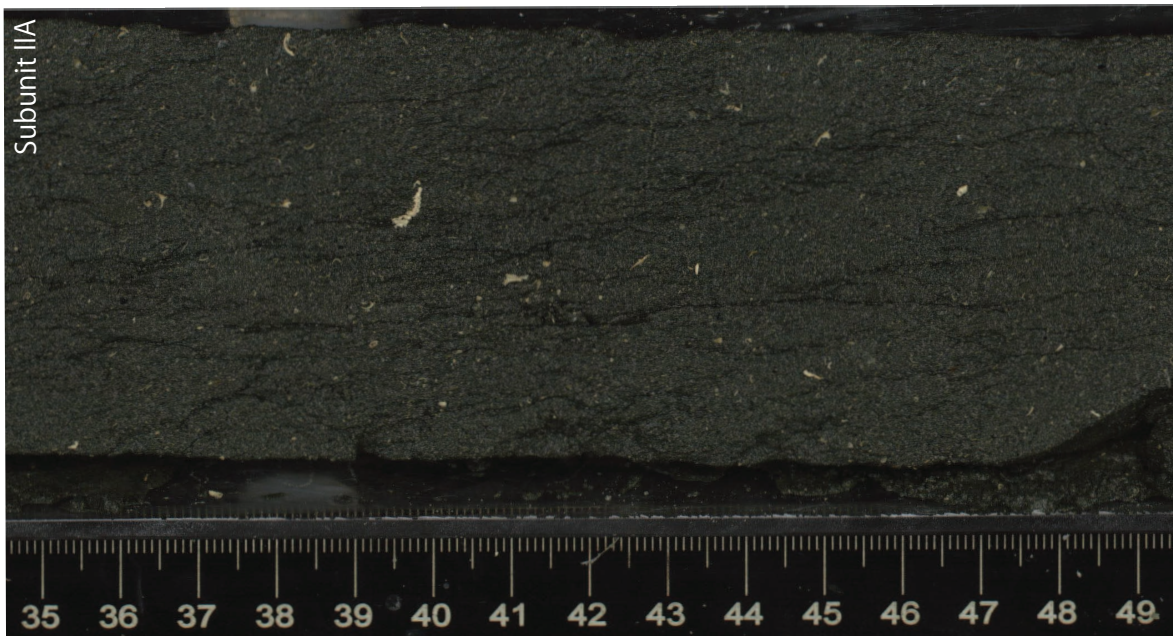


Figure 13. Core (section half) photos at Site 1380 from Harris et al. (2013). **(A)** Intensely deformed fault zones of ~53 m thickness at ~2.5 m above the unconformity. Brecciated intervals and fractured intervals are dominant. The photos are taken from 13R2W, 3W, and 4W (within 453.8~477.7 mbsf). **(B)** The unconsolidated medium to coarse sandstone layers (~12 m thick) containing abundant shell fragments considered to be beach deposits distributed above the consolidated sediments of Unit 2 across the unconformity. The photo is taken from 14R2W.

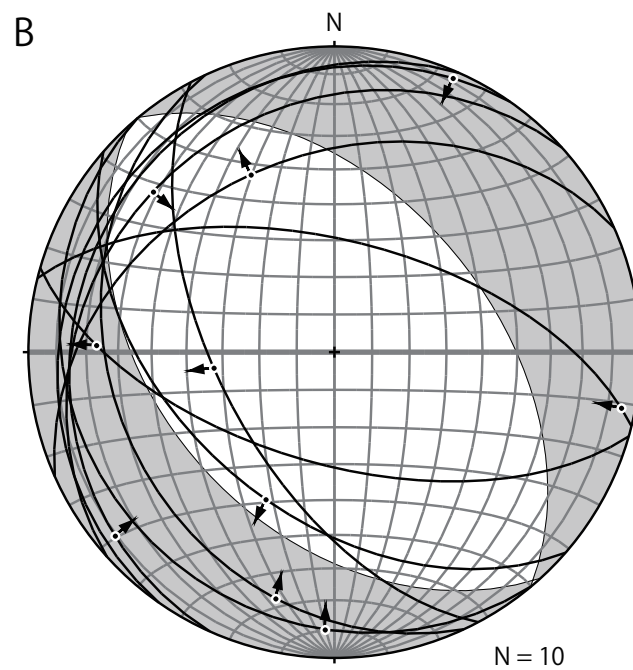
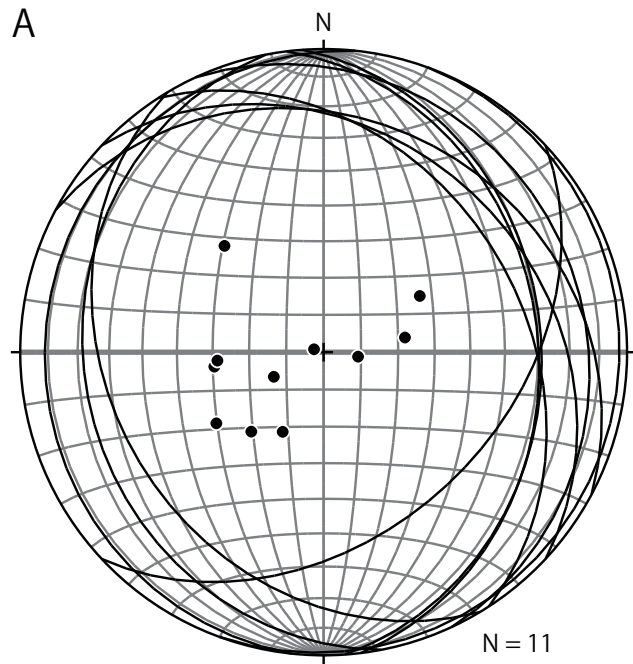


Figure 14. Site 1380 stereographic diagram of projected (A) bedding planes and (B) fault kinematics after paleomagnetic correction from Harris et al. (2013). Bedding planes show a general NW-SE strike with dip angles between 10° and 30° NE and SW, respectively. Black dots: π poles. Black curved lines: π circles. Black arrows: fault slip direction. Shaded in gray : extensional region. Shaded in white: compressional region. Fault kinematics indicate a normal fault stress regime with σ_1 and σ_3 oriented vertically in NE-SW.

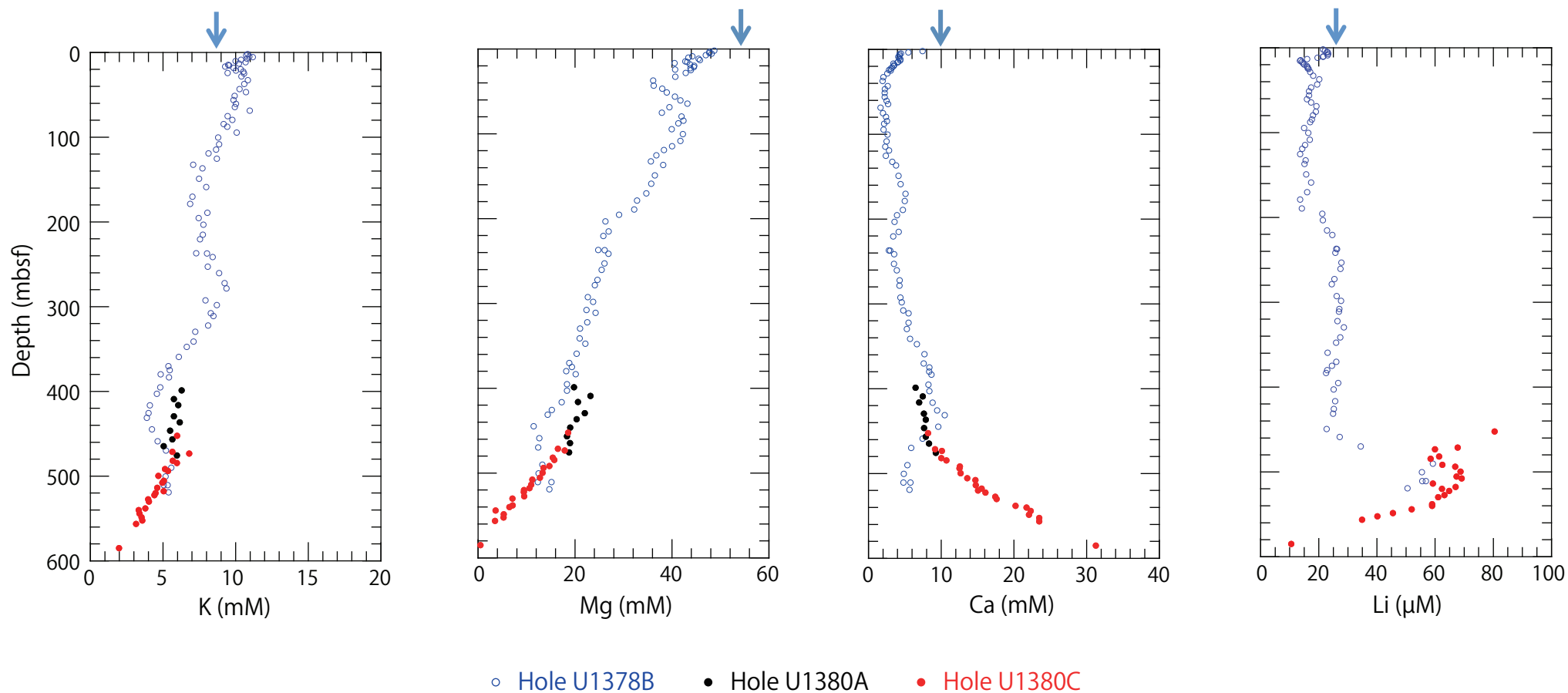


Figure 15. Shipboard pore-water geochemistry results showing downholed profiles of potassium, magnesium, calcium, and lithium collected at Site 1380C from Harris et al. (2013) and at Site 1378B and Site 1380A from Vannucchi et al. (2012). Blue arrows: bottom seawater values. The data for lithium at Site 1378B is from Torres et al. (2014).

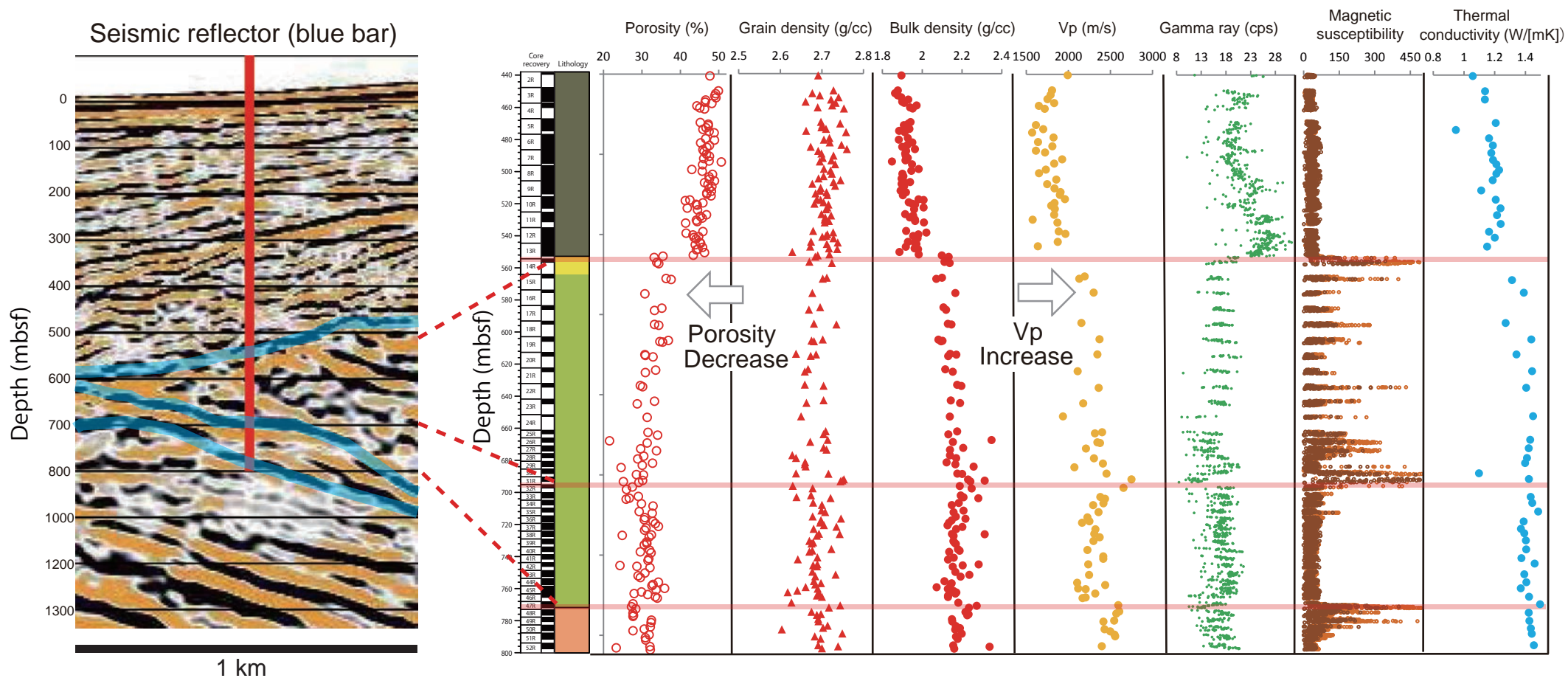


Figure 16. *Left:* Close-up section of seismic Line BGR99-7 at Site 1380 (C.R. Ranero, unpubl. data reproduced in Harris et al. 2013) from Figure 10 showing seismic reflectors (blue bars). *Right:* Physical property results obtained during Expedition 344 (Harris et al., 2013): Discrete sample porosity, wet bulk density, and grain density using the MAD mass/volume Method C, P-wave velocity measured on split cores in the x-direction, downhole profiles for natural gamma radiation acquired using a multisensory core logger, volumetric magnetic susceptibilities measured using the whole-round multisensory logger, and thermal conductivity values obtained from the probe measurements. Red horizontal lines: the lithostratigraphic unit boundaries. Lithostratigraphic unit boundaries and physical property transitions in the drilled range correlate well with the major seismic reflectors at this horizon (blue bars).

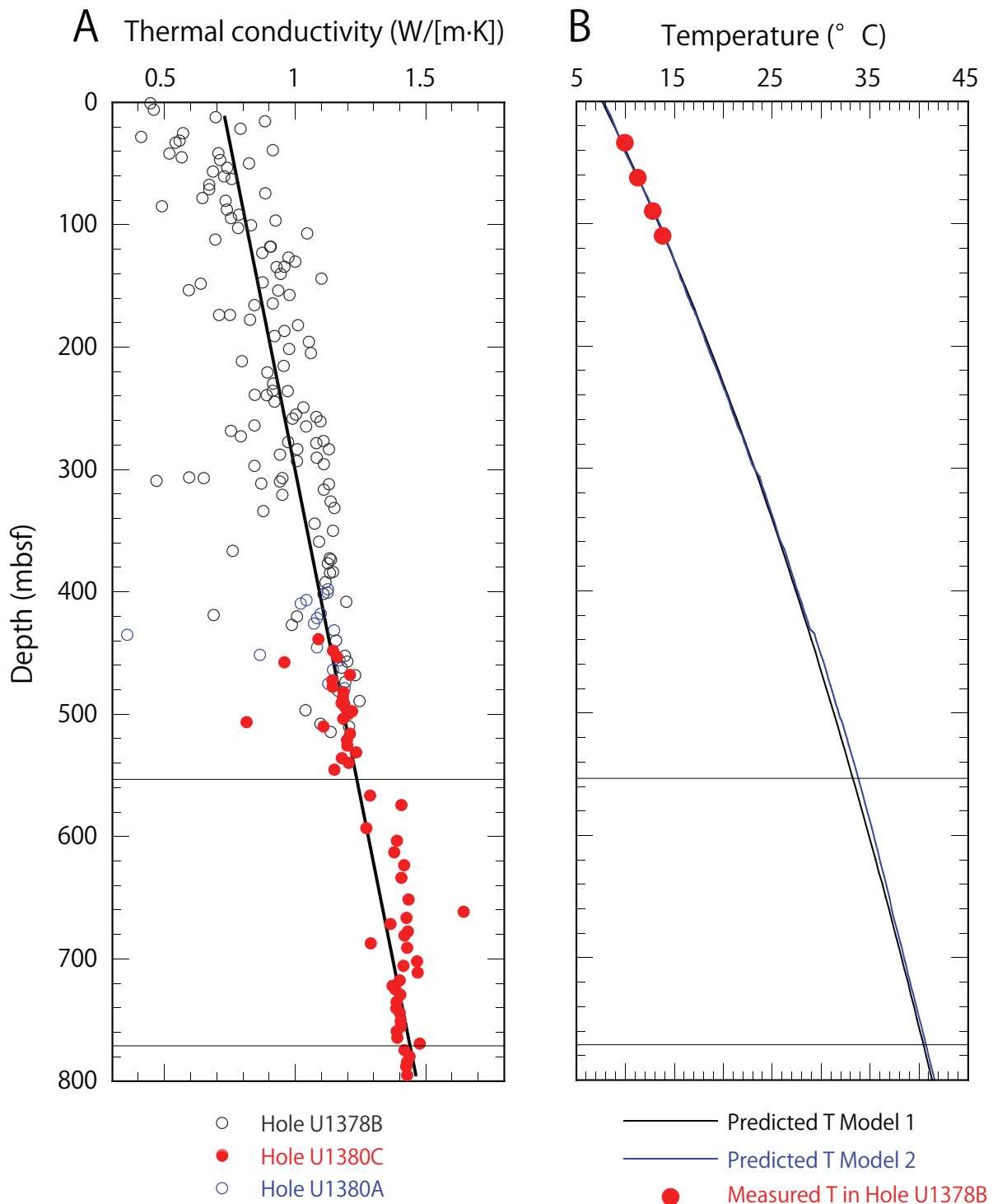
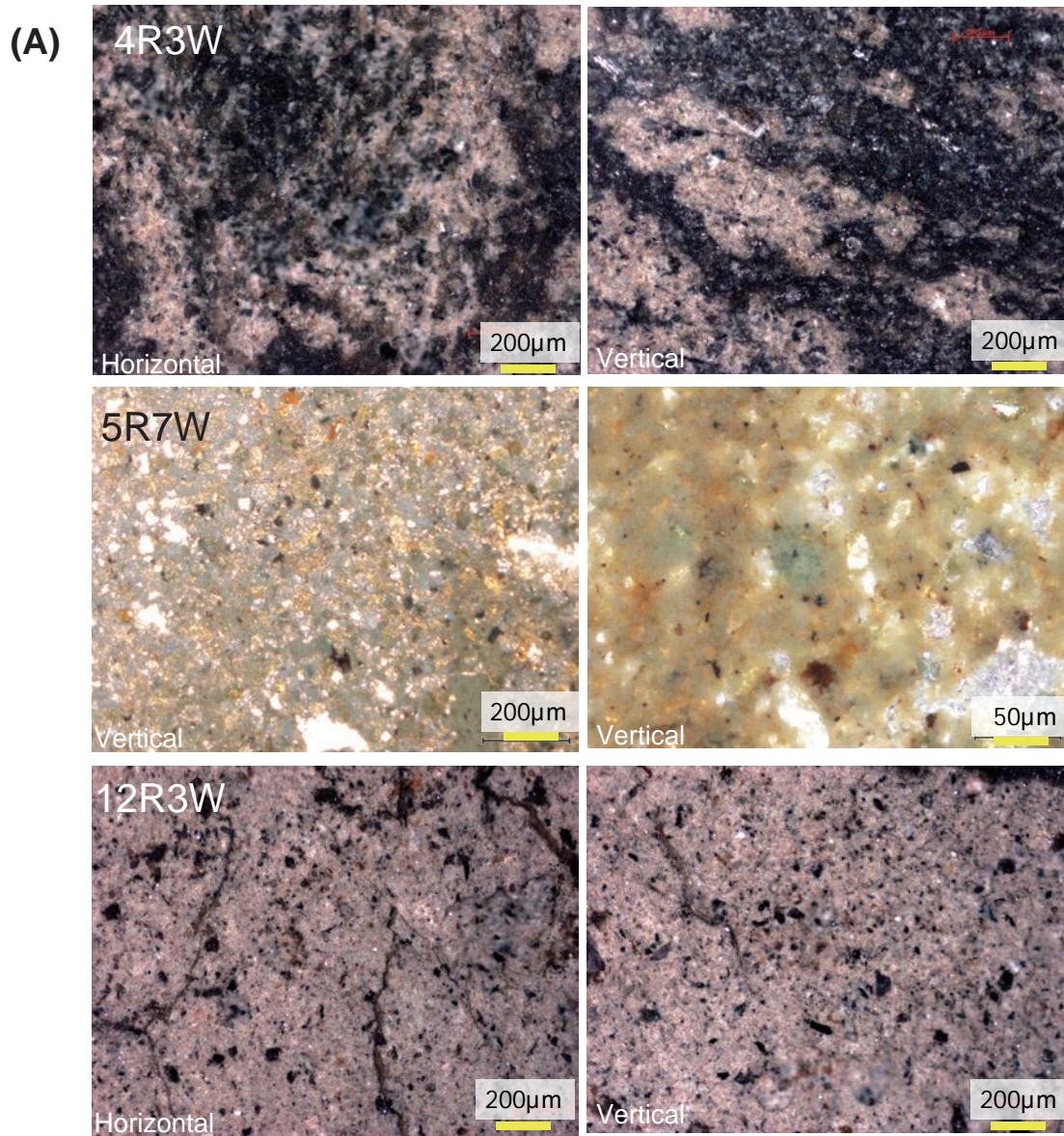


Figure 17. (A) Shipboard measurements of thermal conductivity at Site 1378 and 1380 from Harris et al. (2013). The results are best fit linearly by $y=0.72+0.00093x$ ($R=0.88$). **(B)** Red dots: the measured temperatures in Hole U1378B (Vannucchi et al., 2012). Thermal gradient is modeled using equilibrium temperatures from linear fit of thermal conductivity (black curved line: T Model 1) and from precise thermal conductivity measurements with depth (blue curved line: T Model 2) (from Harris et al., 2013). Horizontal black lines: the lithostratigraphic unit boundaries.



(B)

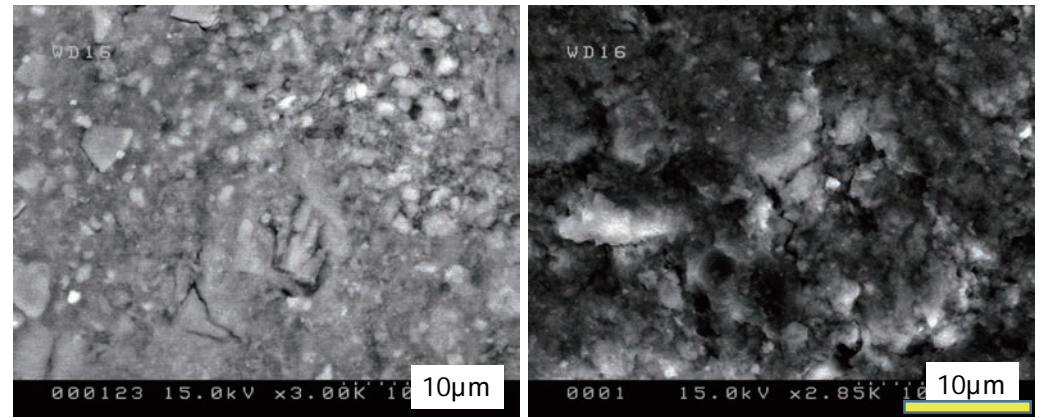


Figure 18. Representative microstructural image observed by optical microscopy (A) and scanning electron microscopy (SEM) (B) of cross-sections of lithostratigraphic Unit 1 from Site 1380 in the vertical and horizontal directions.

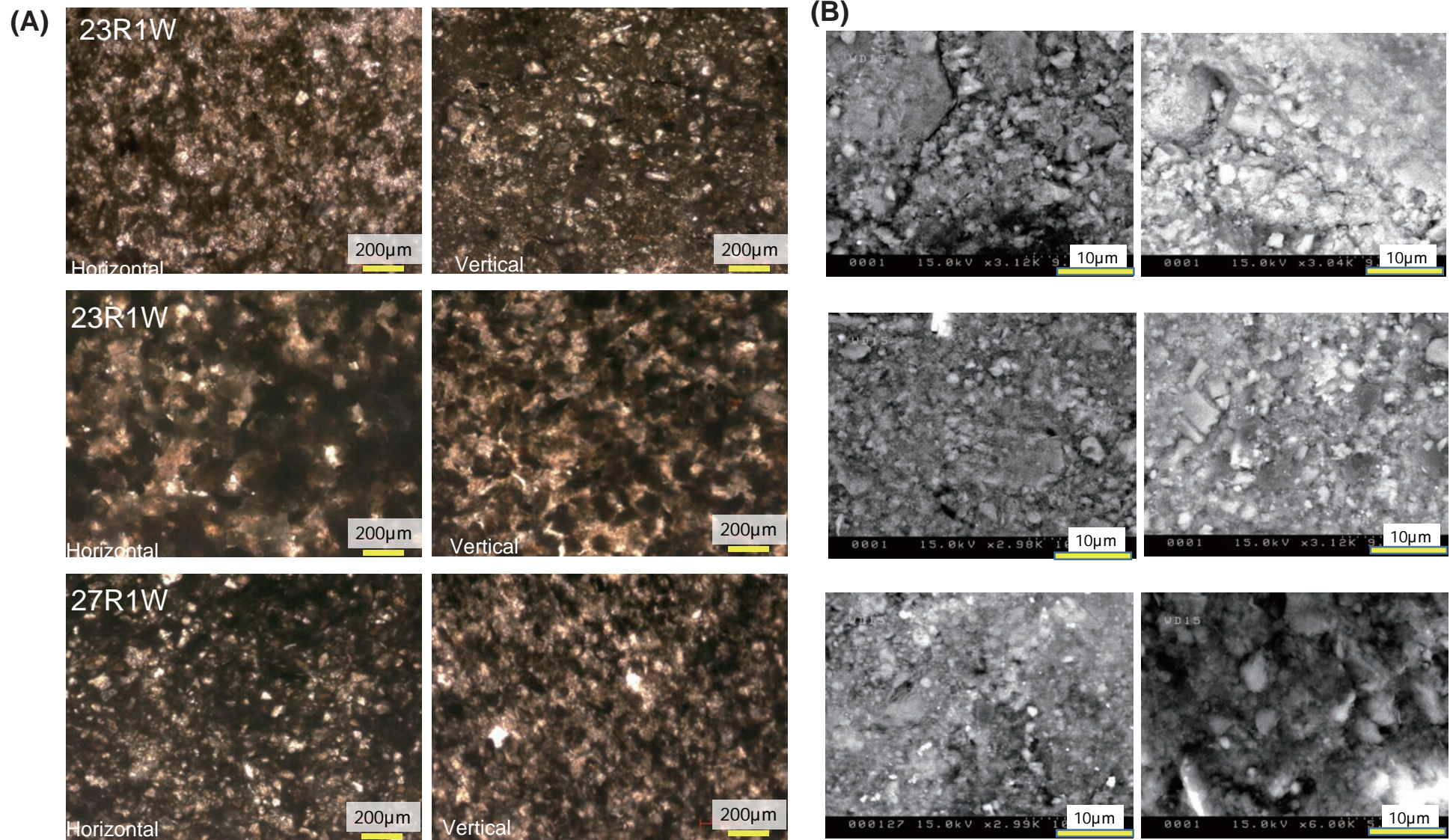


Figure 19. Representative microstructural image observed by optical microscopy (A) and scanning electron microscopy (SEM) (B) of cross-sections of the upper (~552–707 mbsf) lithostratigraphic Unit 2 from Site 1380 in the vertical and horizontal directions.

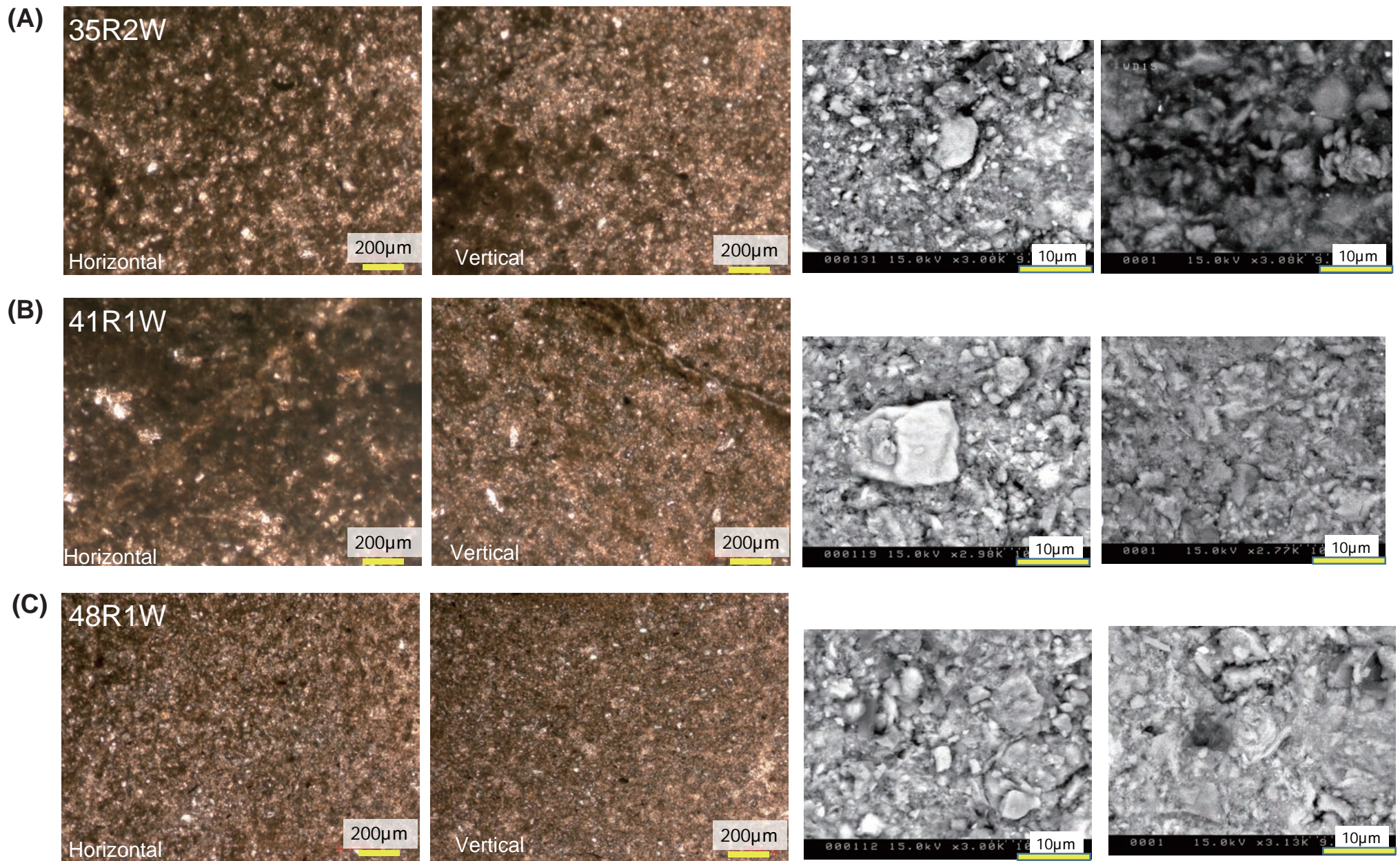


Figure 20. Representative microstructural image observed by optical microscopy and scanning electron microscopy (SEM) of cross-sections of the lower (~707–772 mbsf) lithostratigraphic Unit 2 (A, B) and Unit 3 (C) from Site 1380 in the vertical and horizontal directions.

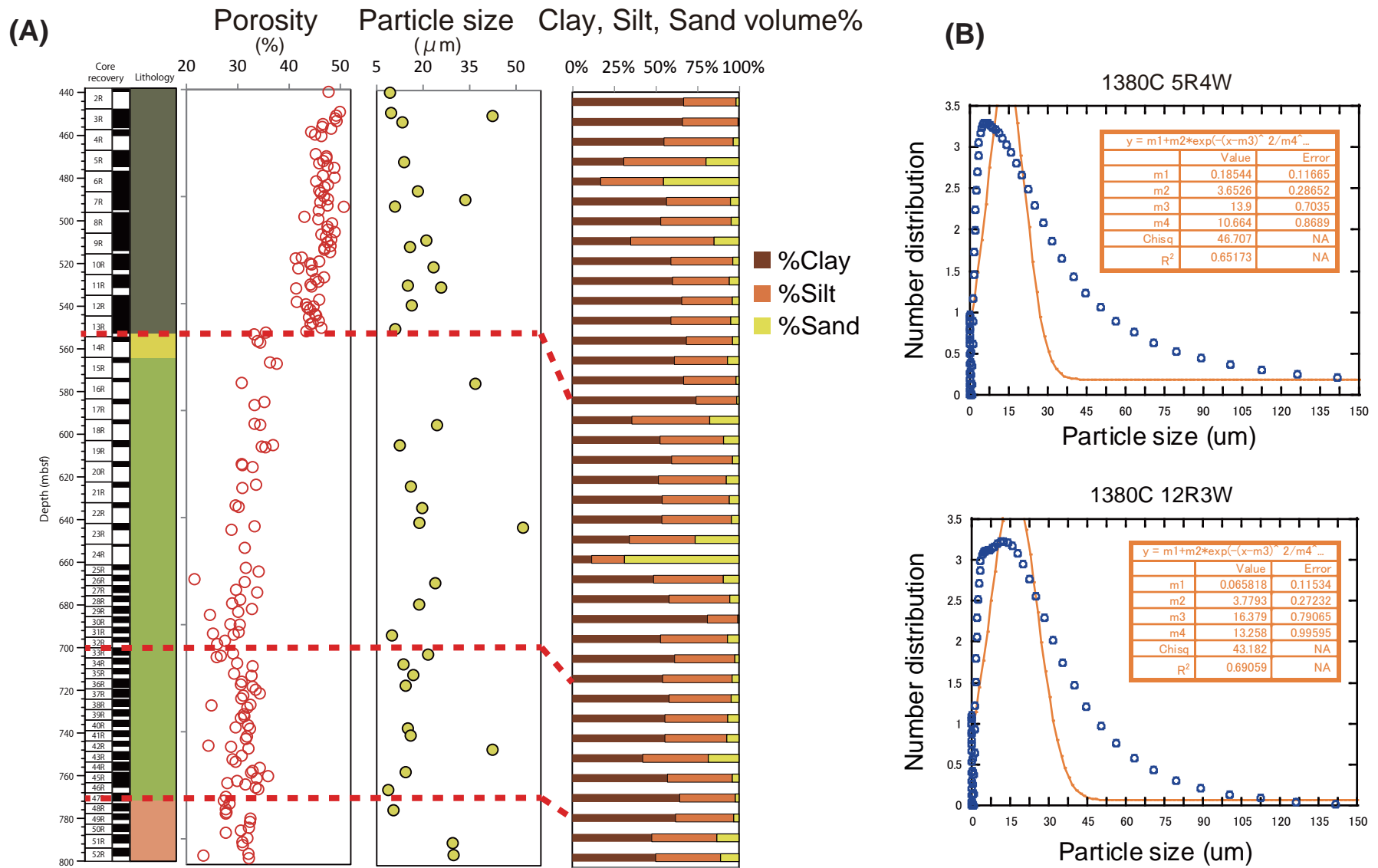


Figure 21. (A) Discrete sample porosity (shipboard) and results of the measured average particle size (this study). Clay, silt, sand volume% were derived from the particle size fraction. Red dotted lines: lithostratigraphic unit boundaries and physical property transitions. **(B)** Number distribution of particle sizes. Finer grains exhibit larger number distributions.

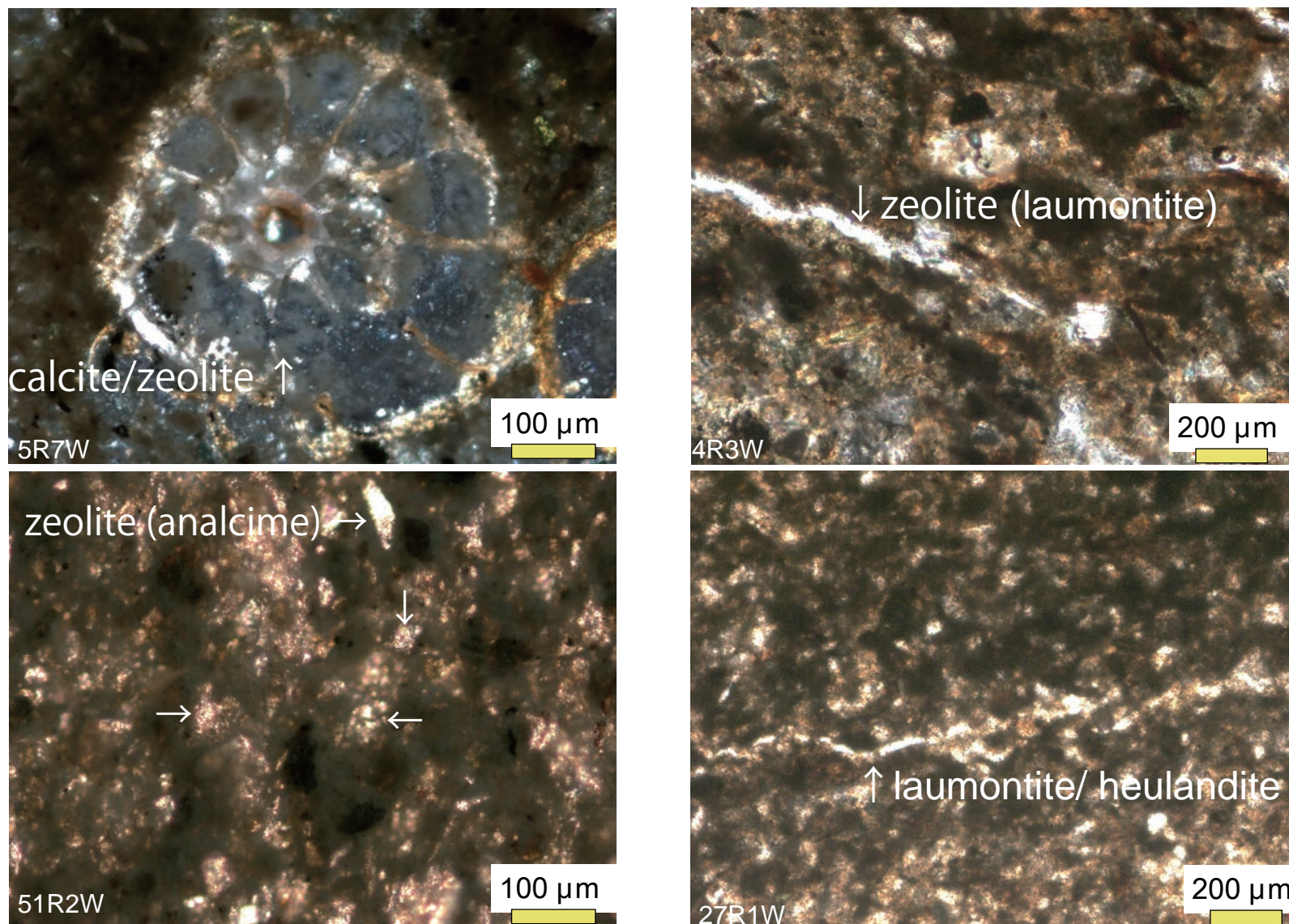


Figure 22. Microstructural observations of the zeolites analcime, heulandite, and laumontite. Analcime is observed to precipitate in pores and/or nanofossil shells, whereas laumontite and heulandite are occasionally precipitated in pores, shells, and mineral veins.

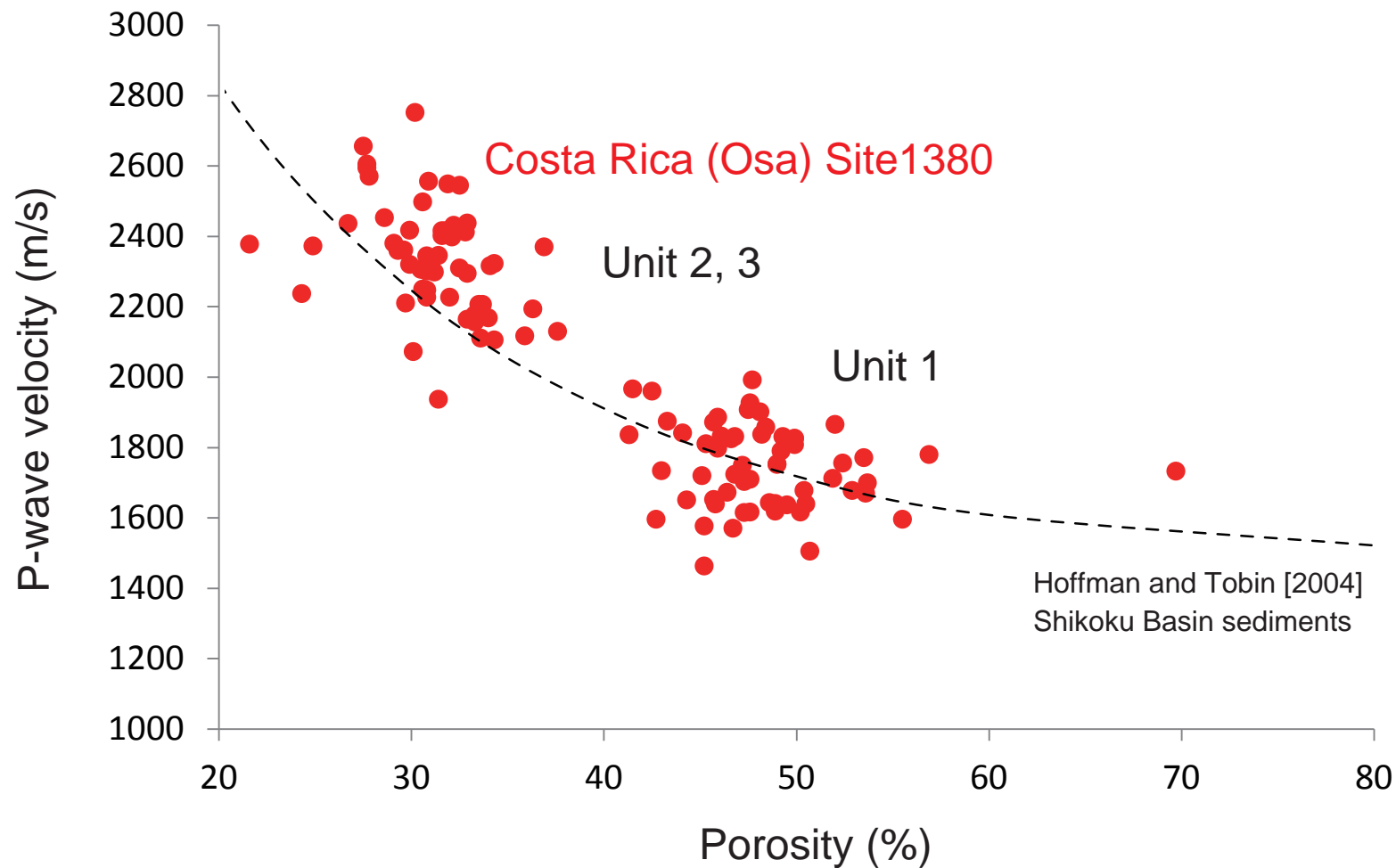


Figure 23. Cross-correlation between the shipboard discrete sample porosity and P-wave velocity measurements for sediments recovered from Site 1380. Dotted lines: the approximate curve derived from the Shikoku Basin sediments from Hoffman and Tobin (2004). It is notable that the overall trend is consistent among Units 1, 2, and 3. However, the properties of Units 2 and 3 are plotted above the approximate curve, indicating higher consolidation than Unit 1.

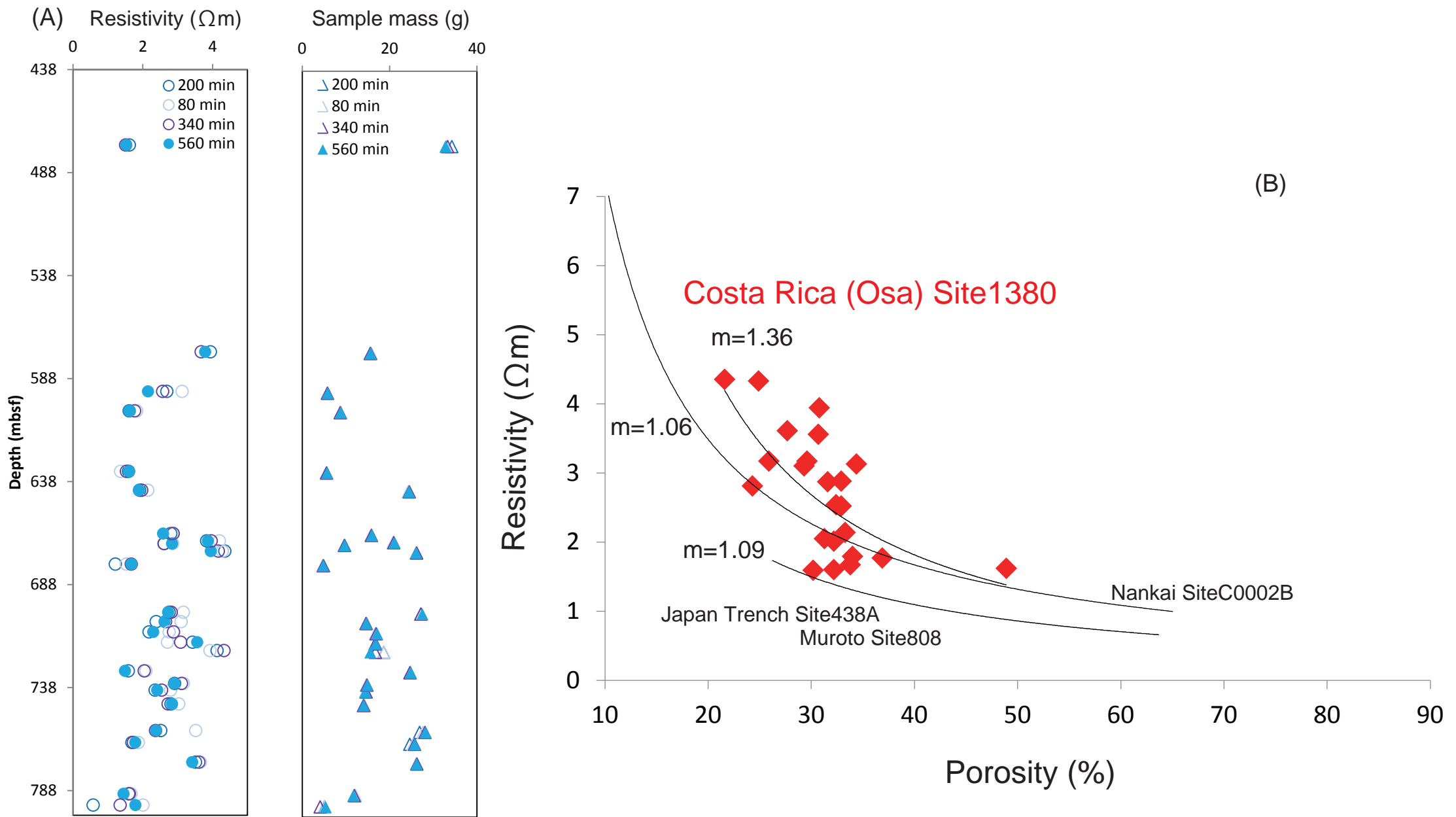


Figure 24. (A) Results of the resistivity measurements obtained from Site 1380 in this study. Plots represent values measured after each time lapse.

(B) Cross-correlation between shipboard porosity and measured resistivity in this study (red diamond). Black approximate line: the exponential curve of Archie's law with reference to the curves for the Japan Trench Site 438A (DSDP Leg 57) and Nankai Trough Muroto Site 808 (ODP Leg 196) and Kumano Site C0002B (IODP Exp. 315) (Shipboard Scientific party, 1980; Shipboard Scientific Party, 2002; Expedition 315 Scientists, 2009).

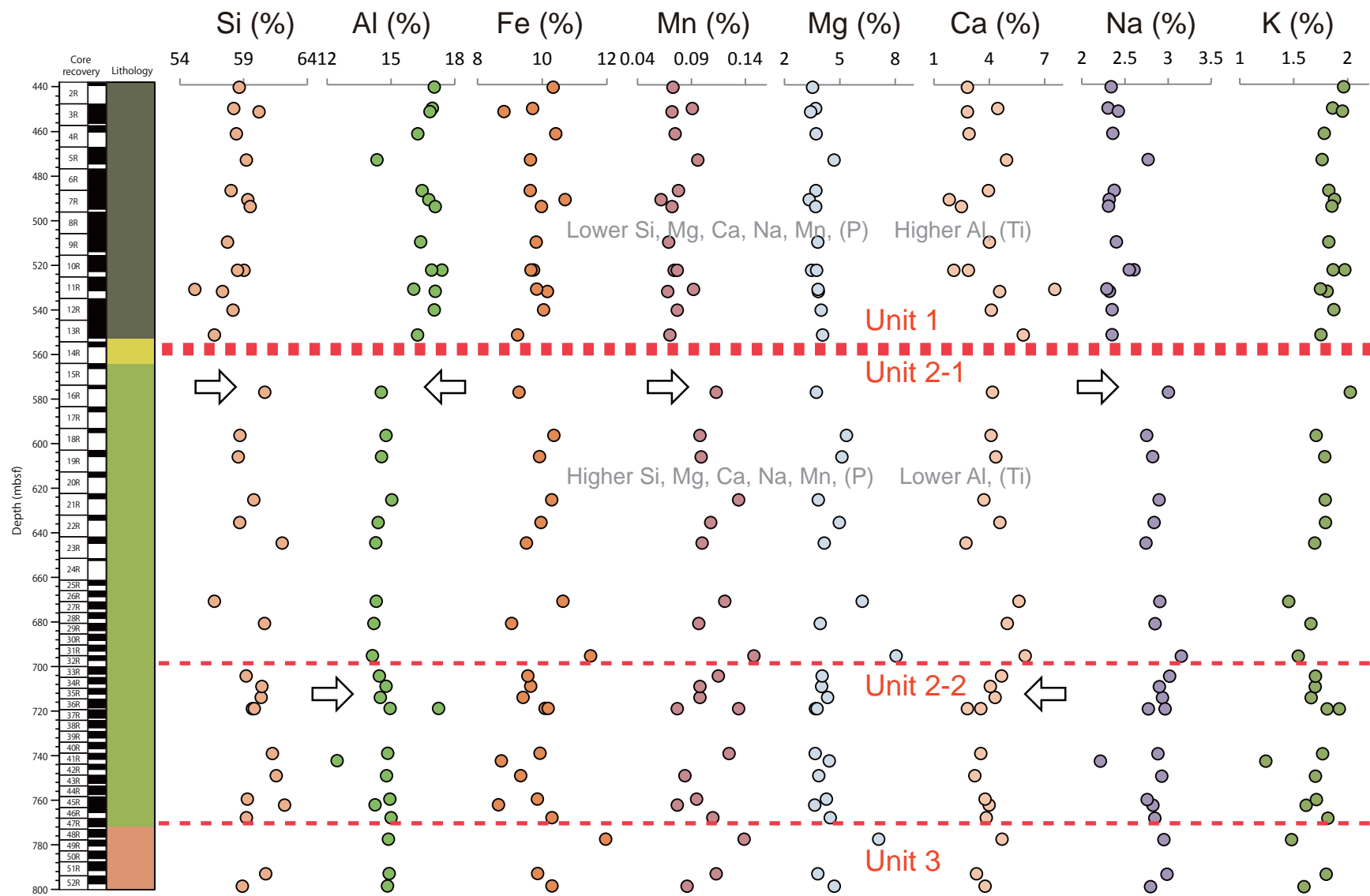


Figure 25. Major element (SiO_2 , Al_2O_3 , Fe_2O_3 , MnO , CaO , Na_2O , K_2O) weight percent (%) of sediment samples at Site 1380 obtained from the XRF analysis. Red dotted lines: lithostratigraphic unit boundaries and physical property transitions. Arrows mark the transition in element composition in which Al_2O_3 , K_2O , and TiO_2 concentrate in Unit 1 and SiO_2 , CaO , P_2O_5 , MgO , NaO , and MnO concentrate in Unit 2, though these differences in element composition are minimal.

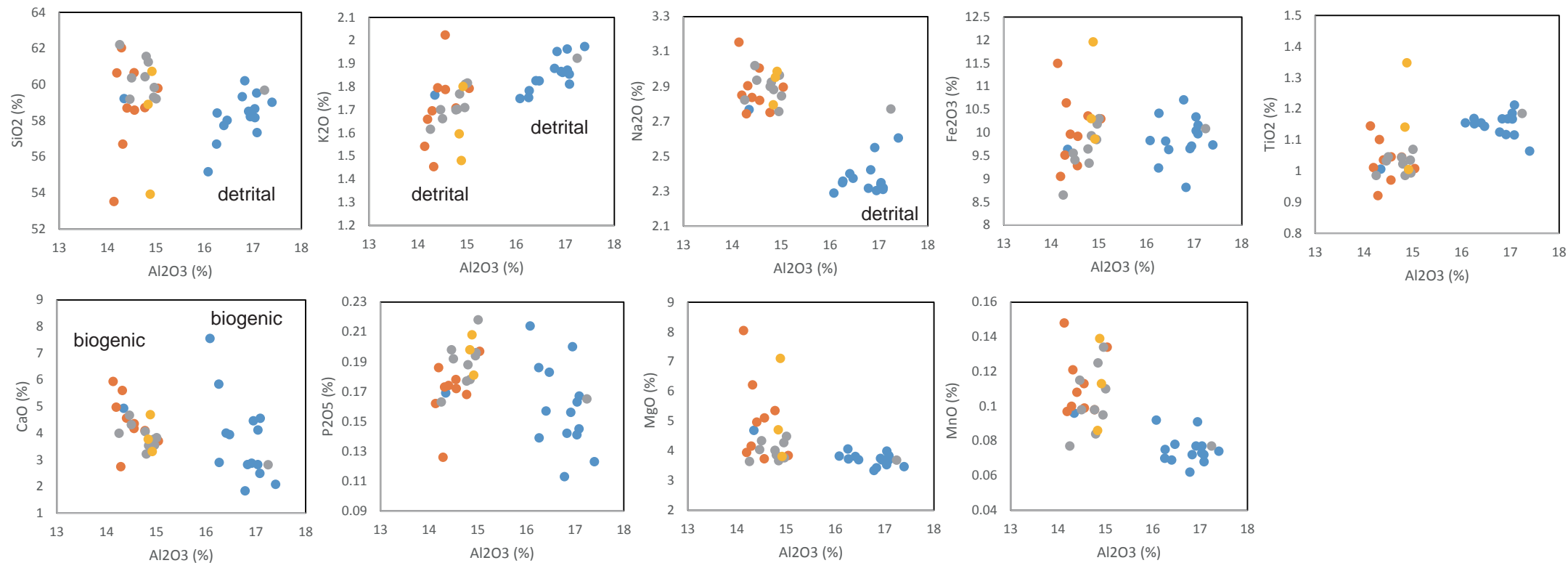


Figure 26. Cross-plots between Al₂O₃ and the other nine major elements (SiO₂, K₂O, Na₂O, Fe₂O₃, TiO₂, CaO, P₂O₅, MgO, MnO).

Positive correlations indicate elements that are contained in the detrital component, whereas negative correlations represent elements affected by biogenic or diagenetic components.

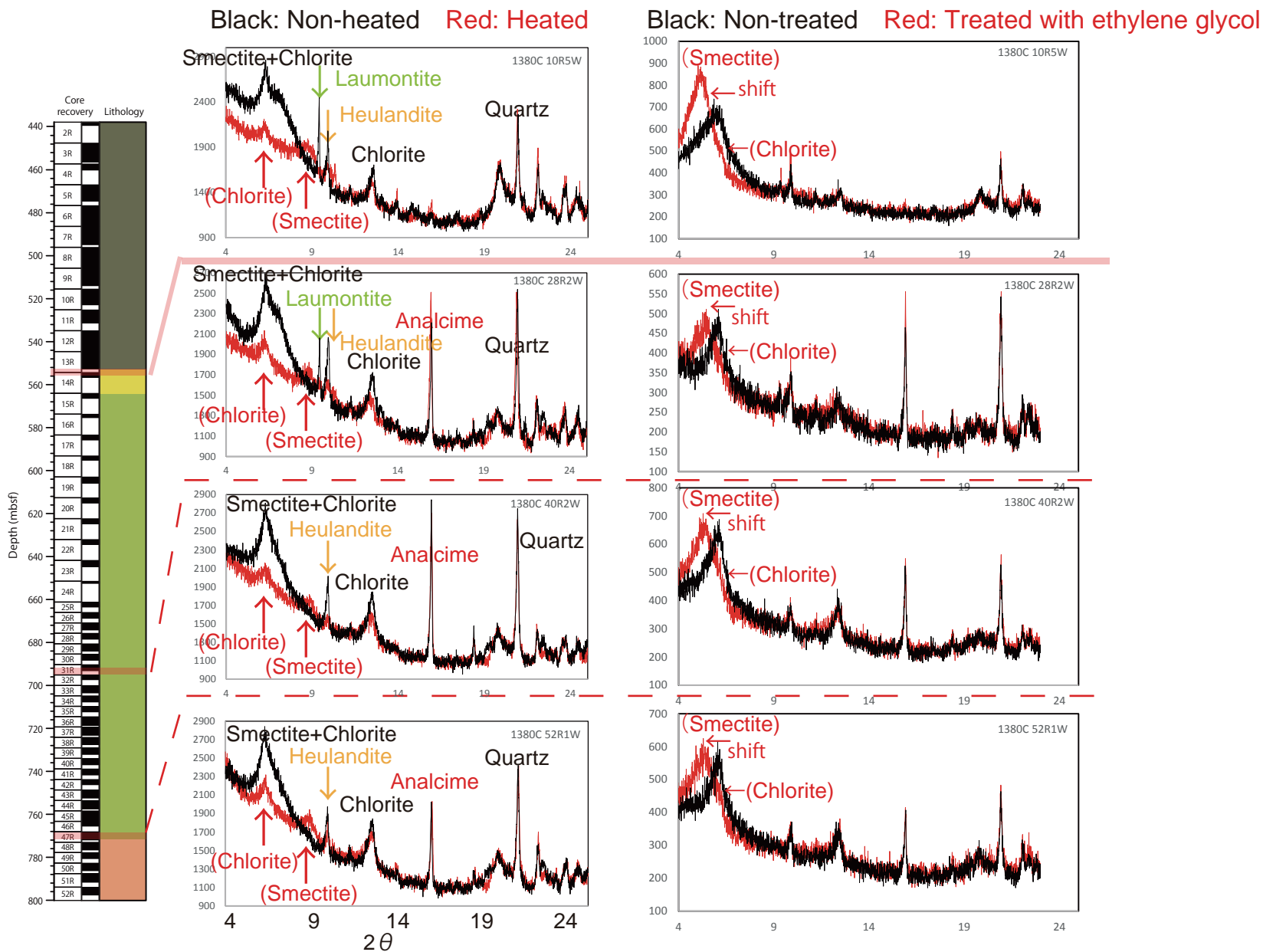
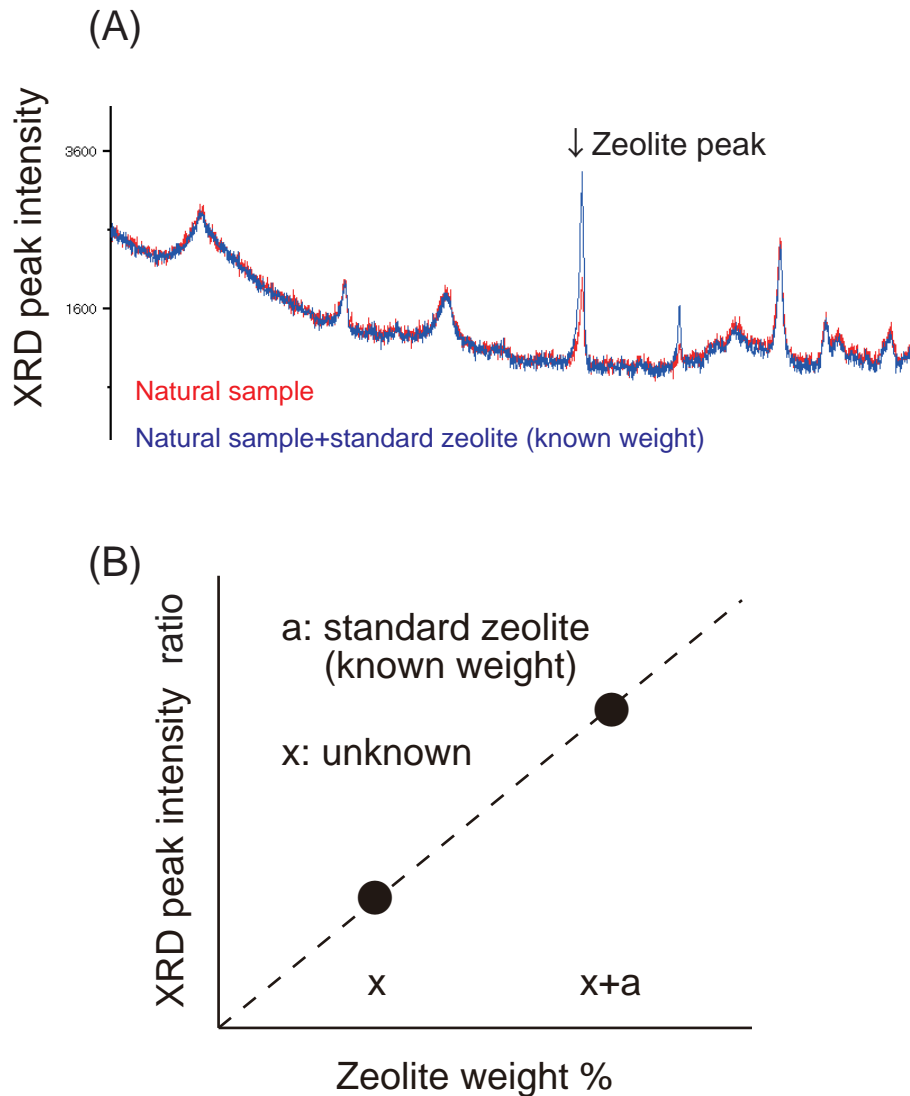


Figure 27. (Left) Representative bulk XRD results of sediment samples at Site 1380. Black lines: samples before heating. Red lines: measurements on the heated (350°C) samples. The two peaks at 9.91° and $11.18^\circ 2\theta$ were identified as laumontite and heulandite, respectively since they disappeared when heated. The peak at $6.28^\circ 2\theta$ is considered as a mixed layer of smectite and chlorite since the peak did not disappear when heated, indicating the presence of chlorite, and smectite has shifted to $8.92^\circ 2\theta$. (Right) Red lines: samples treated with ethylene glycol. Black lines: non-treated measurements. Smectite has higher expandability after ethylene-glycol treatment in Unit 1 compared to Units 2 and 3 indicating that pure smectite is more abundant in Unit 1.



(C)

Zeolite quantification (weight %)

Sample	Analcime	Laumontite	Heulandite		Porosity decrease due to laumontite and heulandite
Unit 1		Zeolites that decrease porosity			
1380C 5R4W	--%	3.2%	1.1%	=4.3%	3.6%
1380C 10R5W	--%	4.5%	1.0%	=5.5%	4.7%
Unit 2-1					
1380C 28R2W	6.1%	2.2%	1.6%	=9.9%	3.6%
Unit 2-2					
1380C 40R2W	7.2%	--%	1.2%	=8.4%	1.2%
Unit 3					
1380C 52R1W	7.9%	--%	1.2%	=9.1%	1.1%

Figure 28. (A) XRD measurements of natural samples and samples with added standard zeolites of known weight (analcime, heulandite, laumontite) for the zeolite mineral weight % quantification. **(B)** The weight % of zeolite is obtained from the relationship with the XRD peak intensity ratio of the natural samples and the standard-added samples. **(C)** The zeolite weight % results and calculated porosity decrease due to the zeolite. The effect of fluid-interacted zeolite precipitation (laumontite and heulandite) on porosity needs to be accounted for, if the fluid-sediment interaction occurred after burial and if the zeolite precipitation affected the initial compaction curve (Fig. 31).

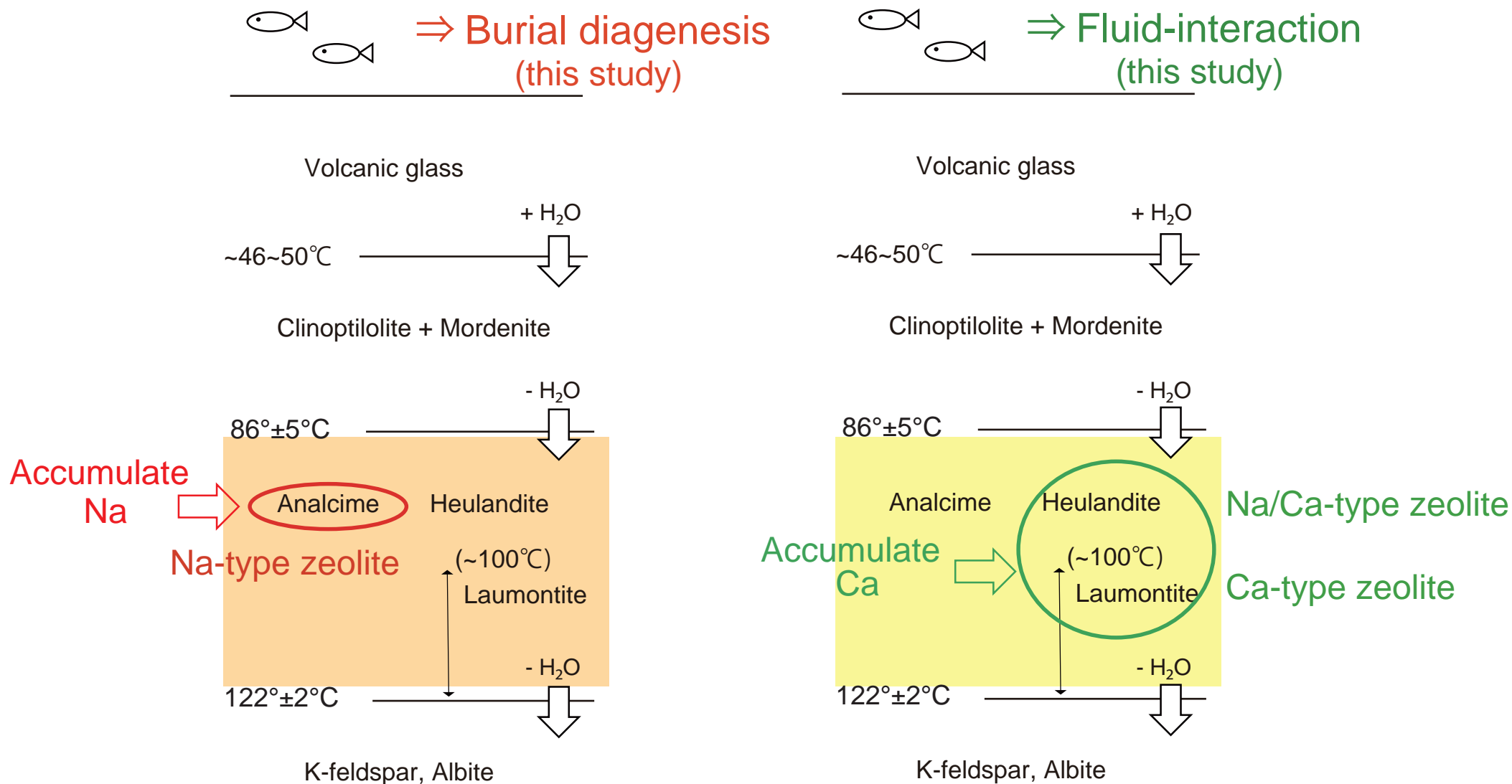


Figure 29. Schematic image of the general vertical zonal distribution of unaltered glass, zeolite, and authigenic feldspar attributed to a geothermal gradient during burial diagenesis and/or hydrothermal alteration. Na-type zeolite analcime, Na/Ca-type zeolite heulandite, and Ca-type zeolite laumontite are formed as intermediate minerals. The reaction between volcanic glass to clinoptilolite and mordenite are known to occur at >~50°C, and clinoptilolite and mordenite transform to analcime and heulandite between 86°±5°C and 122°±2°C, whereas laumontite can be formed at >~100°C, and at >122°±2°C analcime changes to albite (e.g., Iijima, 1986; Ogiwara, 1996). Na-type zeolite analcime and Na/Ca- and Ca-type zeolites heulandite and laumontite are likely to originate from different source and/or form through different fluid-interaction accumulating Na and Ca, respectively.

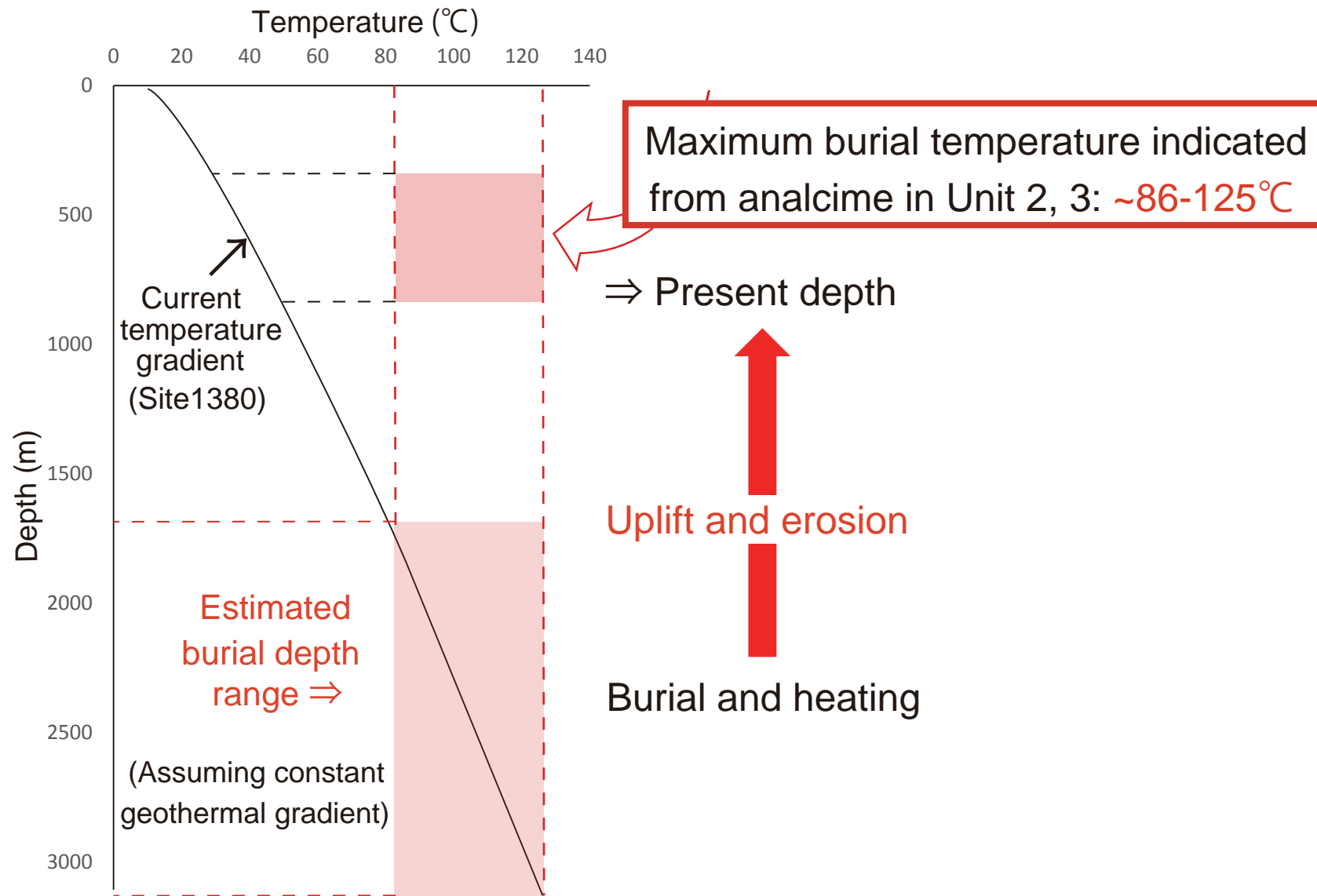


Figure 30. The temperature gradient of the sediments at Site 1380 obtained from the shipboard thermal conductivity and temperature measurements (Fig. 17), assuming a constant heat flow value. Upper red square: the experienced temperature range of the sediments at the present depth. Lower red square: the estimated maximum burial depth range. The high-temperature range derived from the analcime diagenesis indicates exhumation from greater depth through uplift and erosion.

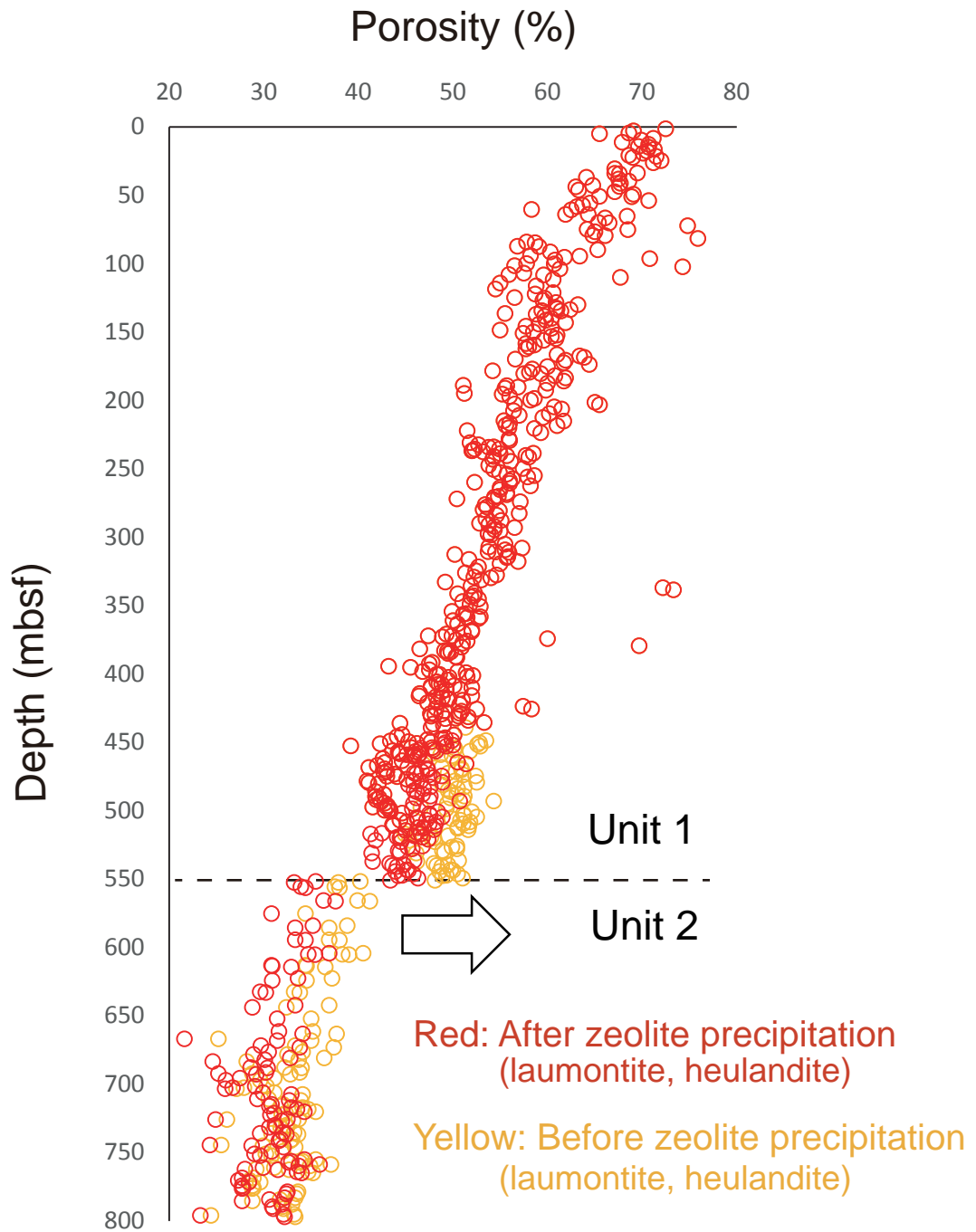
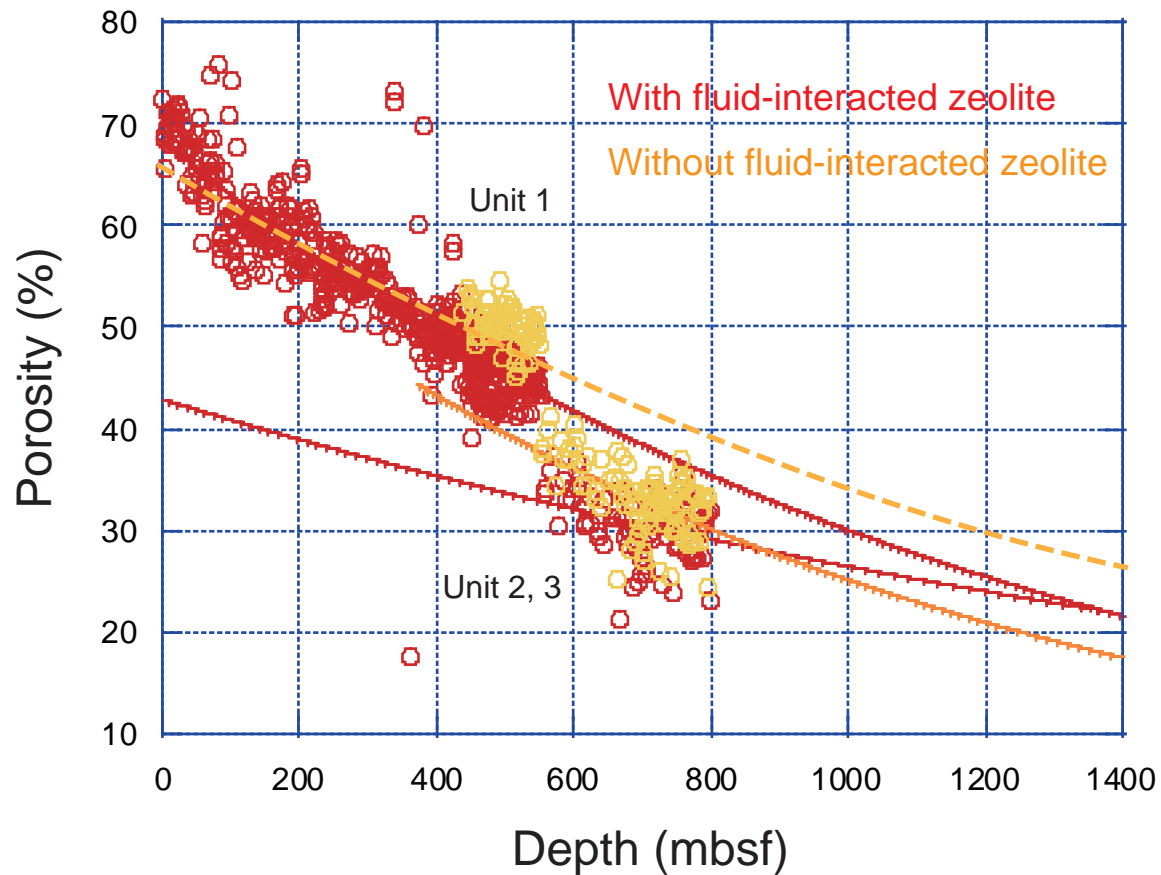


Figure 31. Porosity-depth transition of the sediments at Site 1380. Red plots: the shipboard porosity data of natural samples that include zeolite precipitation. Yellow plots: the recalculated porosity data eliminating the effect of zeolites due to fluid interaction (laumontite and heulandite) in this study. Black dotted line: location of the unconformity between Unit 1 and Unit 2.



<Unit 1>

— $y = 68.322 * e^{(-0.00082278x)}$ $R = 0.89379$

- - - $y = 66.437 * e^{(-0.0006548x)}$ $R = 0.83178$

<Unit 2, 3>

— $y = 43.08 * e^{(-0.00047865x)}$ $R = 0.33658$

— $y = 62.224 * e^{(-0.00090551x)}$ $R = 0.60262$

Figure 32. Porosity-depth curve of Site 1380 Unit 1, 2, and 3 sediments and approximate curves. Red plots: the shipboard porosity values including fluid-interacted zeolites (laumontite and heulandite). Yellow plots: the recalculated values without these zeolites. The equations and R values for each approximate curve are shown below. The red plots consider the fluid-sediment interaction to have occurred before burial, and the yellow plots consider the fluid-sediment interaction to have occurred after burial. The consolidation trends of the sediments are consistent, and the porosity-depth curve of Unit 1 can be assumed to represent the compaction curve of the sediments throughout the depth (Units1-3).

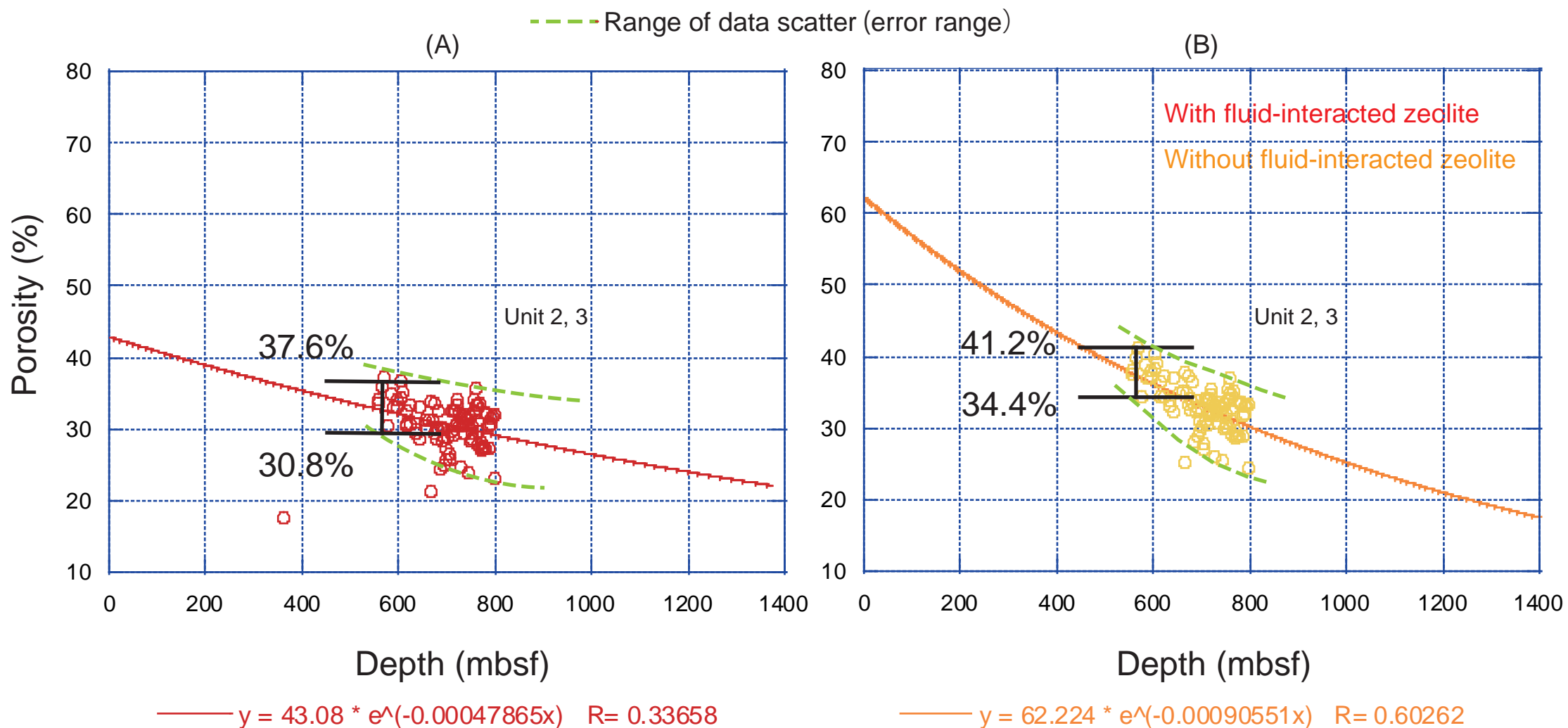


Figure 33. Porosity-depth plots for Site 1380 Unit 2 and 3 sediments. Red plots: the shipboard porosity values including fluid-interacted zeolites (laumontite and heulandite). Yellow plots: the recalculated values without these zeolites. The equations and R values for each approximate curve are shown below. Green dotted lines: the range of data scatter (error range). The porosity range below the unconformity is considered based on the minimum and maximum values between the range of data scatter. (A) The porosity range including fluid-interacted zeolite (laumontite and heulandite) is 30.8%–37.6%. (B) The porosity range without fluid-interacted zeolite is 34.4%–41.2%.

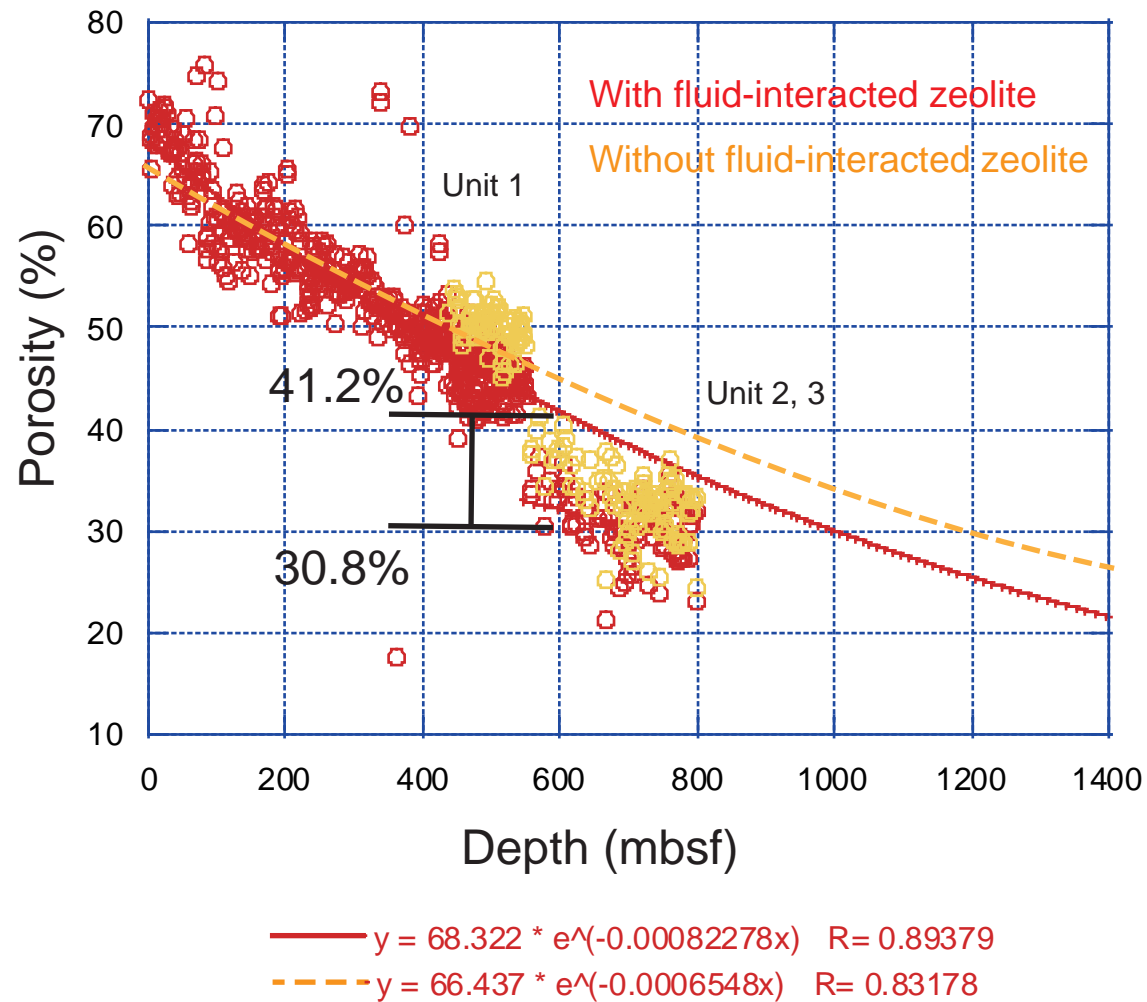


Figure 34. The maximum burial depth below the unconformity can be obtained from the depth along the porosity-depth curve of Unit 1 that coincides with the porosity range below the unconformity (i.e., 30.8%–41.2%) (black bar) examined from Fig. 33. Red plots: the shipboard porosity values including fluid-interacted zeolites (laumontite and heulandite). Yellow plots: the recalculated values without these zeolites. The equations and R values for each approximate curve are shown below.

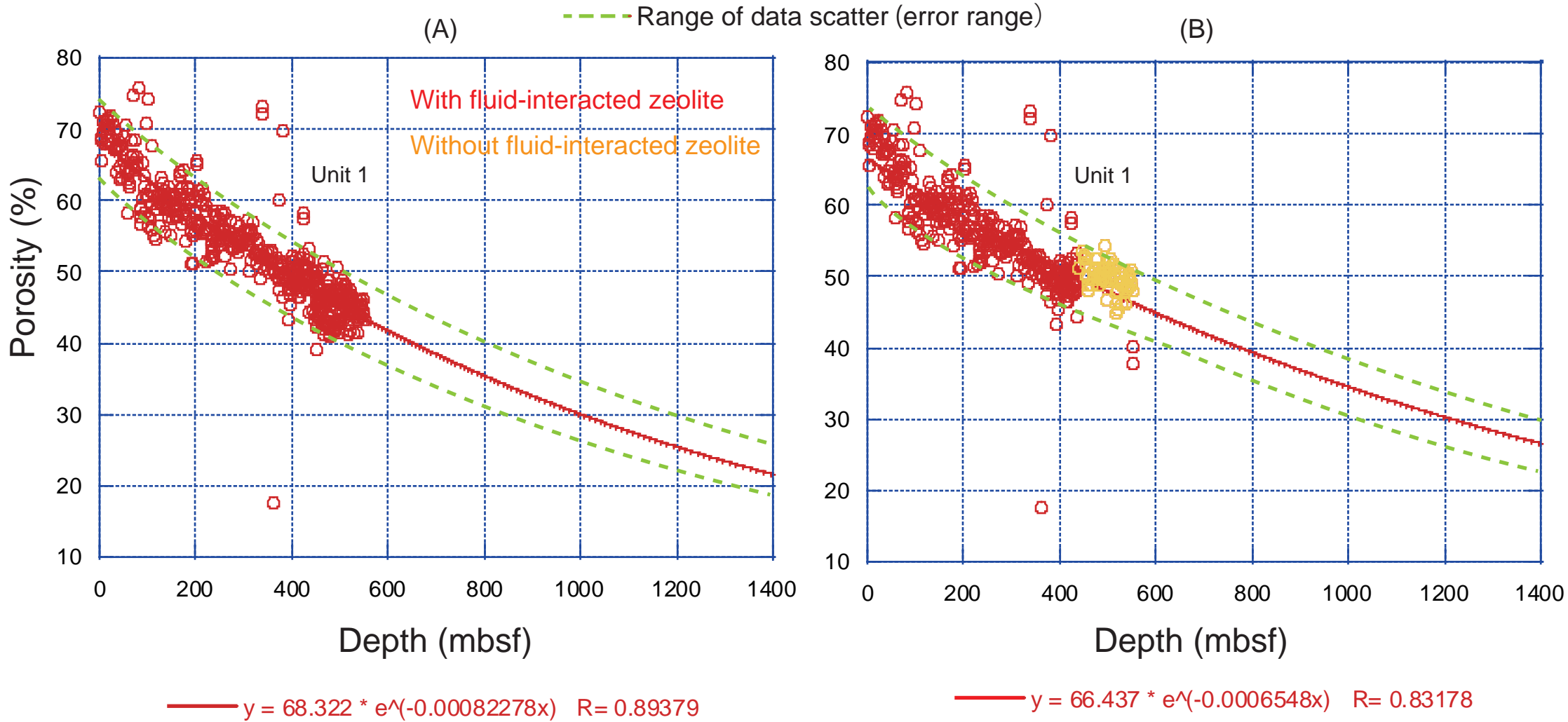


Figure 35. The range of data scatter (error range) along the approximate curve is predicted from the porosity range of Unit 1 (green dotted line). (A) Approximate curve including fluid-interacted zeolite (laumontite and heulandite). (B) Approximate curve without fluid-interacted zeolite. Red plots: the shipboard porosity values including fluid-interacted zeolites (laumontite and heulandite). Yellow plots: the recalculated values without these zeolites. The equations and R values for each approximate curve are shown below.

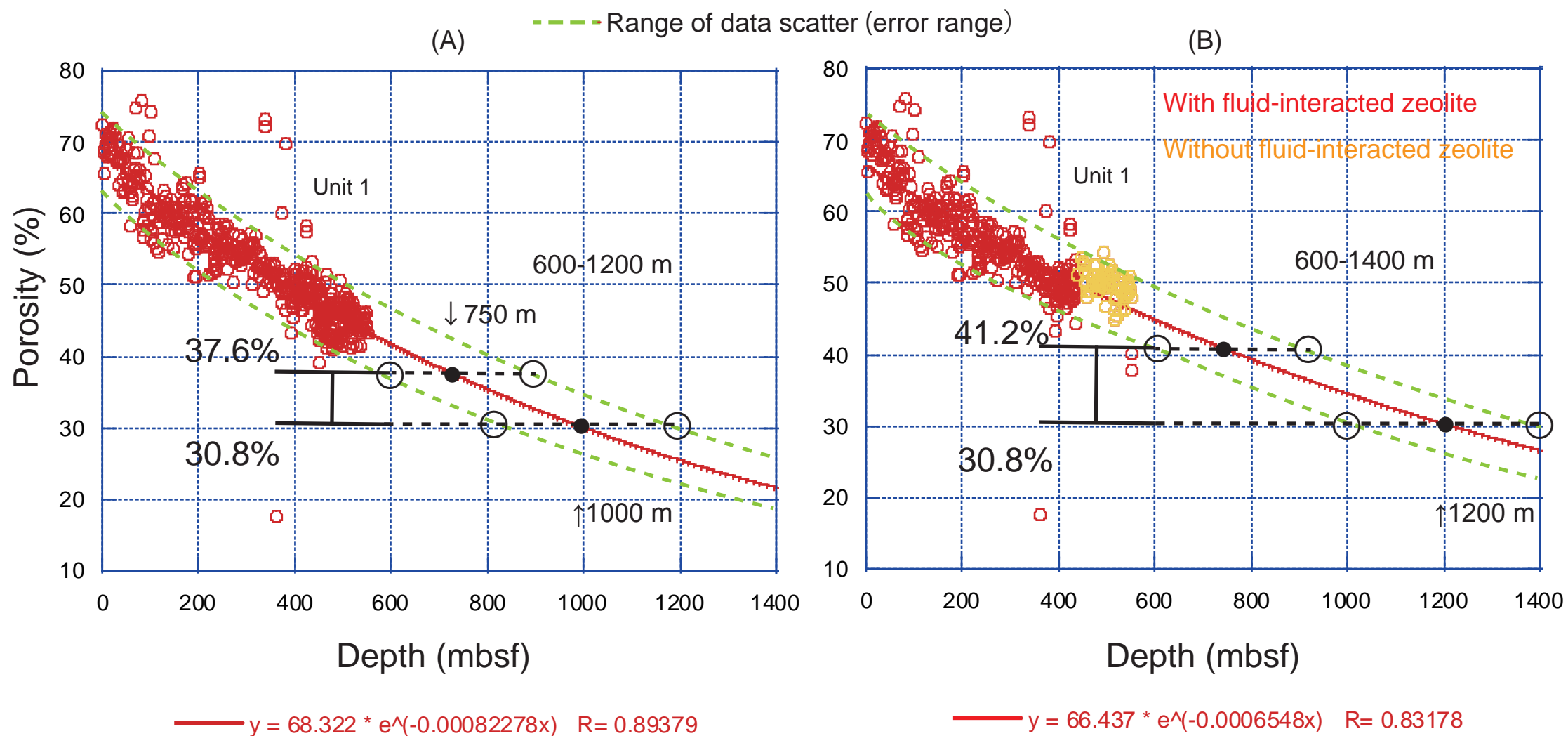


Figure 36. The maximum burial depth below the unconformity can be obtained from the depth range (approximate curve and range of data scatter) along the porosity-depth curve (Fig. 35) of Unit 1 that coincides with the porosity range below the unconformity examined from Fig. 33. The maximum burial depth ranges (A) 600–1200 m from the approximate curve including fluid-interacted zeolites (laumontite and heulandite), and (B) 600–1400 m from the approximate curve without fluid-interacted zeolites. Red plots: the shipboard porosity values including fluid-interacted zeolites (laumontite and heulandite). Yellow plots: the recalculated values without these zeolites. The equations and R values for each approximate curve are shown below.

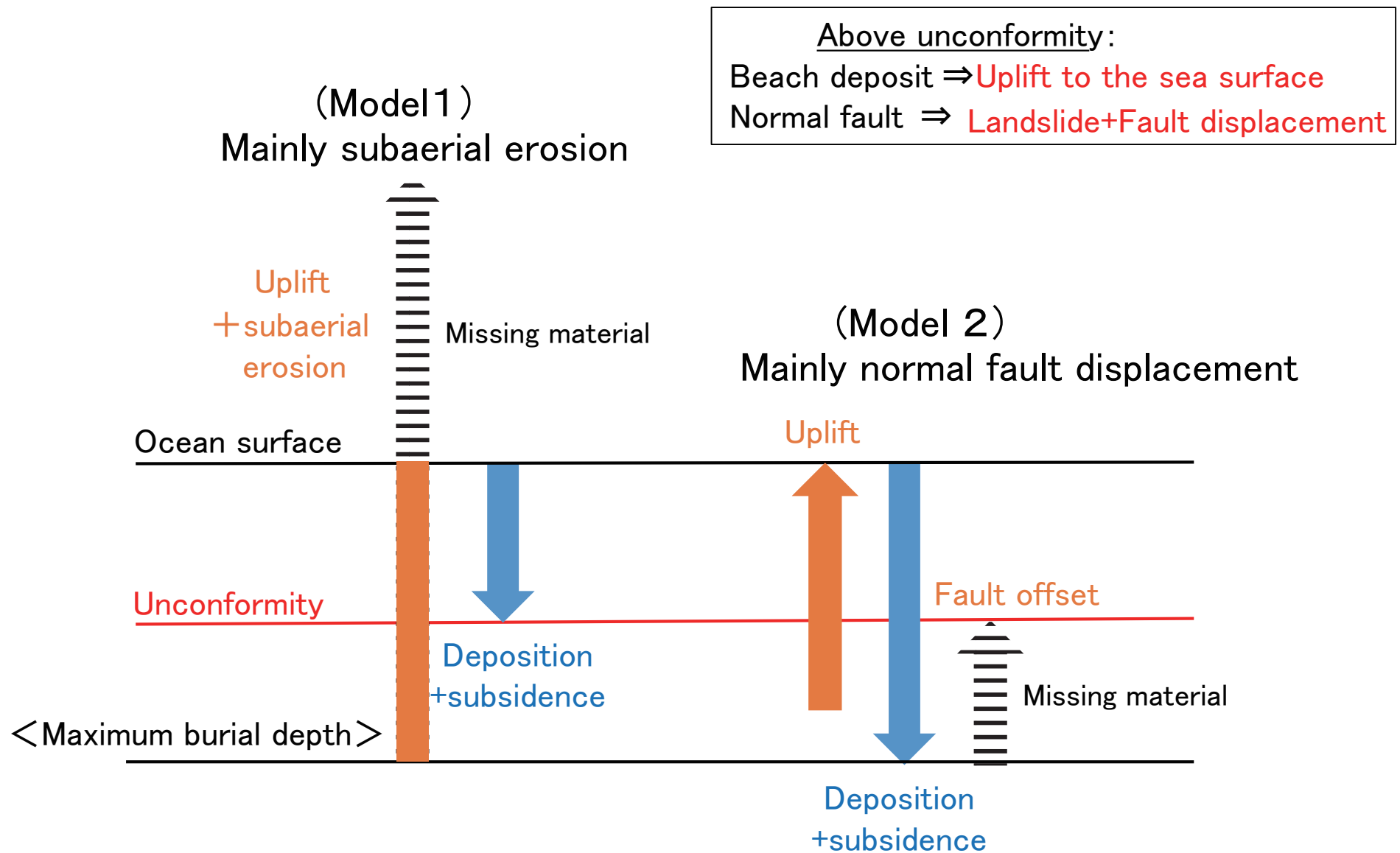


Figure 37. The sediments below the unconformity are likely to have undergone uplift, subaerial erosion, and/or normal faulting to reach the current depth of the unconformity. Beach deposits above the unconformity indicate uplift events to the sea surface, whereas normal faults indicate landslide and fault displacement. In this study, two scenarios are considered; Model 1 is the case of maximum uplift and subaerial erosion, and Model 2 is the case of minimum uplift and erosion and maximum normal fault displacement. Uplift is followed by deposition and subsidence.

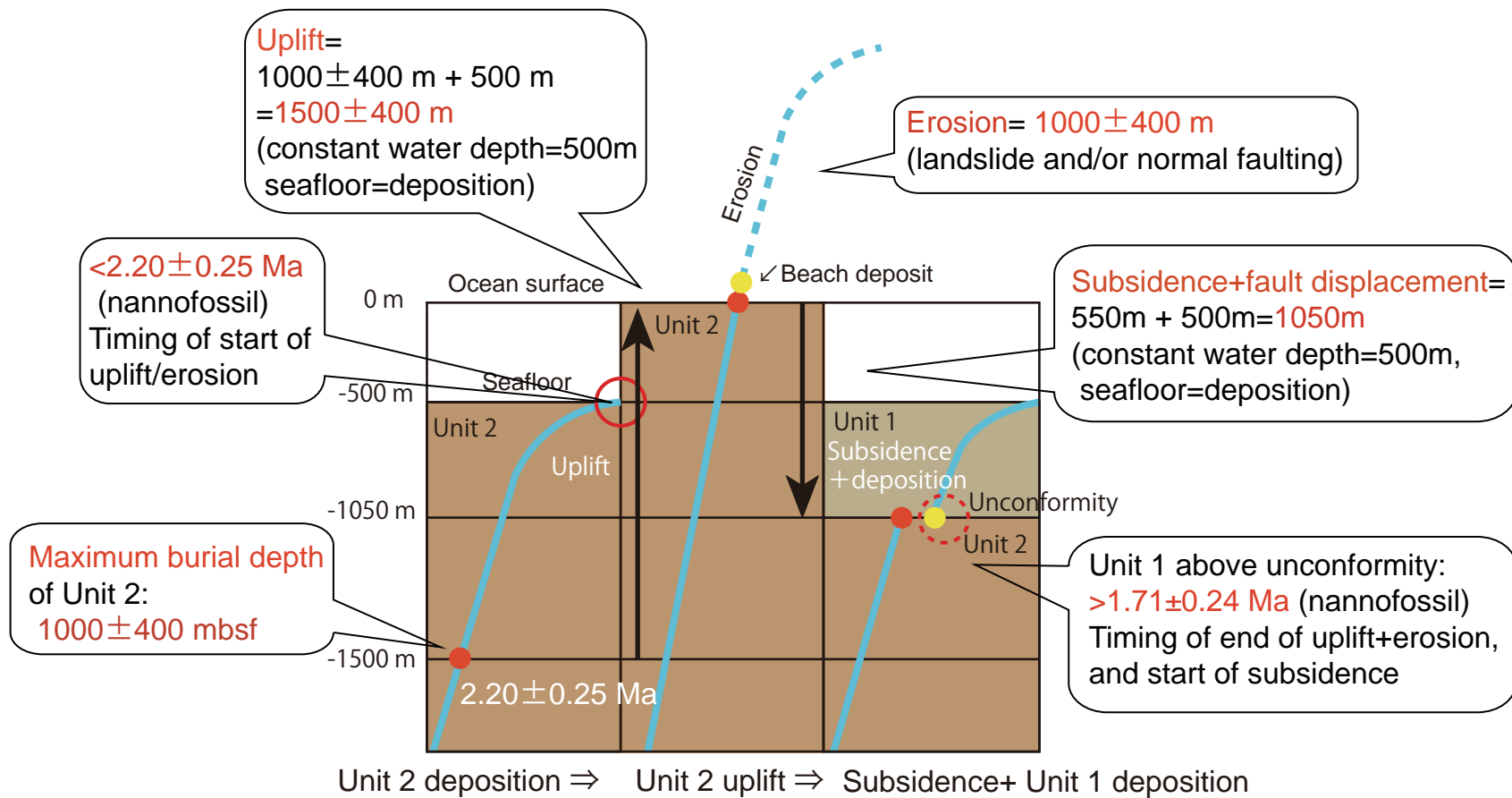


Figure 38. Interpretation of rapid, maximum uplift and material removal derived from the porosity-depth transition (Model 1). The uplift and surface erosion at the sea surface of Unit 2 are followed by subsidence and the deposition of Unit 1. Brown box: sediment column. White box: seawater. Blue-curved line: the porosity-depth curve. Red dot: the top of the sediments of Unit 2 just below the present unconformity. Yellow dot: beach deposit.

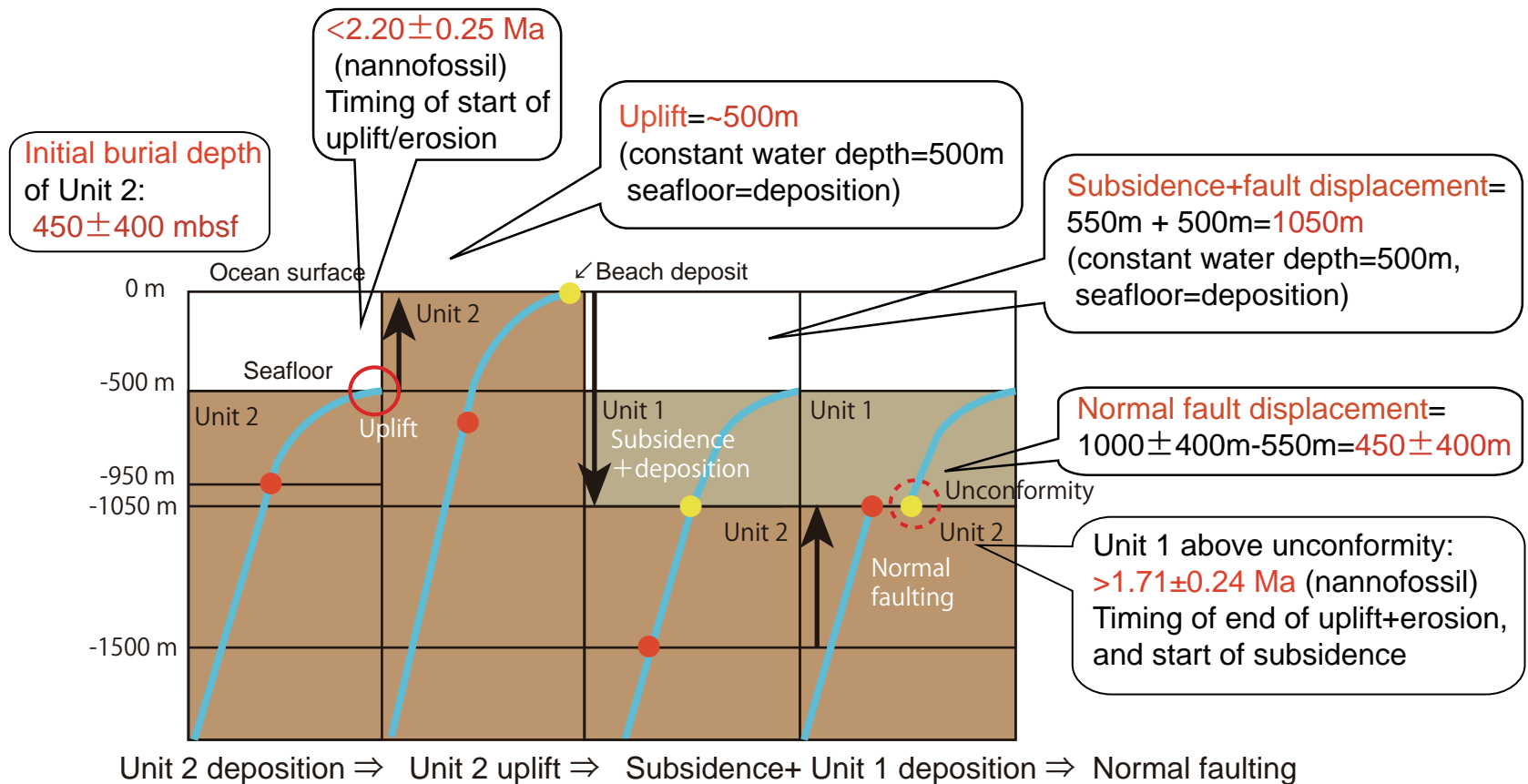


Figure 39. Interpretation of the minimum uplift and material removal, and maximum normal faulting derived from the porosity-depth transition (Model 2). The uplift to the sea surface of Unit 2 is followed by subsidence and the deposition of Unit 1, and normal faulting between Units 1 and 2. Brown box: the sediment column. White box: seawater. Blue-curved line: the porosity-depth curve. Red dot: the top of the sediments of Unit 2 just below the present unconformity. Yellow dot: beach deposit.

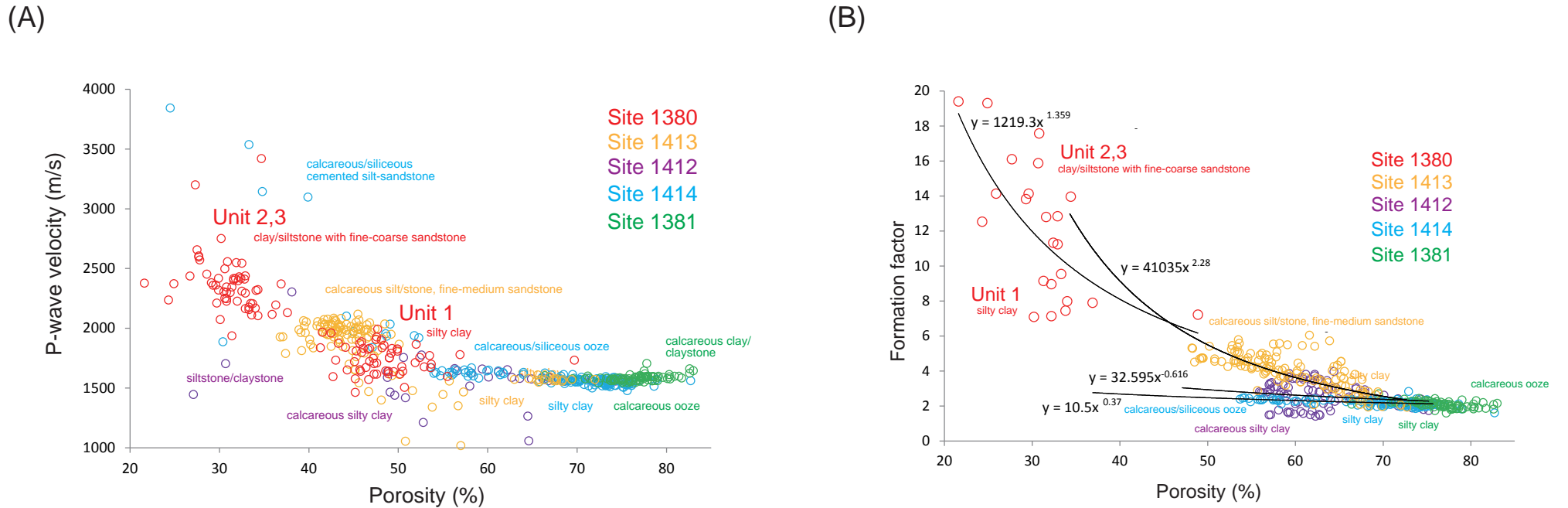


Figure 40. Cross-plots between shipboard discrete sample porosity and P-wave velocity (A), and porosity and formation factor (B) of sediments at mid-slope Site 1380, upper-slope Site 1413, toe Site 1412, and reference Sites 1414 and 1381. Black approximate line: the exponential curve of Archie' s law. The lithology of the sediments is described next to each plot.

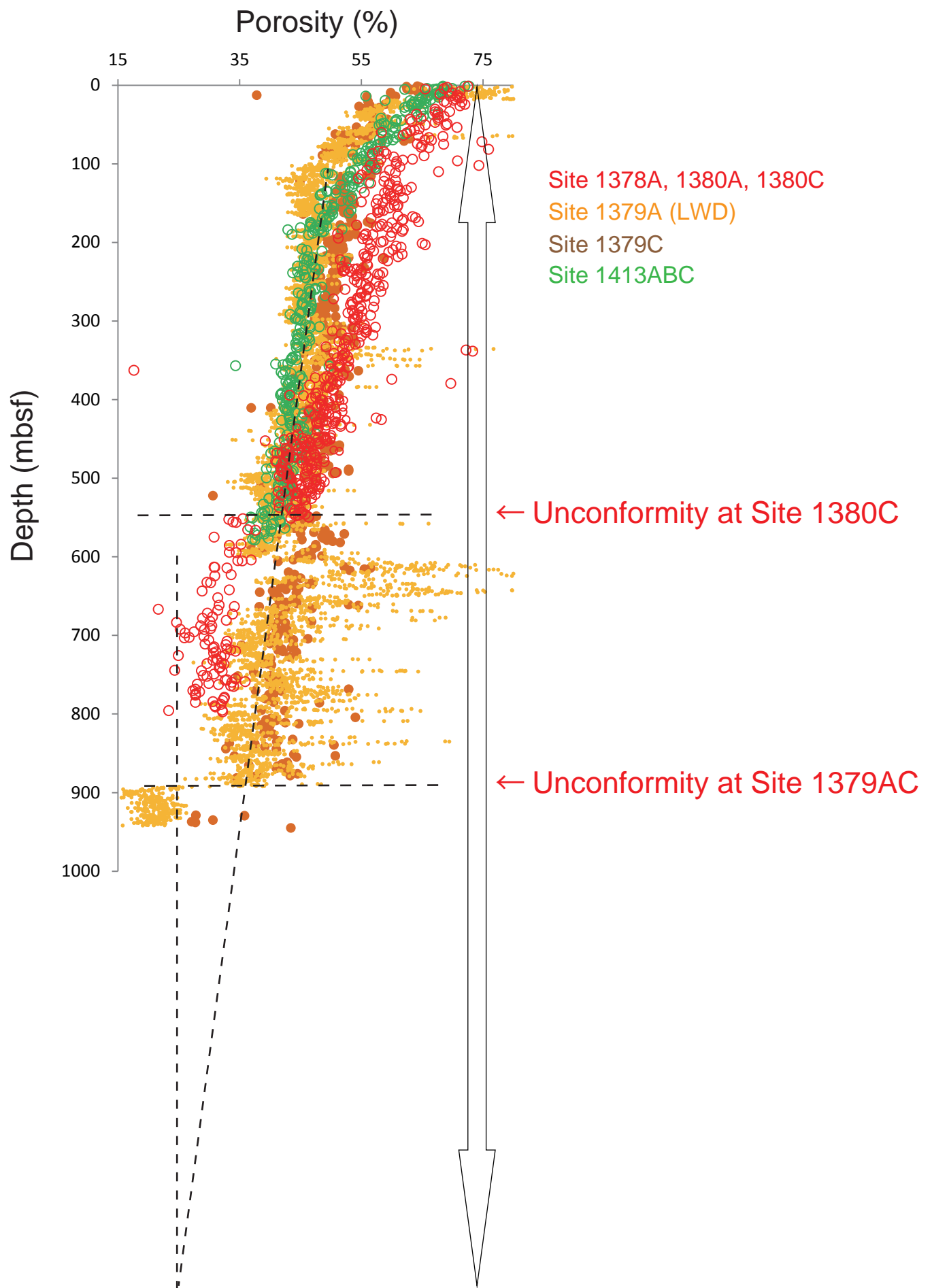


Figure 41. Shipboard porosity-depth curve of sediments from middle-slope Site 1380 and upper-slope Sites 1379 and 1413 obtained from discrete samples and logging-while-drilling measurements (Harris et al., 2013; Vannucchi et al., 2012). Black horizontal dotted lines: the depths of the unconformity that correlate with the major seismic reflectors at Sites 1380 and 1379. The composite porosity depth curve across the unconformity enabled the estimation of the amount of sediment removal and offset, which is larger at Site 1379 compared to Site 1380.

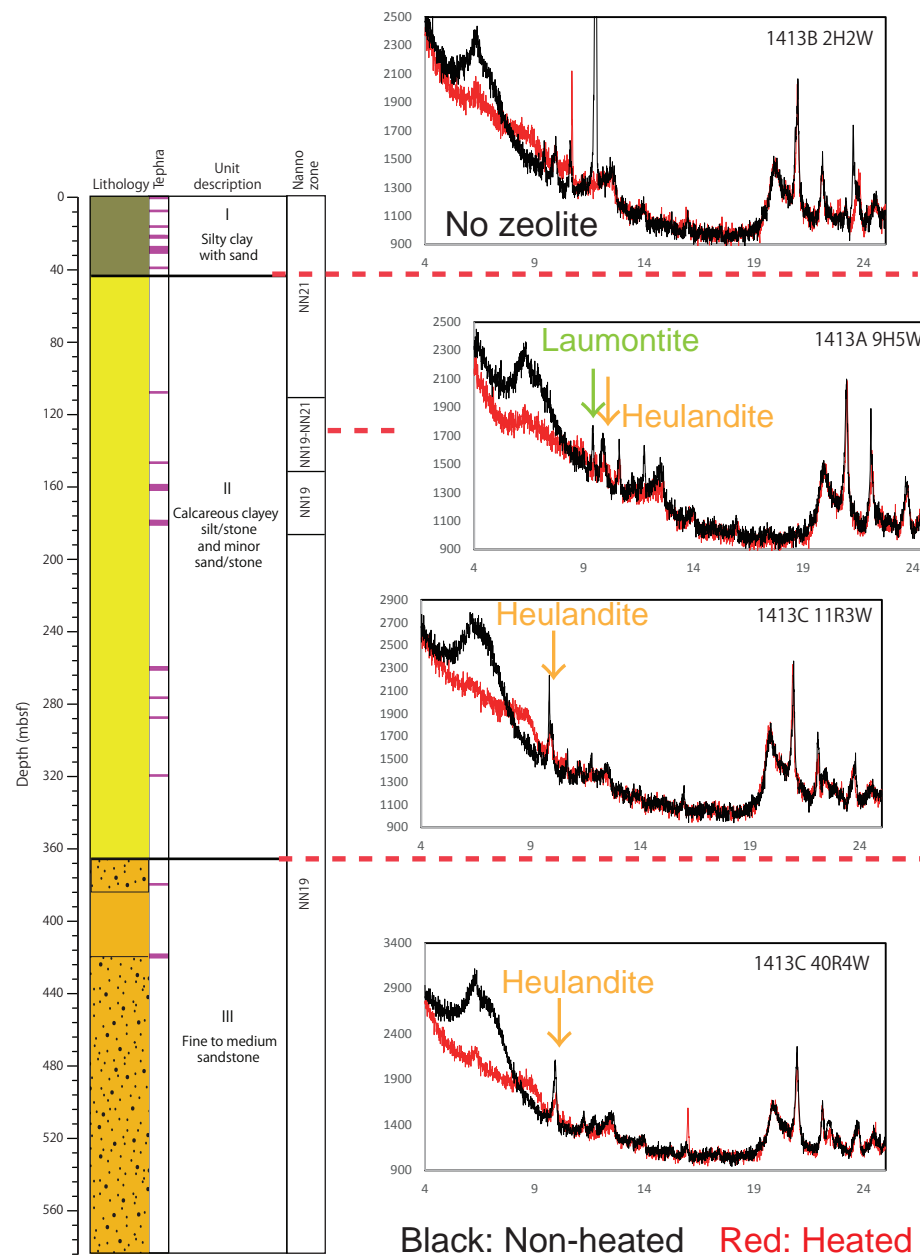


Figure 42. Lithostratigraphic summary of upper slope Site 1413 from Harris et al. (2013) and results of the bulk XRD analysis of representative sediment samples conducted in this study. The major mineral components are phyllosilicates including smectite and chlorite, plagioclase, quartz, and calcite. Zeolites are not present in lithostratigraphic Unit 1, whereas they are present in Units 2 and 3, consisting mainly of heulandite and containing laumontite at the interval between 40 and 130 mbsf. Black lines:samples before heating. Red lines: measurements of the heated (350°C) samples. Red dotted lines: lithostratigraphic unit boundaries.

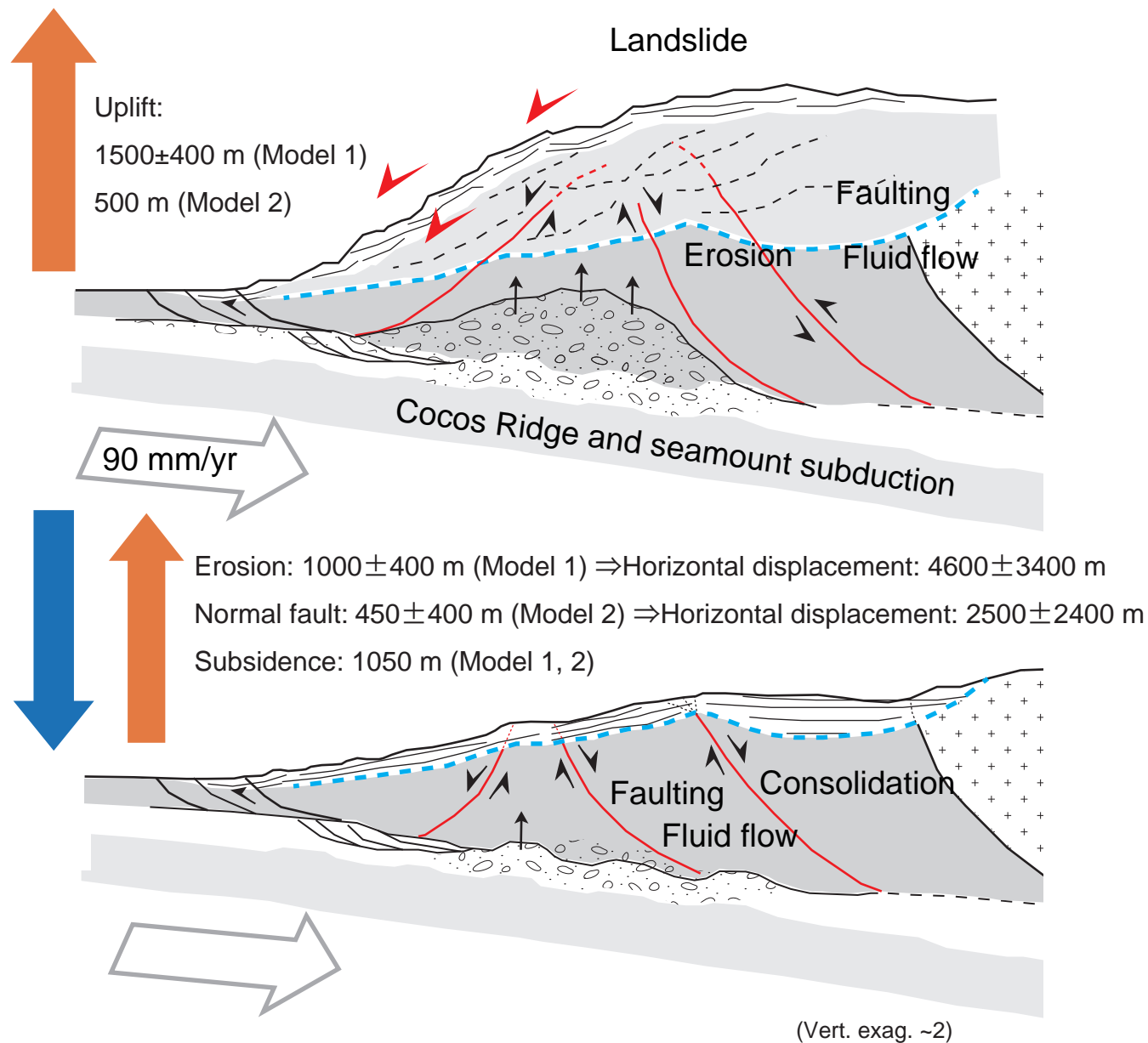


Figure 43. Schematic cartoon of the upper plate deformation history evaluated in Models 1 and 2 in this study. Uplift of maximum 1500±400 m (Model 1) and minimum 500 m (Model 2) and surface erosion of maximum 1000±400 m (Model 1) occurred between 2.20±0.25 and 1.71±0.24 Ma during the onset of the Cocos Ridge subduction, followed by subsidence of 1050 m and normal faulting of maximum 450±400-m-thick displacement (Model 2). Horizontal displacement was estimated under the slope/fault dip angle: 10°–30°. The forearc wedge is characterized by a variable wedge taper angle and high consolidation due to the exhumation of deep sediments through surface erosion and/or extension (faulting, fluid flow).

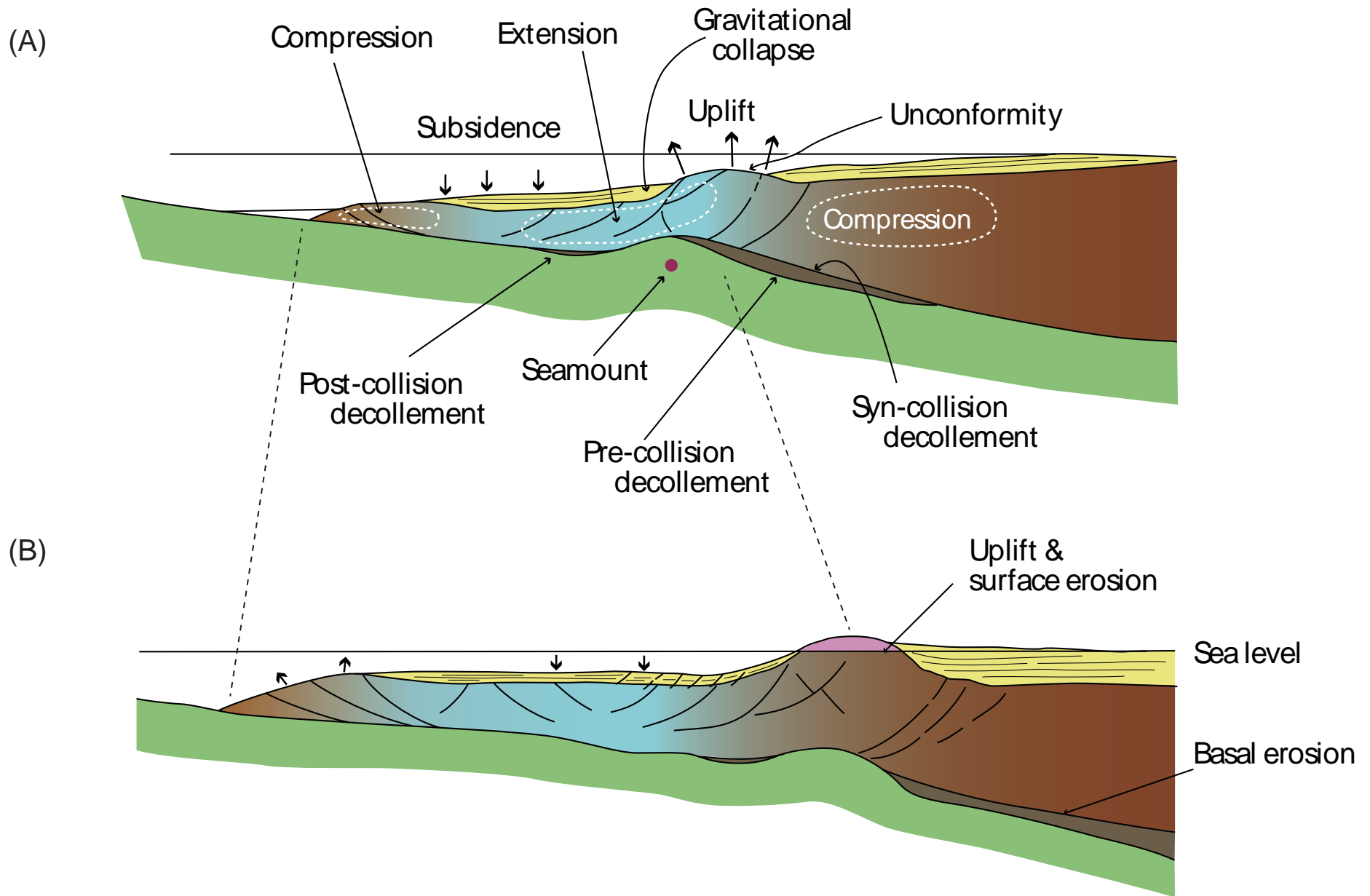
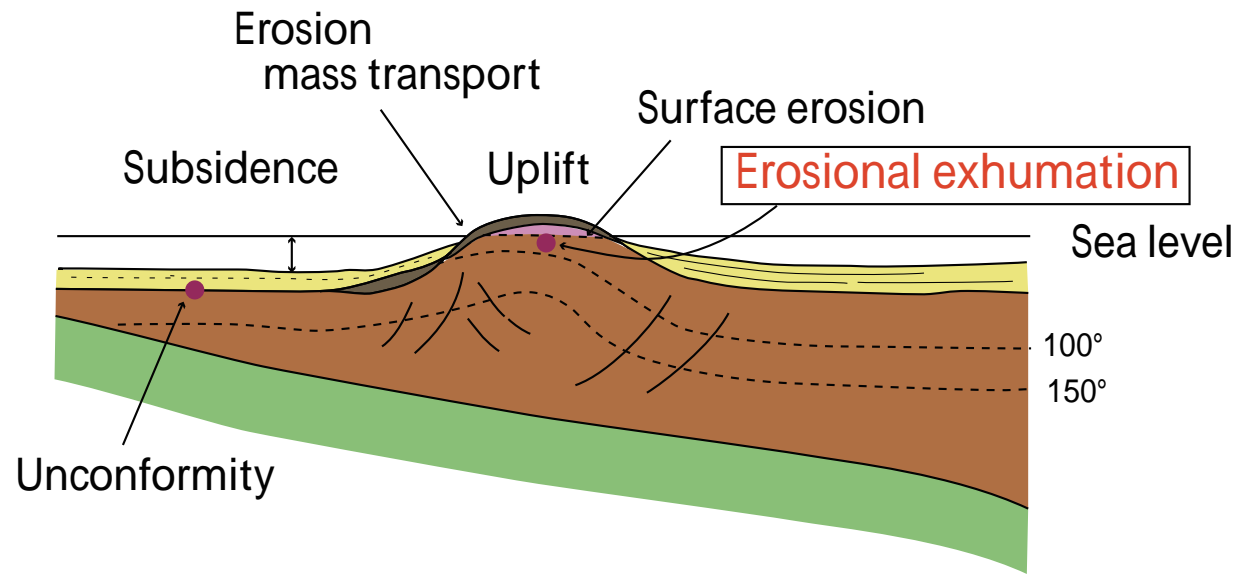


Figure 44. Schematic cartoon of the upper plate deformation and the response during seamount/ridge subduction quantified in this study. (A) Significant uplift is caused by the subducting bathymetric high, followed by subsidence and extension along the post-collision decollement, and compression in the wake of the seamount. (B) The upper plate is subjected to uplift and surface erosion, and it undergoes vast subsidence along the track of the seamount through normal faulting.

Model 1



Model 2

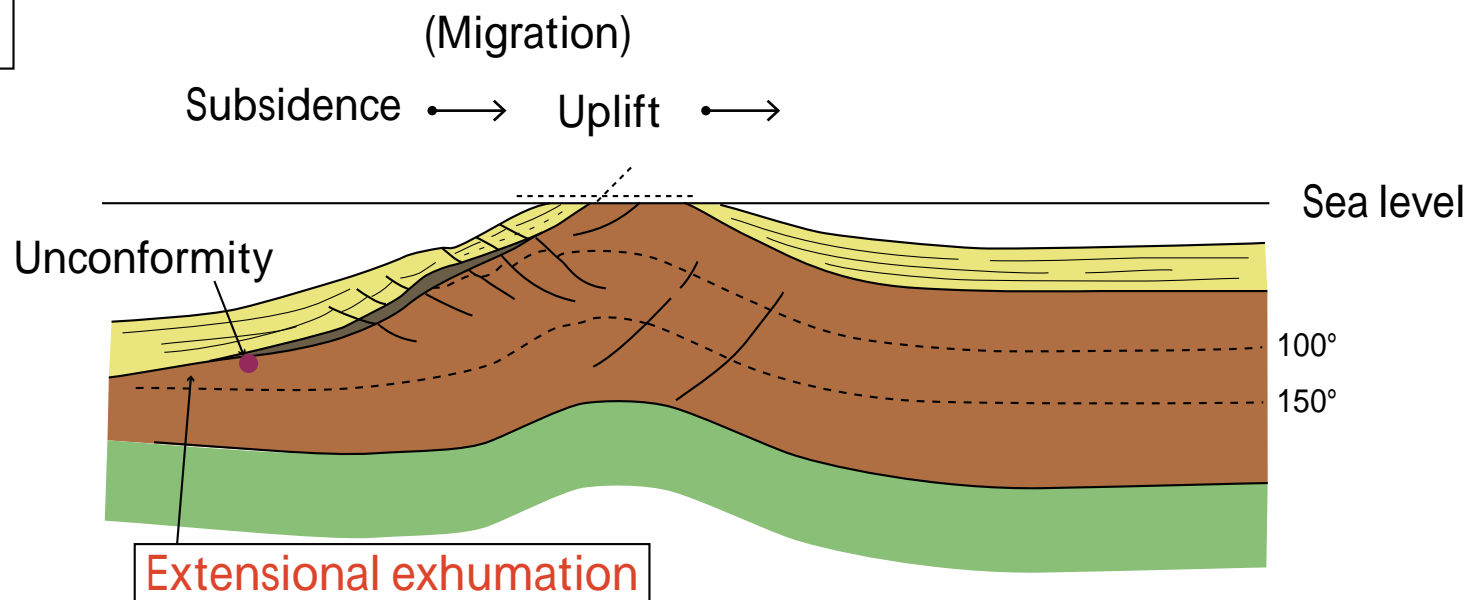


Figure 45. Schematic cartoon of the two models of the upper plate deformation during seamount subduction observed and quantified in this study. Model 1: The forearc may uplift and exhume above the sea-level, creating significant surface erosion. Rocks from greater depths and a higher paleo-isotherm are exhumed through erosion. Model 2: Alternatively, the forearc may uplift but not exhume significantly above sea level. Here, deeper rocks could still be exhumed through extensional faulting and gravity collapse. Uplift in the wake of the seamount causes a characteristic exhumation of higher paleo-isothermal distribution in both models.